BRNO UNIVERSITY OF TECHNOLOGY

VYSOKÉ UČENÍ TECHNICKÉ V BRNĚ

CENTRAL EUROPEAN INSTITUTE OF TECHNOLOGY BUT

STŘEDOEVROPSKÝ TECHNOLOGICKÝ INSTITUT VUT

DEVELOPMENT OF A NOVEL TERAHERTZ MAGNETIC RESONANCE SPECTROMETER FOR SPIN DYNAMICS INVESTIGATIONS

VÝVOJ NOVÉHO SPEKTROMETRU MAGNETICKÉ REZONANCE V TERAHERTZOVÉM ROZSAHU PRO VÝZKUM DYNAMIKY SPINŮ

DOCTORAL THESIS

DIZERTAČNÍ PRÁCE

AUTHOR
AUTOR PRÁCE

Ing. Antonín Sojka

SUPERVISOR
ŠKOLITEL

doc. Ing. Petr Neugebauer, Ph.D.

CO-SUPERVISOR
ŠKOLITEL SPECIALISTA

Dr. Oleksii Laguta

CO-SUPERVISOR
ŠKOLITEL SPECIALISTA

Dr. Vinicius Tadeu Santana

BRNO 2022

ABSTRACT

During the last decades, the method called High Frequency/Field Electron Paramagnetic Resonance (HF-EPR) spectroscopy experienced a boom in chemistry, biology, material science, and physics. Still, HF-EPR spectrometers operating at sub-THz frequencies are mostly custom-made with non-standard solutions. The thesis aims to develop a novel broadband EPR spectrometer capable of operating in the field and frequency domain and performing frequency domain rapid scan to study relaxation times. The spectrometer operates at high magnetic fields up to $16\,T$, broad frequency range from 90 to 1100 GHz, and temperature ranges of $4 - 400\,K$. Furthermore, The work describes the design and development of six different exchangeable sample holders with a proof-of functionality measurement and unique fast-loading flange for the sample holder. The capability of the spectrometer to perform Rapid Scan measurement is demonstrated in the measurements of the LiPc single crystal and the DPPH sample dissolved in toluene.

KEYWORDS

Electron Paramagnetic Resonance, Electron Spin Resonance, EPR, ESR, High frequencies/fields, HF-EPR, Rapid scan, EPR sample holder

ABSTRAKT

Během posledních desetiletí zaznamenala metoda nazývaná vysokofrekvenční elektronová paramagnetická rezonance (HF-EPR) rozmach v chemii, biologii, materiálových vědách a fyzice. Přesto jsou HF-EPR spektrometry pracující na frekvencích blížící se THz ve světě vzácné. Cílem této dizertační práce bylo vyvinout nový širokopásmový EPR spektrometr schopný pracovat jak v širokém magnetickém poli tak v široké frekvenční oblasti a který by byl schopen provádět rychlé skenování frekvencí pro studium relaxačních časů. Vyvinutý spektrometr pracuje při magnetických polích 0-16 T, frekvenční rozsah od 90 do 1100 GHz a teplotní rozsahy $4 - 400$ K. V práci je dále popsán návrh a vývoj šesti různých výměnných držáků vzorků s EPR měřeními, které prokázali jejich funkčnosti. Design obsahuje navíc unikátní rychloupínací přírubou pro rychlou výměnu vzorku společně s držákem vzorku. Schopnost spektrometru provádět rychlé skenování frekvence pro měření relaxačních časů je demonstrována na měření LiPc monokrystalu a vzorku DPPH rozpuštěného v toluenu.

KLÍČOVÁ SLOVA

Elektronová paramagnetická rezonance, elektronová spinová rezonance, EPR, ESR, vysoké frekvence/pole, HF-EPR, rychlé skenování, držák vzorku pro EPR

Author's Declaration

Author:	Ing. Antonín Sojka
Author's ID:	151669
Paper type:	Doctoral thesis
Academic year:	2022/23
Topic:	Development of a Novel Terahertz Magnetic Resonance Spectrometer for Spin Dynamics Investigations

I declare that I have written this paper independently, under the guidance of the advisor and using exclusively the technical references and other sources of information cited in the paper and listed in the comprehensive bibliography at the end of the paper.

As the author, I furthermore declare that, with respect to the creation of this paper, I have not infringed any copyright or violated anyone's personal and/or ownership rights. In this context, I am fully aware of the consequences of breaking Regulation § 11 of the Copyright Act No. 121/2000 Coll. of the Czech Republic, as amended, and of any breach of rights related to intellectual property or introduced within amendments to relevant Acts such as the Intellectual Property Act or the Criminal Code, Act No. 40/2009 Coll. of the Czech Republic, Section 2, Head VI, Part 4.

Brno . . . .

author's signature*

---

*The author signs only in the printed version.

ACKNOWLEDGEMENT

Contents

Introduction

Spectroscopy is one of the keystones in our understanding of nature and the development of new technologies. Generally, spectroscopic methods are based on the energy exchange between electromagnetic waves and a sample, where the oscillating electric field component of the wave (E_1) interacts with a studied material (see Fig. 1), as in Optical Microscopy (OM), Far-Infrared spectroscopy (FIR), X-Ray Computed Tomography (CT), or Positron Emission Tomography (PET) (see Fig.2). In the cases of Electron Paramagnetic Resonance (EPR) and Nuclear Magnetic Resonance (NMR) spectroscopies, the oscillating magnetic field component (B_1) plays a dominant role in the interaction with the samples.
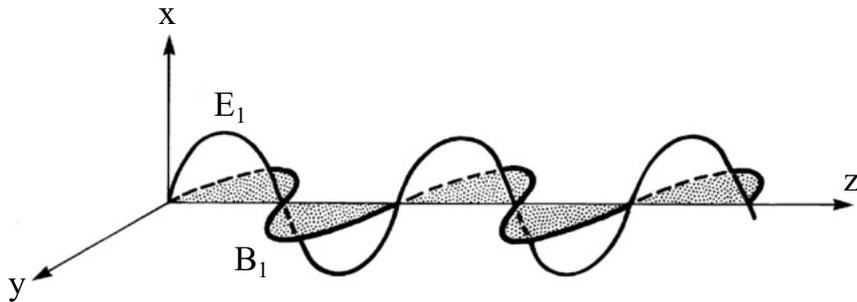
Fig. 1: Instantaneous amplitudes of electric field (E_1) and magnetic-field (B_1) components in a propagating plane-polarized and monochromatic electromagnetic beam. We note that E_1 is confined to plane xz, B_1 is confined to plane yz, with wave propagation along z. Taken from [6].

Both methods are very similar to each other. While in NMR, the electromagnetic wave interacts with nuclei, in EPR, it interacts with the spin of an electron. The techniques are based on the Zeeman effect. The effect is based the electromagnetic wave's interaction with the spin of nuclei or electrons in a magnetic field. At zero magnetic field, an isolated spin has two possible possible states of the same energy, the spin state is degenerated. When an external magnetic field is applied, the degeneracy is lifted and two energy levels can be distinguished. If the system is irradiated with an electromagnetic wave of energy (frequency) corresponding to level separation, absorption is observed. The difference in the required energy in EPR and NMR leads to a different range of frequencies that the spins need for excitation. Electron spins require three orders of magnitude higher energy to be excited than nuclei spins. The resonance condition implies that the irradiation frequency ratio to the magnetic field scales as 28 GHz/T in EPR and 42.5 MHz/T in NMR, comprising the microwave (m.w.) and radio frequency range. Thus, modern

EPR spectrometers operate in GHz and NMR spectrometers in the MHz frequency range. The requirement of higher energies led to slower development of EPR due to technical challenges, making NMR spectroscopy still more popular nowadays.
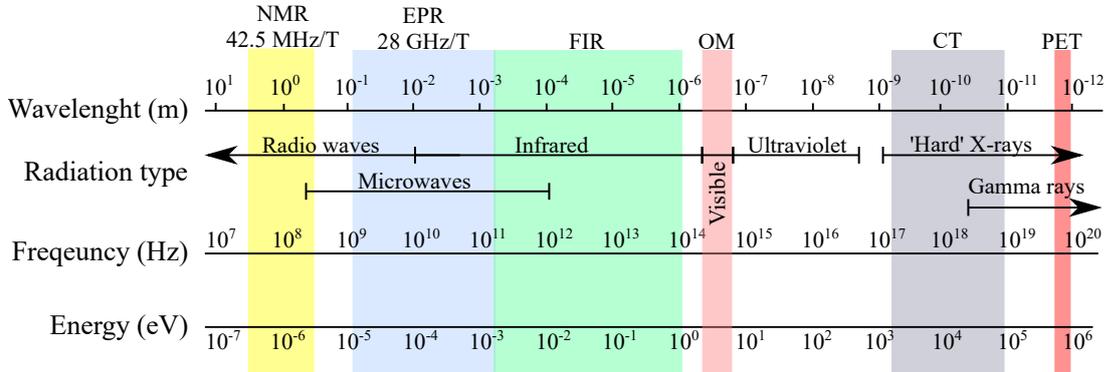
Fig. 2: Schematic image showing basic spectroscopic methods with the frequencies, wavelength and corresponding energy ranges where the methods operate.

Since its discovery in 1944 by Zavoisky [7] and parallel to the progress in the technology of m.w. propagation, m.w. sources, m.w. detectors, and superconducting magnets, EPR has been a thriving technique. Its popularity still grows as the energy range covered by this spectroscopic method moves to high frequencies and fields (HF-EPR) (above $120\dot{G}Hz$ and $4.3\,T$) [8], providing more information about the sample, higher sensitivity and resolution. Nowadays, applications of HF-EPR can be found across many scientific disciplines. For example, biologists use EPR for the calculation of distances between the atoms in proteins and molecules [6, 9, 10], chemists and physicists for determination of chemical structure and magnetic properties of molecules [11–14], and for magnetic studies of a wide range of system including monolayered materials [15, 16].

Goal of the thesis and Motivation: The interaction among spins and their environment can be described by the spin-lattice (T_1) and spin-spin (T_2) relaxation times. The access to relaxation times is crucial for the understanding and development of spin polarization agents in dynamic nuclear polarization (DNP) techniques [17, 18], and single-molecule magnets (SMMs) or single-ions magnets (SIMs) based quantum bits [19–23]. In this regard, EPR has access to relaxation times. Usually, such a task can be accomplished by pulsed EPR spectroscopy. In this method, the sample is irradiated by a series of pulses that flip the magnetization. The relaxation of the magnetization to its origin occurs in a specific time scale that is detected according to a given sequence of pulses. However, pulsed EPR resolution depends on the power of m.w. source (1 kW and more), which is at high frequencies hard and

expensive to accomplish. Moreover, HF-Pulsed-EPR has additional disadvantages imposed by the limited sample space due to the use of cavities (at 263 GHz samples are placed into a capillary with only 30 µm diameter), narrow operating band (only few GHz), and dead time which complicates measuring relaxation times bellow 50 ns [24]. These limitations can be overcome by a method called Rapid Scan EPR (RS-EPR) spectroscopy. In RS-EPR, the frequency or field is swept fast through the resonance. Suppose the sweep is comparable or faster than the relaxation time of the studied system. In that case, one can obtain an oscillatory signal called "wiggles" in the EPR spectrum, which contains information about T_2 relaxation time. The frequency-domain rapid scan measurements are more complicated to accomplish as they require a fast sweeping frequency source. Therefore, most of the published results employ field domain rapid scan [25, 26], which is easier to realize by adding sweeping coils around the sample. However, the measured band is narrow (hundreds of mT). Moreover, the data acquisition in RS is extremely fast, ms or faster, which gives the possibility to study fast processes, and additionally, RS can gain sensitivity of spectrometer under certain conditions [27]. Nevertheless, the advantages of frequency-domain rapid scan are significant, and as the progress in technologies bring more power, broader range, and more stable m.w. sources, a wider range of opportunities will be available for applying this method. In 2018, Oleksii Laguta with Petr Neugebauer showed the advantages of broad frequency rapid scan [28]; no dead time, access to ns relaxation times, and possibility to acquire T_2 relaxation time at any frequency within the range of the spectrometer. They also pointed out the problems of a rapid scan, standing wave, and significant background, which can bury the RS signal. These problems are reduced with the spectrometer developed and described in this thesis.

The main goal of this Ph.D. thesis was to design, build, and troubleshoot a novel resonance-free high-frequency/high-field EPR spectrometer that is able to operate at the same time in a frequency and field domain, and advance the frequency-domain rapid scan technique at high frequencies. Specifically, by performing frequency rapid scans on radicals dissolved in liquid that will impact on the future of Dynamic Nuclear Polarization (DNP) applications [29]. The successful study of such radicals in high magnetic fields is a necessary step in understanding and optimizing the nuclear polarization efficiency and developing spin polarization agents. The importance of DNP in Nuclear Magnetic Resonance (NMR) lies in a significant enhancement, up to several orders of magnitude, of NMR signals [17, 30–32].

Layout of the thesis: The spectrometer built during this doctoral work was inspired on a well-established operating spectrometer at the University of Stuttgart [33]; by combining the newest available commercial technology with home-made

coupling mechanisms and sample holders, our spectrometer intends to expand the possibilities of regular EPR spectrometer. The proposed spectrometer operates at frequencies from 90 GHz up to 1.1 THz, magnetic field up to 16 T and temperature range of the sample between 2-400 K (see Fig. 3B). Since our spectrometer was developed and built from scratch (see Fig. 3A), including the mechanical parts, a big part of this thesis is focused on the development of HF-EPR and also troubleshooting.
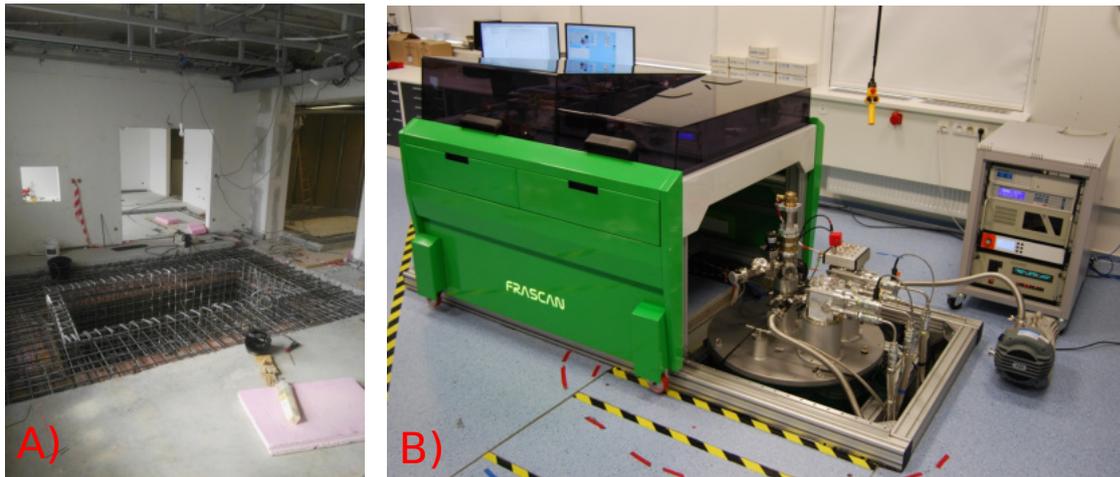
Fig. 3: A) The view of the lab in 2018 (start of my Ph.D. study). B) The HF-EPR built during my Ph.D (2022).

The thesis is split into two main parts: theoretical introduction, chapter 1 to 3, and practical part, chapter 4 to 6. The first chapter of the thesis describes the history and current state-of-the-art of EPR. At the end of the chapter is a small note about NMR development in Brno. The first half of chapter two introduces basic EPR theory and why can be benefical to do EPR in the high field. The second half of the chapter describes the spin relaxation theory, pulsed EPR, and Rapid Scan. Then, chapter 3 describes the concept of HF-EPR with a m.w. transmission system.

Chapter 4 starts with the description of the developed HF-EPR spectrometer. The reader can find the information about the main part of spectrometer: multi-use magnet frame design with airlock solution, EPR table, and EPR probe, with closer description of Quasi Optical (QO) solution, automatized coupling of m.w. between the probe and EPR table, and ultra-high vacuum (UHV) case for transporting air-sensitive samples to our superconducting magnet via an airlock and fast loading flange (FLF) for sample holder exchange at the end of the EPR probe. The chapter contains the analysis of the QO by Vector Network Analyzer (VNA) and TK power meter and cooling analysis of EPR Probe.

In chapter 5 is shown the design of six different sample holders. All sample holders are shown with the measurement example. The designed and troubleshot sample holders are: Simple Sample Holder (SSH) for pressed powder pellets or single crystals, Liquid Sample Holder (LSH) for samples in liquid form, Rotator Sample Holder (RSH) for oriented crystal in the magnetic field, Chip Sample Holder (CHSH) for testing devices under the m.w., Carousel Sample Holder (CSH) for quantitative EPR and reducing colling time during sample loading, Vacuum Sample Holder (VSH) for measuring air-sensitive samples. Besides, a specific scientific problem in the field of molecular magnetism and spin dynamics is part of the thesis to demonstrate the successful construction and scientific relevance of the spectrometer.

Finally, chapter 6 focuses on rapid scan measurements. The chapter starts with the determination of the actual spectrometer sensitivity and a description of rapid scan experiments. Then the rapid scan measurements of LiPC single crystal placed perpendicular to the external magnetic field B_0, of LiPC crystal at different angles to B_0, and rapid scan on DPPH dissolved in acetone are shown.

In the Appendix, the reader can find useful information about samples, drawings, function descriptions of Variable Temperature Insert (VTI), and basic information about the LabVIEW programs mentioned in this work.

1 History and current state-of-the-art

EPR spectroscopy, or Electron Spin Resonance (ESR) spectroscopy, may be regarded as an extension of the revolutionary experiment conducted by Stern and Gerlach in the 1920s [34]. In that experiment, they demonstrated that particles with a magnetic moment have discrete orientations due to an intrinsic property called spin. In 1938, Rabi described and measured magnetic properties of atoms, nuclei and molecules and performed the first NMR experiment [35][1]. In 1944, the first EPR experiment was performed by Zavoisky at Kazan University (see Fig. 1.1 A), a researcher from USSR. Zavoisky was first working on with NMR. Due to the inadequately inhomogeneous magnetic field available at that time, he did not achieve the desired and reproducible results [36]. Therefore, he dedicated his new efforts to the topic of EPR, which, unlike NMR, does not require such field homogeneity, but instead it requires a highly sensitive detection device. In 1944, he observed the EPR phenomenon in 1944 through m.w. absorption in a paramagnetic salt sample ($Mn_2Cl \cdot 4H_2O$) at $140\,MHz$ and $3\,GHz$, and a magnetic field up to 4.76 mT for the first time [7]. In 1977, his discovery of EPR phenomena was confirmed by the International EPR Society [36].

After 1946, the EPR technique spread rapidly worldwide, mainly because of the commercial availability of microwave components [6]. For some time, EPR and NMR technological progress went side-by-side. The first commercial NMR and EPR spectrometers were manufactured by company R.H. Varian, the first high-tech company in Silicon Valley. In 1952 the company produced first 30 MHz NMR spectrometer (see Fig. 1.1 B) [37] and in 1956 X-band EPR spectrometers [36] was manufactured. In the following years, the development of NMR and EPR slips into two main streams. In NMR, a resolution turned out to be crucial because because linewidth is very sharp (often less than $0.1\,Hz$, $3\,nT$). To be able to distinguish overlapping signals in the NMR spectra, the spectrometer requires a stable magnetic field and radio-frequency source in orders 10^{-8} of stability. The EPR signal lines are typically broader than 30 kHz or $10\,\mu T$ which decrease the requirements for a field homogeneity and a frequency stability to 10^{-5}.

In EPR and NMR, detection sensitivity is the key criterion for high-performance. Theoretically, an easy solution to get better sensitivity is to go higher resonance frequencies and magnetic fields[2]. At this point, the major difference in development progress between EPR and NMR appears. NMR spectrometers were limited by the quality and availability of superconducting magnets, unlike EPR spectrome-

---

[1]For this experiment, Rabi was awarded the Nobel Prize in 1941.

[2]The effect of g-strain and line broadening, which get worst for most samples in high fields, is not assumed.

7
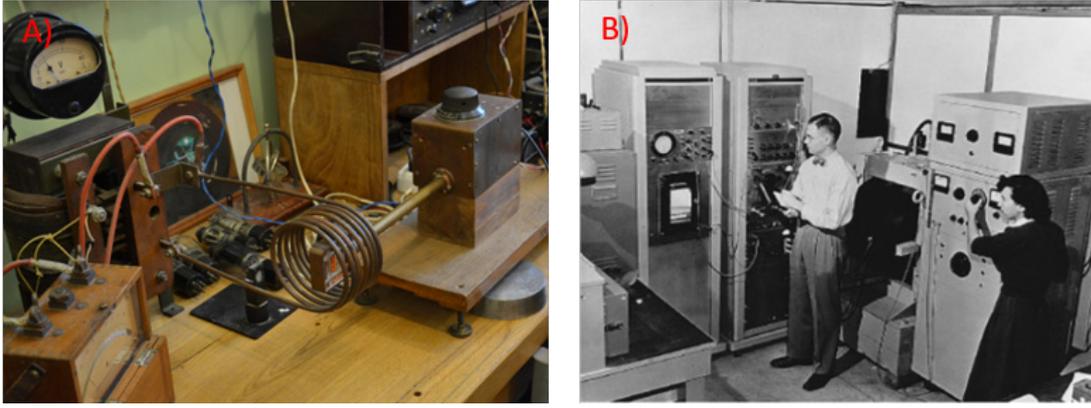
Fig. 1.1: A) First EPR Spectrometer costructed by Zavoisky. Taken from B) First commercieal 30 MHz NMR spectrometer made by R.H. Varian in 1952. Taken from [38].

ters which were mainly limited by stable and powerful high-frequency sources. The problem of the development of EPR was visible on the market of available spectrometers. Varian Associates introduced 35-GHz EPR in 1956. It took more than 30 years until 1996 when "first" high field (HF) commercial 94 GHz EPR spectrometer (E680) was introduced by Bruker Biospin[3]. The benefits of HF-EPR, such as higher sensitivity, access to zero-field splitting, better resolution, attract scientists and engineers to start working on HF-EPR. The first concept of Continuous-Wave (CW) EPR operating at 140 GHz (4.5 T) and 5 T was introduced in 1971 by Lebedev at the Institute of Chemical Physics in Moscow and Physical-Technical Institute in Donetsk [8]. After eight years, in 1978, they developed the first 140 GHz (7 T) EPR spectrometer. The spectrometer has an absolute sensitivity of 4×10^8 spins/mT at 1 Hz bandwidth. This sensitivity was about three orders of magnitude higher than *"mass-produced"* X-band EPR at that time. Lebedev group demonstrated advantages of high-field/frequency EPR on a series of experiments [39, 40], for example, a complete separation between lines of two different radicals in liquid dioxane (similar to Fig. 2.4) [41]. After introducing Fourier Transform (FT) NMR by Ernst and Anderson in 1966 [42, 43], the development of the NMR spectrometers was shifted from CW-mode to pulse mode, which is dominant nowadays [44, 45]. The pulsed NMR techniques open the door to sophisticated experiments like spin-spin distances and relaxation time measurements. Bruker Physics produced the first commercial pulse NMR in 1969. The first pulsed X-band EPR spectrometer was manufactured by Bruker Biospin in 1987 [46], and the first pulsed HF-EPR operating at 95 GHz performed successful measurements in 1989 [47]. The large time delay between both

---

[3]In this work, HF-EPR are spectrometers operating at frequencies above 90 GHz.

spectrometers is due to a missing components for fast data acquisition. The reason is that EPR relaxation times are in the microsecond range, but nuclear spin relaxations at the millisecond range, which is related to much broader EPR spectra. In 1989 CW-EPR system working between 160 and 525 GHz and magnetic fields of up to 20 T was introduced at the Grenoble High-Magnetic-Field Laboratory [48]. To operate in such a broad frequency range, they use a very stable optically pumped far-infrared laser as the source. The same process was used to build a pulsed HF-EPR spectrometer operating at 600 GHz in 1995, Grenoble (France) [49]. At high m.w. frequencies, new problems start to be present. The m.w.'s transfer from the source to the detector was suffered by high dumping from standard waveguides. Therefore, so-called Quasi-optics (QO) were employed. The QO solutions were firstly reported in EPR by the group of Freed in 1988, and their form is used up to nowadays in modern home-built, and commercial spectrometers [50]. The list of home-build HF-EPR spectrometers increased drastically from that time [51]; thus, EPR became a useful complementary method to study samples' physical, chemical, and biological properties. In the new millennium, pulse EPR spectrometer was experiencing big in development. Many techniques in pulse EPR was invented, and scientist started to combine EPR and NMR in Dynamic Nuclear Polarisation, where HF-EPR spectrometers are used to polarize nuclei via electronic cross-relaxation [52, 53].

Most of the cw-EPR spectrometers mentioned in the paragraph above were working in the magnetic domain, a sample is irradiated by m.w of fixed frequency and the magnetic field is swept through resonance. The reason is simple, the sources that would operate at broad frequency range simultaneously with small variations of power and phase noise are expensive and very rare on the market. The advantages of such systems are undeniable. For example, studying a sample such as single molecule magnets (SMMs) with multiple frequencies helps significantly to later measurement processing and determination of sample parameters. To calculate system parameters as zero field splitting more than one measurement is needed to observer EPR signal peaks dependency. With multi-frequency EPR, field dependent and field-independent phenomena can be easily distinguished. Nowadays, EPR spectrometers can be easily found operating even at high frequencies up to THz frequencies [54]. One of the first who employed field and frequency sweep simultaneously, record of EPR map, was Petr Neugebauer in Stuttgart [33]. The system operates between 90 - 750 GHz and 0-16 T. Although, the EPR map suffers from standing waves induced in the system and non-linear power distribution of the EPR source. One of the solutions to this problem is to implement Martin-Puplett interferometry [55] to change total path length distance and adjust m.w. phase.

One branch of EPR spectroscopy is closely connected to this work, the Rapid scan EPR method. A method that can improve the signal to noise ratio and significantly

9

decrease the acquisition time and, more importantly, get access to relaxation time, T_2. The rapid scan is here from the beginning of the development of NMR in 1948, where the *"wiggles"* were observed in situations in which the passage time of the magnetic field through resonance is shorter than T_1 and T_2 [56–58] (see Fig. 1.2). Dadok was the first person who implemented rapid scan in NMR [59]. In the following year, it was proven that rapid scan NMR could achieve roughly 35 % smaller signal intensity than pulse Fourier Transform (FT) NMR [60]. Therefore, in 1970 rapid scan NMR was overshadowed by FT-NMR due to the wide range of pulse sequences that became available [60]. The first rapid scan of EPR was done in 1955 by the group of Portis [61]. Since the method is based on how fast a spectrometer can sweep through a spectrum, the method evolved step-by-step with technology. Nowadays, most of the rapid scan measurements are realized in the field domain by irradiating samples with a constant m.w. and sweeping fast through resonance with a modulation coil.
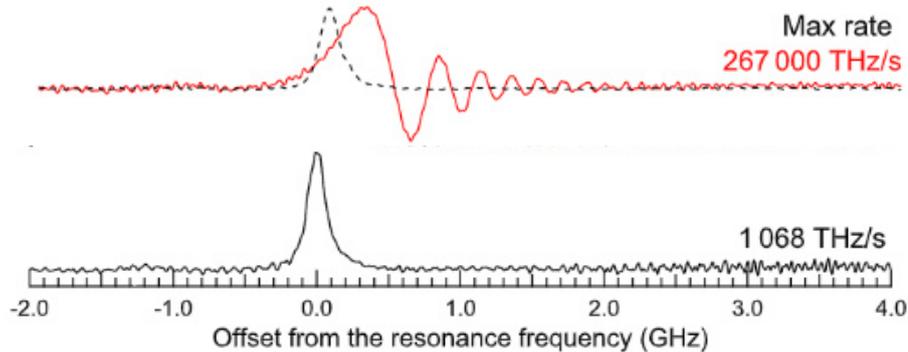
Fig. 1.2: Rapid scan spectra of the LiPc sample recorded at the fixed field of 8 T, temperature of 13 K and modulation frequencies 20 kHz and 5 MHz, and constant modulation amplitude of 8.5 GHz. In the first spectra, black, the sweep rate is not fast enough, and only absorption signal without "wiggles" is measured. Traces are labeled by the maximum sweep rate achieved at the center of sweep. Dashed curves are the deconvoluted spectra. Taken and adjusted from [28].

The field domain rapid scan uses only one frequency compared to the frequency domain. Therefore, the spectrometer can significantly increase sensitivity by employing a resonator with a well-optimized transmission system. Moreover, field domain EPR is much cheaper compared to the frequency domain. Mainly Eatons are responsible for the big progress in this field [26, 55, 62–65]. Their works and collaboration with the company Bruker resulted in 2019 into the first commercially available rapid scan X band spectrometer [66]. The negative side of field domain rapid scan is the restriction to one band, relatively slow sweep of the magnetic coil,

and the rapid field change by the varying current in the modulation coil induces significant heat and vibrations without clever design. Therefore such systems are space-demanding. On the other hand, the frequency domain EPR can be generally used over a wide range of frequencies with one spectrometer. Furthermore, there is no restriction about the sweep range as they can easily measure nanosecond relaxation times, which is not possible with fast field sweeps. Therefore, we can expect rapid scan relaxation studies on the broad signals as SMM or SIM in the near future. On the other hand, the power distribution[4] and standing wave introduced into the system are the biggest problems of this method [28]. To sum the current state of of EPR spectroscopy is difficult as EPR spectroscopy is still evolving. Thanks to the new generation of sources and detectors coming up in this decade, the golden era of EPR spectroscopy is yet to come. But the reader has to remember the words about EPR development, "*Eaton Rules*" from *Biller* and *McPeak* [67]:

- Be aware of advances in other technologies—you never know when someone else has already solved a problem that has you stumped.
- Never assume the EPR experiment is bound to only one size/shape or implementation.
- Experiments which are "impossible" today can be possible tomorrow.

History of NMR in Brno

Here, I would like to write a few lines about the NMR production history in my University town Brno. In the 1950s, only two companies in the whole world were manufacturing NMR spectrometers, Varian (in the USA) and Jeol (in Japan). At that time Czechoslovakia was satellite state of the Soviet Union. A closed market and isolation made the development of NMR, where "know-how" is needed, complicated. Even so, the company Tesla Brno, under the supervision of Josef Dadok, was able to produce over 500 NMR spectrometers.

In 1965, TESLA Brno presented the first of their NMR spectrometer, TESLA BS477 (see Fig.1.3), to the world. The spectrometer operated at a frequency 60MHz. The spectrometer was successful on the international scene, and many experts from the world came to visit TESLA Brno to see the production. However, the lack and price of complex electric units slowed down the production and further development. Therefore in 1989, the NMR spectrometer production had been stopped.

To remind the TESLA Brno development team's achievements and honor the leader of this team Josef Dadok, the new J. Dadok National NMR Centre is named after him.

---

[4]The distribution of m.w. source output power over its frequency range.

Fig. 1.3: Picture of TESLA BS477. Taken from [68].

2 Theory of EPR

This chapter contains a brief review of the properties of an electron and how atoms, molecules, or more complex systems are eligible to be studied by EPR. The chapter also introduces the basic principles of EPR, including relaxation studies and why high magnetic fields and frequencies are important in EPR. The content of this chapter was taken mainly from [6, 51, 69, 70].

2.1 Electron has magnetic moments

The electron, an elementary particle with charge e and mass m_e can be found in every atom or molecule around us. It has magnetic moments that can be described by classical or quantum theories. According to the classical electromagnetic theory, the magnetic moment μ has a particle with mass (m) and an electrical charge (q):

$$\mu = \frac{q}{2m}\sigma, \tag{2.1}$$

where σ, *angular momentum*, is a mechanical quantity linked to movement of the point mass. This description is applicable to any elementary particles. For the electron:

$$\mu_l = \frac{-e}{2m_e}\sigma_l. \tag{2.2}$$

μ_l and σ_l are called orbital angular momentum, and the orbital magnetic moment of the electron. In the quantum mechanical description, variables μ_l and σ_l are quantities, and can take only certain values. Therefore, $\sigma_l(\sigma_{l,x}, \sigma_{l,y}, \sigma_{l,z})$ can only take discrete values of the form:

$$\sigma_l^2 = l(l+1)\hbar^2, \tag{2.3}$$

where l is orbital number and $\hbar$ is reduced Plank constant equal to $h/2\pi$. If the orbital number l is fixed, the components of σ_l can take only values of the form:

$$\sigma_{l,i} = m_l\hbar, \quad \text{for} \quad i\text{=}x,y,z. \tag{2.4}$$

The angular momentum σ_l is linked to the electronic motion. Additionally to that, we can introduce the electron spin angular momentum σ_S, which has similar relation to equations 2.3 and 2.4:

$$\sigma_S^2 = s(s+1)\hbar^2 \quad \sigma_{s,i} = m_s\hbar, \tag{2.5}$$

where s is an intrinsic characteristic of the electron known as spin with value $S = 1/2$. Therefore, m_s can take only values $\pm 1/2$ and we can introduce spin magnetic

momentum μ_s which corresponds to the *spin angular momentum* σ_S, Bohr magneton in the specific case of one electron:

$$\mu_s = -g_e \frac{e}{2m_e} \sigma_s, \tag{2.6}$$

where g is g-factor, one of a fingerprints of each atom, molecule or structure. For free (unbound) electron is $g = g_e = 2.00231930436146(56)$ [71]. An unpaired electron responds not only to a applied magnetic field B_0 during the EPR measurements, but also to any local magnetic fields of atoms or molecules. Thus the $g \neq g_e$, but is equal to value, which characterizes the study system. Then, the electron's total magnetic moment is:

$$\mu = -\left(\frac{e}{2m_e}\right)(\sigma_l + g_e\sigma_s). \tag{2.7}$$

In a close look, any sample or molecule contains great numbers of electrons, where each electron has a magnetic moment. However, the restriction imposed on the electrons makes the sum of magnetic moments often null.

2.1.1 Paramagnetism

Paramagnetic materials or compounds, a large group of samples that EPR studies, are characterized by one or more unpaired electrons, which depends on the number of electrons in each orbitals. An atomic orbital is space where electron are located and its identified by a triplet number (n, l, m_l) (see Table 2.1):

Tab. 2.1: Quantum numbers determining shape of the orbital.

number	Values	Meaning
n	1,2,3...	distance from nuclei
l	0,1,2,...,(n-1)	orbital momentum (size)
m_l	$0, \pm 1, ..., \pm l$	orbital momentum (z - component)

The number $l = 0, 1, 2, 3$ corresponds to *s,p,d,f*-type of orbital. The visualization of the orbitals is shown in [72]. The electrons start filling the lowest possible state first according to Pauli's exclusion principle, which requires that each orbital harbors maximally two electrons, one with spin $m_S = -1/2$ and one with spin $m_S = +1/2$. All orbitals characterized by the same number of n are located in one shell. The number of the electrons in this shell equal n^2. Each shell comprises subshells of $(2l+1)$ orbitals by a given electron pair (n,l). When the subshell is full, all possible values of m_l are used, their sum is null, and the atom or molecule does not have the magnetic moment. Generally, an atom has a magnetic moment when one of its

Tab. 2.2: Atoms with an incomplete subshell. Taken from [70].

1s	H
2s	Li
2p	B, C, N, O, F
3s	Na
3p	Al, Si, P, S, Cl
4s	K
3d	Sc, Ti, V, Cr*[1], Mn, Fe, Co, Ni, Cu*
4d	Y, Zr, Nb*, Mo, Tc, Ru*, Rh*, Ag*
4f	Ce*, Pr*, Nd*, Pm, Sm, Eu, Gd*, Tb*, Dy, Ho, Er, Tm, Lu*
5d	La*,Hf, Ta, W, Re, Os, Ir, Pt*, Au*
5f	Th, Pa, U, Np, Pu, Am, Cm, Bk, Cf, Es, Fm, Md, No, Lr

subshells, typically the highest energy subshell, is incomplete (the table 2.2 shows atoms with an incomplete subshell).

In EPR, the signal originates from atoms with incomplete subshells. However, an incomplete subshell is insufficient condition for an atom to be paramagnetic and thus have an EPR signal. Numerous atoms shown in table 2.2 are not paramagnetic [70]. Moreover, we generally measure in EPR elements organized in molecules and crystal lattices, where valence electrons create chemical bound in molecular orbitals. Each orbital can accept up to two electrons with spin $+1/2$ and $-1/2$. If the molecule has an even number of electrons, the sum of spin magnetic moments is null, and molecules are non-paramagnetic. However, there are three exceptions [6, 51, 69, 70]:

1. Molecules with even numbers of electrons, that have two unpaired electrons in their ground state, molecules with B_2, O_2, biradicals groups and molecules composed of two coupled entities, each with one unpaired electron.
2. When the number of the electrons in the molecule equals to an odd number. These systems are known as free radicals, and typically they include OH*, CN*, NO* NO_2* groups.
3. Paramagnetic centers in solid form (conduction electrons in metals, ionised impurities in semi-conductors, organic molecular conductors, and a wide variety of point defects).

---

[1]Superscript * marks the atomic subshells with not "regularly" electron filling.

2.2 Basic principles of EPR

The basic principle of EPR is based on the Zeeman effect (Fig. 2.1), where the oscillating component, B_1, of an electromagnetic wave at frequency f interacts with the magnetic moment of an unpaired electron spin, $S = 1/2$, in the presence of an applied external magnetic field B_0. The resonance condition for $S = 1/2$ is then as follows:

$$\Delta E = E_u - E_l = hf = g\mu_B B_{res}, \tag{2.8}$$

where E_u and E_l are the energies of the two possible m_s states of spin $S = 1/2$, B_{res} is the resonance field.
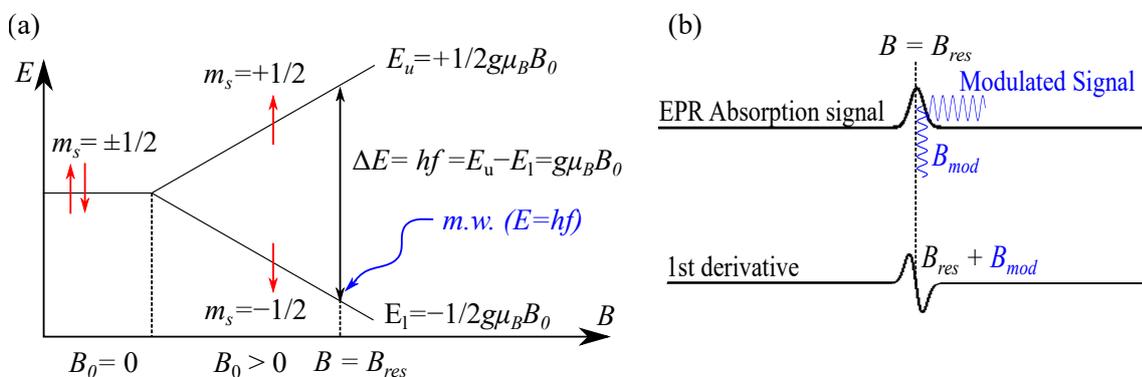
Fig. 2.1: Example of the interaction between a hydrogen atom with spin $1/2$ and the external magnetic field. If the amplitude of external magnetic field B equals to zero, there will be no energy difference between the spin state $m_s = +1/2$ and $m_s = -1/2$. However, if the external magnetic field has a non-zero value, the separation between the energy states occurs. By applying an external electromagnetic wave with energy equal to the separation of the energy states, the spin can be excited to the higher state.

The resonance condition implies that irradiation frequency scales by $28\,\mathrm{GHz/T}$, m.w. range. An absorption EPR signal is observed when the resonance condition is fulfilled, *e.g.* when the electromagnetic wave's energy hf matches the energy levels' separation ΔE (see Fig 2.1). In order to further improve EPR signal-to-noise ratio (SNR), a small modulating field, B_{mod}, oscillating at few kHz, is applied, leading to the actual measurement of the derivative of an absorption spectra (Fig. 2.1, right) [73]. In the case of a system with more than one unpaired electron, $S > 1/2$, the spin-spin and spin-orbit couplings may lift the degeneracy of spin states even at zero-field, the so-called zero-field splitting (ZFS).

Nevertheless, other physical phenomena play a role in spin systems. For many relevant applications, those phenomena lies in the range of higher energies and require higher magnetic fields and frequencies to be adequately detected and described. Therefore, Hamiltonian contains these terms:

$$H = H_{Zeeman} + H_N + H_{HFS} + H_{LS} + H_{elect} + H_{ef} + H_{SS} + H_Q, \qquad (2.9)$$

where new components represent the following interactions:

H_{Zeeman}	Electron Zeeman energy
H_N	Nuclear Zeeman energy
H_{HFS}	Hyperfine structure
H_{LS}	Spin - orbit interaction
H_{elect}	Electron repulsion energy
H_{ef}	Crystal (ligand) field energy
H_{SS}	Spin-spin interaction
H_Q	Nuclear Quadrupole energy

A detailed description of the components of the Hamiltonian components can be found in [6]. The magnitude of these different contributions to the Hamiltonian is shown in Fig.2.2.
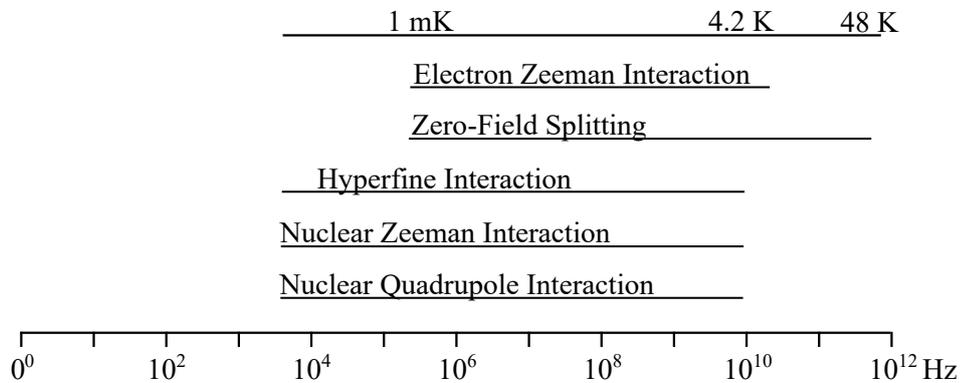
Fig. 2.2: Table with the order of magnitude of different phenomena related to EPR given in units of frequency and temperature. Adapted from [74].

2.2.1 Frequency domain vs Field Domain EPR

There are two ways to meet the resonance conditions in an EPR experiment. The sample can be either irradiated by a m.w. beam with constant frequency during sweeping of the magnetic field (Magnetic Domain Magnetic Resonance (MDMR))

or to maintain a static magnetic field and sweep the frequency of the m.w. radiation (Frequency Domain Magnetic Resonance (FDMR)). Irradiating the sample at the constant frequency during the experiment is called continuous wave- EPR (cw-EPR).

In many samples, the study energy splittings are caused by field independent interactions, such as zero-field splitting (ZFS) or crystal-field splitting. An FDMR measurement has a significant advantage over the MDMR in that the EPR spectrum is recorded even at zero fields (see Fig. 2.3 b) [75]. Therefore, the energy spectrum of the study system is recorded directly, while in MDMR, those properties have to be extrapolated. Moreover, to determine magnetic parameters by EPR precisely very often are required a multifrequency study [33]. Typically, these studies are presented as frequency filed plots [76]. In MDMR, the HFEPR spectrum is often recorded as a series of different frequencies, which is extremely time-consuming because the ramp speed of the superconducting magnet is defined by the capacity of the cryogenic system [77]. Therefore, it is beneficial to record FDMR spectra together with continuous ramping of the magnetic field. The result, *EPR map*, is a two-dimensional frequency-field map presented in Fig. 2.3. Moreover, FDMR achieves a much faster sweeping time that could be hungered of GHz in milliseconds or even faster in the so-called rapid scan regime (discussed in section 2.4.). In comparison sweep rate of MDMR, limited by the cooling power of its cryogenic system, results in T per minute with superconducting magnets [78]. Additionally, the FDMR spectrum can be recorded even while the magnet is in persistent mode to save the valuable resource of liquid helium. Lastly, some of the samples have an energy spectrum that spans over a broad energy range up to several THz [79]. In such cases, magnetic fields required to measure MDMR are impossible to achieve.

Nevertheless, most of the EPR spectrometers in the world perform experiments in the magnetic domain. The main reason is the technological challenge and implementation of a wide frequency sweep compared to the wide magnetic field ramp. Changing the current in a conductor is easier than sweeping the frequency in wide, up to hundreds of GHz, range [80, 81]. Moreover, the MDMR can employ a resonator, which can significantly improve sensitivity [51]. Nowadays, more and more scientific groups have started using the FDMR setup in combination with MDMR setup.

2.2.2 Advantages of EPR in High Fields/Frequencies

Increasing sensitivity: Another advantage of using high frequencies is the increase in detection sensitivity. The ratio between the Boltzmann distribution of the population of the spin states in a two-level system in equilibrium by applying a magnetic field, as it is the case for a $S = 1/2$ system is given by
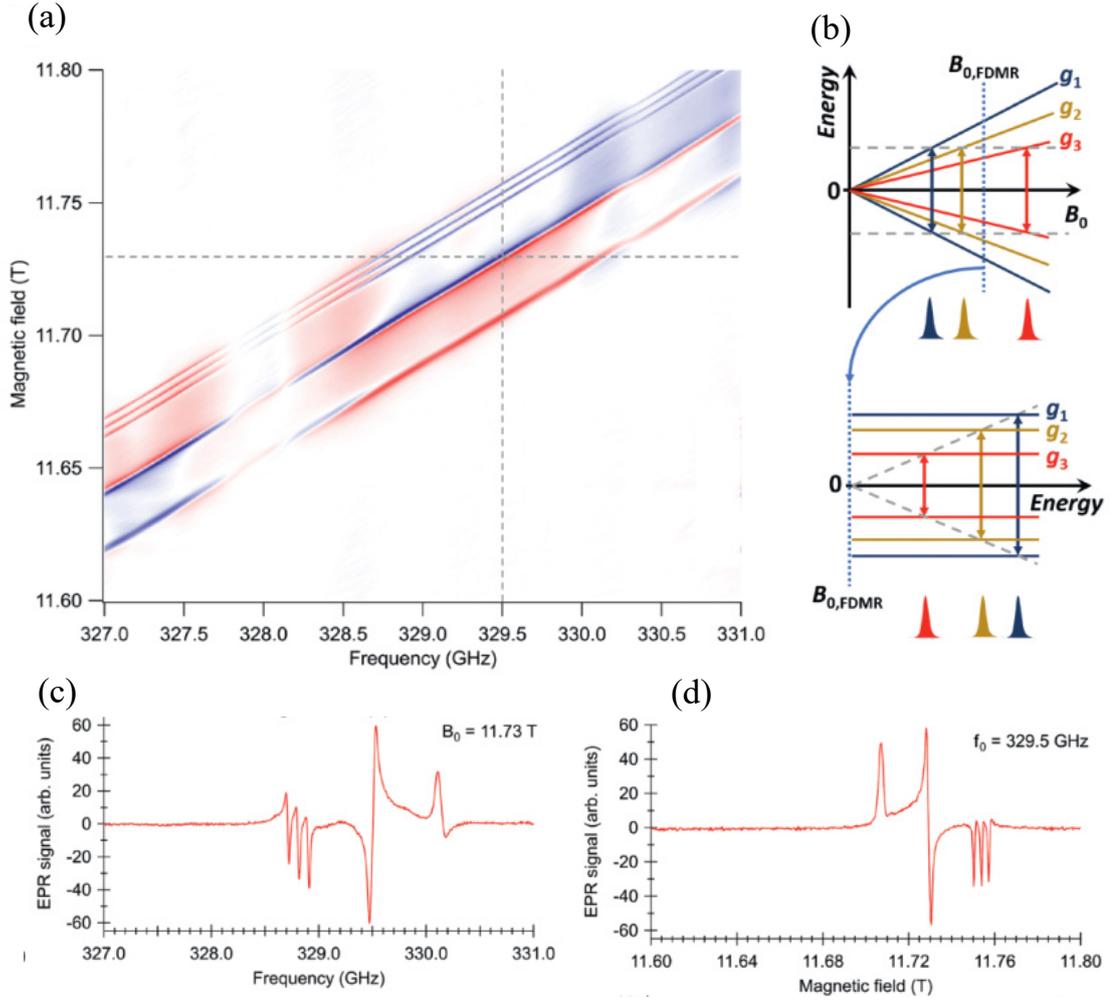
Fig. 2.3: (a) A two-dimensional frequency-field EPR map of TEMPOL dissolved in polystyrene, resulting in a 2.5 mg film with 10^{16} spins. The map with a resolution of 10000x1000 points in frequency and field axis, respectively, was acquired by the collection of single frequency scans while sweeping the magnetic field. (b) The extracted field and frequency domain spectra from the map in (a). (c) and (d) Illustration of EPR and FDMR experiments at EPR fixed frequency (energy) and FDMR fixed magnetic field (B_0,FDMR), respectively. Taken from [77].

$$\frac{N_u}{N_l} = \exp\left(-\frac{E_u - E_l}{kT}\right) = \exp\left(-\frac{hf}{kT}\right), \tag{2.10}$$

where E_u and E_l are the energy corresponding to the $m_s = 1/2$ and $m_s = -1/2$, N_u is the number of spins occupying the higher energy level, and N_l is the number of spins occupying the lower energy level, k is the Boltzmann's constant, and T is thermodynamic temperature. The net absorption of radio-frequencies by the sample

corresponds to the EPR intensity and it depends on the difference in occupancy between the number of spins in the lower and upper states.

Equation 2.10 states that at the low temperature, the number of spins able to be excited increases and consequently, the EPR signal increases since it is proportional to the population difference $\Delta n = n_{lower} - n_{upper}$. For example, at the temperature of 300 K and frequency of 10 GHz, N_u/N_l is equal to 0.998, but at temperature 2K and the same frequency, this ratio equals 0.787. Hypothetically, that means that on average 213 electrons from 1000 spins in the system are involved in absorption compared to 2 spins involved at room temperature. This scheme and interpretation can be extended to an N-level system by writing the corresponding Boltzmann distribution for each level according to its energy.

Higher spectral resolution: A variety of the sample [6]: molecules with g-anisotropy (molecule orbital orientation to the magnetic field is represented as g_x, g_y, g_z), samples containing two systems with slightly different g-factor, or systems containing hyperfine splitting are studied in high magnetic fields and frequencies, where those species are well separated (see Fig. 2.4).

Using the resonance condition in Eq. 2.11, we can determine the separation between the resonance position for two different free radicals with two different g parameters. If both radicals have an isotropic g-value g_1 and g_2 ($g = (g_x + g_y + g_z)/3$) then the resonance separation will be:

$$\Delta B = \frac{hf}{\mu_0} \left(\frac{1}{g_1} - \frac{1}{g_2} \right). \tag{2.11}$$

Comparing a W-band spectrometer (360 GHz, 3.6 T) with an X-band spectrometer (9.5 GHz and 330 mT), the separation will be resolved by more than 40 times. Such an increase in resolution is valuable in organic radicals measurements. In such cases, the isotropic g-value is very close to the free-electron g-value, and the difference between them is in the order of 10^{-4}. By measuring such a sample with an X-band spectrometer, the difference between those resonances will be equal to 0.03 mT, which is not easy to distinguish due to the finite linewidth of absorption lines.

In the next step, the Hamiltonian (equation 2.9) will be simplified to the interaction of an unpaired electron with nuclei in a typical paramagnetic radical (see equation 2.12). The first component, H_{Zeeman}, is the Zeeman Energy and it was mentioned in equation 2.8, and the second component H_N, Zeeman Nuclear spin energy, has a similar interpretation as a Zeeman energy but for nuclear spins. The last relevant component, H_{HFS} or Hyperfine structure, refers to small shifts and splitting of the energy levels of atoms, molecules, or ions due to the interaction among electrons and I nuclear spins:

$$H = H_{Zeeman} + H_N + H_{HFS} = hg_e\mu_B B_{ext}S - \sum_i g_{Ni}\mu_N B_{ext}I_i + \sum_i SA_iI_i, \quad (2.12)$$

where μ_N is the nuclear magneton, g_{Ni} the nuclear g–values, I_i is the nuclear spin operator, and A_i describes the magnitude of the interaction between the electron and nuclear spins, the hyperfine coupling tensor. Equation 2.12 shows that the electron Zeeman's effect and the Nuclear Zeeman's effect are field-dependent. In contrast, the hyperfine structure is field-independent. Thus, the interaction of the electron with the nucleus to a first approximation is independent of the applied magnetic field. For example, the EPR spectra with g-anisotropy of a TEMPOL radical becomes resolved only at W-band frequency, allowing both to distinguish between the g anisotropy ($g_{xx} > g_{yy} > g_{zz}$) and the anisotropy in the hyperfine interaction ($A_{xx}, A_{yy} << A_{zz}$), which is dominant in the z-direction.
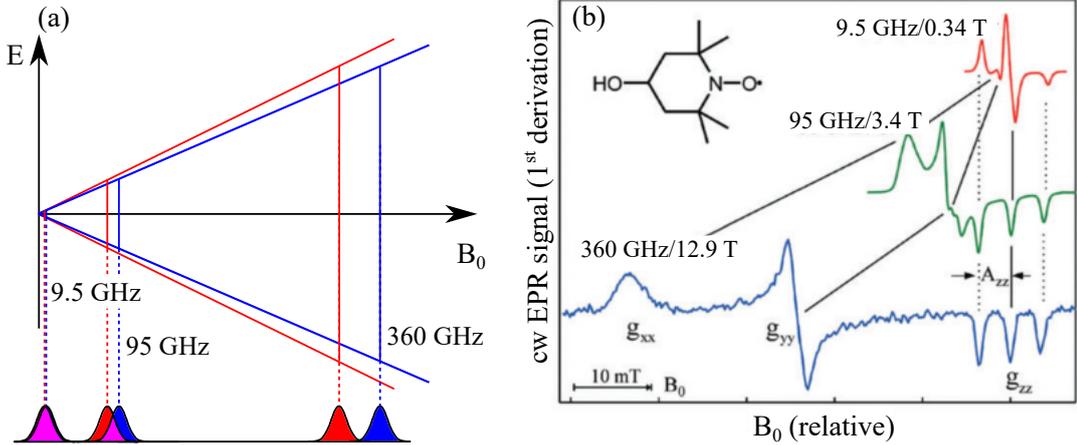
Fig. 2.4: a) Two species of different g-values are very diffcult to distinguish at the X-band (9.5 Ghz) frequency. The situation gets better for the W-band (95 Ghz) frequency where we can already see the two lines presented. However, only the lines for the high (360 Ghz) frequency are fully separated. The resolution of a W-band spectrometer can be considered as one order of magnitude higher than that of a X-band spectrometer. Taken from [82]. b) First-derivative CW-EPR spectra of a TEMPOL in frozen water solution at different microwave frequency/B_0 settings. The spectra are plotted relative to the fixed g_{zz} value. Taken from [83].

Therefore, by increasing the magnetic field, the spectrum becomes better resolved, and the hyperfine structure may become evident. The need to use high frequencies to resolve the spectrum and observe the hyperfine splitting can be expressed by the following equation:

$$\Delta B \frac{\Delta g}{g_{iso}} > \Delta B_{HFS}^{1/2}. \tag{2.13}$$

When the anisotropic Zeeman interaction exceeds the linewidth due to unresolved hyperfine interactions, going to higher frequencies and fields helps [51].

Zero-field splitting detection: For $S > 1/2$, the so-called high-spin systems, the zero-field splitting (ZFS) term H_{ZFS} in equation 2.9 plays a fundamental role [69,84]. The solution for a $S = 3/2$ system with a zero-field splitting $D = 300\,\text{GHz}$ is shown in Fig. 2.5A. To see ZFS by EPR experiment directly, it is typically necessary to use high m.w. frequencies that correspond to the separation between the energy levels [85, 86]. A good example is $Mn_{12}Ac$ with a spin $S = 10$, one of the first SSM [87, 88]. At EPR map (see Fig. 2.5 B) is visible, that with FDMR system operating at high frequencies (190 to 350 GHz in this case) it is possible to see level separation (absorption of m.w.) even at zero magnetic fields.
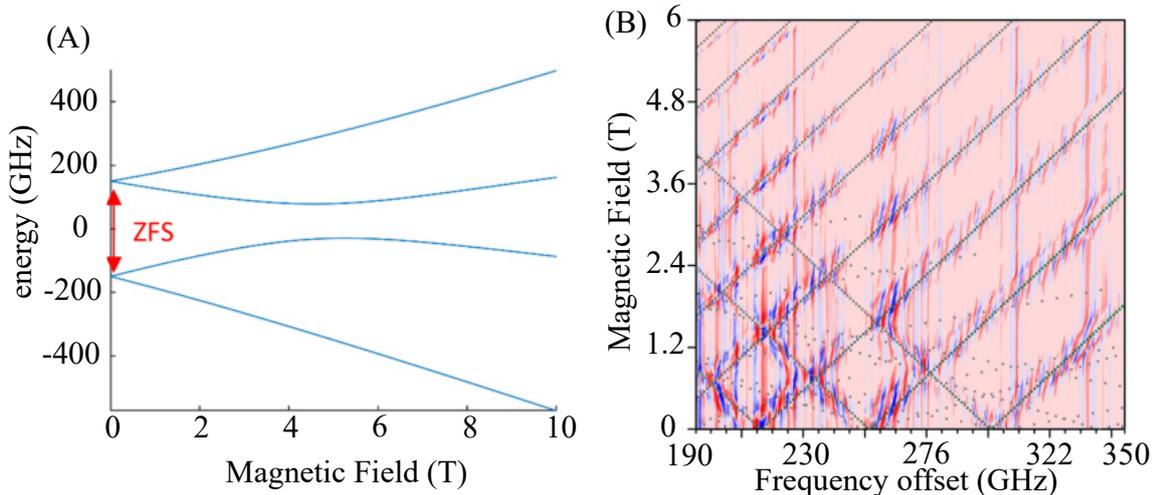
Fig. 2.5: (A)The level energy (Hamiltonian solution) of a 3/2-spin system placed into the magnet field. (B) The measurement are showing EPR map 1200x800 resolution of Mn_12Ac crystal together with simulation (dotted lines). Parameters of simulations: S = 10, g = [1.93, 1.96], D = - 13790.5 MHz, B_4^4 = 1.19917 MHz, B_0^4 = -0.659543 MHz. Taken from [77].

Spectrometers operating at lower frequencies (X-band, Q-band, W-band) are not suitable for the studies of molecules with high ZFS, which are referred in the literature as "EPR silent". The strict meaning of "silent" is therefore connected to the availability of a suitable spectrometer to probe the transitions in the studied material.

2.3 Spin Relaxation

This section will introduce the term spin relaxation and the effect of m.w. pulse on sample magnetization. Later, the section explains how the relaxation is measured by pulse and rapid scan EPR.

General aspects   For an instructive introduction of relaxation times, the properties of a two-level spin system will be presented. The problem will be depicted using the case of an ensemble of spins with $S = 1/2$. In our model, the spins are isolated, therefore the spin-spin interaction is negligible. The spin system is located inside a magnet with an uniform magnetic field B_0. Therefore, two energy levels separation is present with a difference of energy $\Delta E = E_u - E_l$ and only Zeeman spliting parameter is considered in spin Hamiltonian:

$$\frac{N_u}{N_l} = \exp\left(-\frac{\Delta E}{k_B T}\right). \tag{2.14}$$

When this system is exposed to electromagnetic radiation matching the energy difference between the levels, the ratio between the N_u and N_l is altered. Electrons that absorbed energy are considered as "*hot*" to their surroundings. Such hot spin has spin temperature T that is eventually restored to the temperature T_s of the surrounding. The process of losing the extra energy δE_0 at time $t = t_0$ is shown in Fig 2.6 and can be described with an exponential decay through the expression:

$$\delta E = \delta E_0 \exp\left(-\frac{t - t_0}{T_1}\right), \tag{2.15}$$

where T_1 is the characteristic time for energy flow from the spin system into the surrounding.

Spin dynamics   In the following text, the previous discussion about the population difference is treated more carefully. We consider

$$\Delta N = N_u - N_l, \tag{2.16}$$

as a variable $\Delta N(N, T_S)$, where N_l, and N_u are defined:

$$N_u = \frac{1}{2}(N - \Delta N) \qquad \& \qquad N_l = \frac{1}{2}(N + \Delta N), \tag{2.17}$$

where $N = N_l + N_u$ is the total population of spin system. The probability of the spin being in an upward or downward transition is Z_u and Z_l in unit time. The difference between the transition rate for the kinetic system is:

$$\frac{d\Delta N}{dt} = -2N_u Z_u + 2N_l Z_l. \tag{2.18}$$
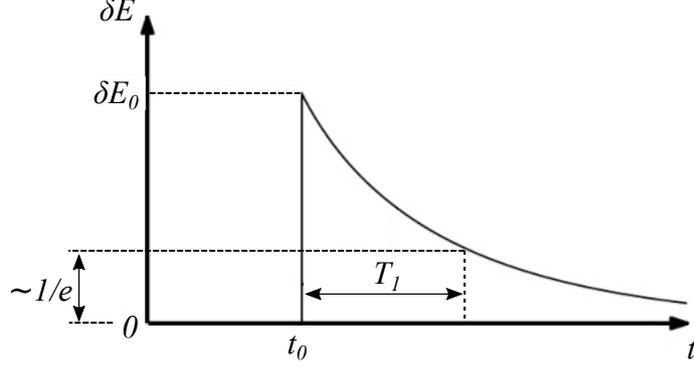
Fig. 2.6: Decay of the extra energy δE_0 in the system at the time t_0 to $1/e$ value. The relaxation time T_1 is an indirect measurement of the coupling between the spin system and its surroundings.

This equation can be rewritten as:

$$\frac{d\Delta N}{dt} = N(Z_l - Z_u) - \Delta N(Z_l + Z_u) = \left(N\frac{Z_l - Z_u}{Z_l + Z_u} - \Delta N\right)(Z_l + Z_u). \quad (2.19)$$

The system is balanced (called in a steady state) when $d\Delta N/dt = 0$. The equation 2.19 is equal:

$$\Delta N^s = N_l^s - N_u^s = N\frac{Z_l - Z_u}{Z_l + Z_u}. \quad (2.20)$$

With this solution we can rewrite equation 2.19 to:

$$\frac{d\Delta N}{dt} = (\Delta N^s - \Delta N)(Z_l + Z_u). \quad (2.21)$$

The quantity $(Z_l + Z_u)^{-1}$ is by definition relaxation time T_1:

$$\frac{d\Delta N}{dt} = \frac{\Delta N^s - \Delta N}{T_1}. \quad (2.22)$$

The equation 2.22 is a first order kinetic equation with the solution:

$$\Delta N = (\Delta N)_0 + [\Delta N^s - (\Delta N)_0]1 - \exp\left[\frac{-(t - t_0)}{T_1}\right]. \quad (2.23)$$

From this solution can be assumed several statements:
- $\Delta N(t)$ evolves exponentially to $(\Delta N)_0$ with rate constant $k_1 = T_1^{-1}$,
- T_1 represents the lifetime of a given spin-orientation state (affect linewidth broadening due to the Heisenberg uncertainty principle).

2.3.1 Mechanism of T_1

The origin of the transition Z_l and Z_u can be described as followed:

$$Z_u = B_{lu}\rho_V + W_u \qquad \& \qquad Z_l = A_{ul} + B_{ul}\rho_V + W_l, \quad (2.24)$$

where ρ_V is time-average radiation density irradiating the system, W_u and W_l are upward and downward transition probabilities for transition due to surroundings. $A_u l$ is Einstein coefficient for spontaneous photon emission and B_{ul} and B_{lu} are Einstein coefficient ($B_{lu} = B_{ul}$) for stimulated emission and absorption (magnetic dipole transitions). By submissions equation 2.24 into 2.21 and 2.22 results:

$$\Delta N^s = N\frac{A_{ul} + W_l - W_u}{A_{ul} + 2B_{ul}\rho_V + W_l + W_u},$$
(2.25)

$$T_1 = (A_{ul} + 2B_{ul}\rho_V + W_l + W_u)^{-1}.$$
(2.26)

From this equation, power saturation can be explained. If the system at resonance is exposed to the radiation density ρ_V which dominates in equation 2.25, Z_u and Z_l become equal and the population difference between the spin states will approach zero, $\Delta N \Rightarrow \Delta N^s \Rightarrow 0$, causing the EPR signal to disappear [6]. This phenomenon is called power saturation. The most important T_1 mechanisms [69,89] are the following (see Fig. 2.7):
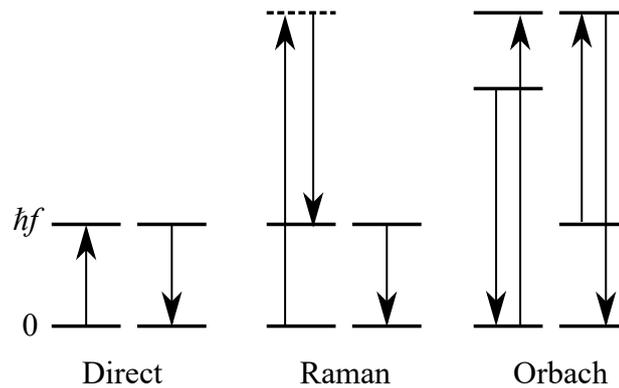
Fig. 2.7: Schematic overview over the different magnetisation relaxation (spin–lattice relaxation) processes for a (Kramers) doublet split by the Zeeman interaction. Dotted state represents virtual state. Taken and adjusted from [90].

1. *Direct processes*: The process dominates at very low temperatures on the phonon-assisted non-radiative transition between spin levels.
2. *Raman processes*: Virtual excitation and excitation to phonon states on much higher energy than the spin levels. This process has higher probability with increasing temperature, where the temperature depence of T_1 vary between T^{-5} to T^{-9}.
3. *Orbach processes*: A two-phonon process in which the energy to be transferred to the lattice is the difference between the energies absorbed and emitted for a specific low-lying excited state.

2.3.2 Bloch Model

Magnetization: The magnetization M can be expressed as:

$$M = \frac{1}{V} \sum_{i=1}^{M} \mu_i. \tag{2.27}$$

The magnetization is the sum of the net magnetic moments per unit volume (see Fig. 2.8) [91]. Bloch equations describe the time dependence of spin systems with a spin magnetization $\boldsymbol{M}$ in the presence of an external magnetic field B_0. Describing the system via Bloch equations makes visualization of magnetization vectors and torques in the resonance condition more intuitive. Moreover, the model helps to explain the absorption and dispersion shape of EPR spectra. The model works with the complex interaction between spins and surrounding by gathering all aspects into two relaxation times T_1 and T_2.
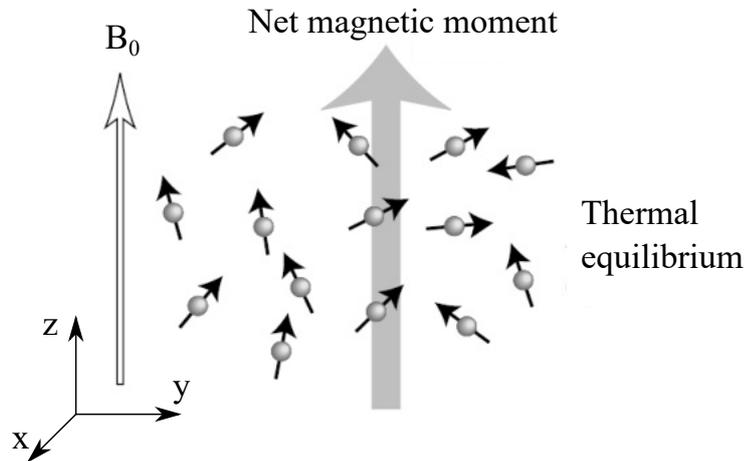
Fig. 2.8: System in thermal equilibrium after exposing to external magnetic field. Magnetization is getting bigger with the increasing external magnetic field. If the external magnetic field B_0 would be equal to zero, the spin moments' sum will result in zero magnetization. Taken from [92].

Transverse T_2 relaxation time: In the presence of a fixed external magnetic field B_0, system magnetization $\mathbf{M}(M_x, M_y, M_z)$ precess in the direction of B_0 with constant angular frequency (named Larmor frequency) $\omega = -\gamma B_0$ (see Fig. 2.8 B) [93]. If the direction of the external magnetic field change, the initial magnetization starts to precess into a new equilibrium, as is shown in Fig. 2.8 A).

$$\frac{dM_x}{dt} = \gamma B_0 M_y, \tag{2.28a}$$

$$\frac{dM_y}{dt} = -\gamma B_0 M_x, \tag{2.28b}$$

$$\frac{dM_z}{dt} = 0, \tag{2.28c}$$

where γ is the gyromagnetic ratio equal to:

$$\gamma_e = \frac{g\mu_e}{\hbar}. \tag{2.29}$$
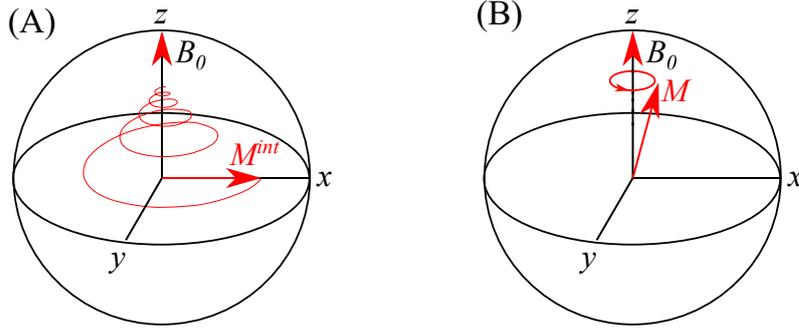
Fig. 2.9: Schematic illustration of magnetization evolution in Bloch sphere. A) Relaxation of initial magnetization M^{int} into a new position parallel to B_0 field. B) Precession of Magnetization M around the B_0 field. In this case, component M_z remains constant.

The solutions of equations 2.28 are:

$$M_x = M_\perp^0 \cos(\omega t), \tag{2.30a}$$

$$M_y = M_\perp^0 \sin(\omega t), \tag{2.30b}$$

$$M_z = M_z. \tag{2.30c}$$

It is visible that the M process at around the z axis (B_0) with constant longitudinal magnetization M_z. When the system is exposed to sudden change of external field, the magnetization M_x, M_y and M_z relax into new equilibrium at different rates. Usually, the transverse components M_x and M_y relax with the same rates which is called *transverse T_2 relaxation time*, and relaxation of M_z is express by T_1:

$$\frac{dM_x}{dt} = \gamma B M_y - \frac{M_x}{T_2}, \tag{2.31a}$$

$$\frac{dM_y}{dt} = -\gamma B M_x - \frac{M_y}{T_2}, \tag{2.31b}$$

$$\frac{dM_z}{dt} = \frac{M_z^{int} - M_z}{T_1}. \tag{2.31c}$$

2.3.3 Rotating frame transformation

If an alternating magnetic field is applied to the system (for example irradiation of spin system by m.w.), it is useful to transform the coordinates to a rotating frame following the continuous precession of magnetization M around magnetic field B_0 with angular velocity ω. In the new system of coordinates, the magnetization is parallel to B_1 (visualization of transitions induced between the magnetic-energy levels, when the oscillating magnetic field is in a direction perpendicular to external magnetic field B_0) and is along new axis x_ϕ (see figure 2.10).
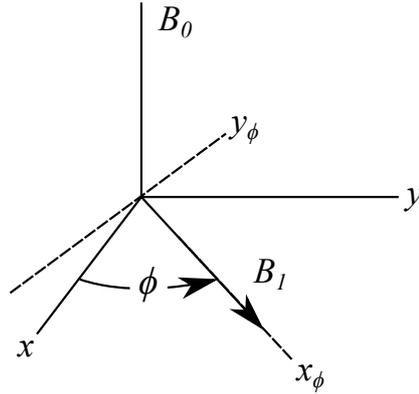
Fig. 2.10: Effective fields in the rotating coordinate system. Taken from [6].

The Bloch equation for the rotating frame are [6]:

$$\frac{dM_{x\phi}}{dt} = -\left(\omega_B - \omega\right) M_{y\phi} - \frac{M_{x\phi}}{T_2}, \tag{2.32a}$$

$$\frac{dM_{y\phi}}{dt} = \left(\omega_B - \omega\right) M_{x\phi} - \frac{M_{y\phi}}{T_2} + \gamma B_1 M_z, \tag{2.32b}$$

$$\frac{dM_z}{dt} = -\gamma B_1 M_{y\phi} - \frac{M_z - M_z^0}{T_1}, \tag{2.32c}$$

where $M_{x\phi}$, $M_{y\phi}$ and M_z are new coordinates of magnetization $\mathbf{M}$ in rotation frame. The differential equations has solution of steady state:

$$M_{x\phi} = -M_z^0 \frac{\gamma B_1(\omega_B - \omega)T_2^2}{1 + (\omega_B - \omega)^2 T_2^2 + \gamma^2 B_1^2 T_1 T_2}, \tag{2.33a}$$

$$M_{x\phi} = -M_z^0 \frac{\gamma B_1(\omega_B - \omega)T_2^2}{1 + (\omega_B - \omega)^2 T_2^2 + \gamma^2 B_1^2 T_1 T_2}, \tag{2.33b}$$

$$M_z = M_z^0 \frac{1 + (\omega_B - \omega)^2 T_2^2}{1 + (\omega_B - \omega)^2 T_2^2 + \gamma^2 B_1^2 T_1 T_2}. \tag{2.33c}$$

The magnitude of transverse components $M_{x\phi}$ and $M_{y\phi}$ are smaller compared to M_z^0. The component $M_{x\phi}$ rotates synchronously with B_1 about the z axis, while the other transverse component $M_{y\phi}$ is phase shifted that it is perpendicular to component $M_{x\phi}$.

This effect of exposing system to oscillating field B_1 can be described also by terms of dynamic susceptibilities χ' and χ''. Therefore, considering the complex magnetic susceptibility:

$$\chi = \chi' + i\chi'', \tag{2.34}$$

where χ' is a dispersive part, a real part of the magnetic susceptibility, χ'' is absorption, the imaginary part of susceptibility. The relation between χ and $M_{x\phi}$ and $M_{y\phi}$ can be written as:

$$\chi' = \frac{M_{x\phi}}{2B_1}, \tag{2.35a}$$

$$\chi'' = \frac{M_{y\phi}}{2B_1}. \tag{2.35b}$$

The term dispersion describes the real part of the magnetic susceptibility, whereas absorption describes the imaginary part. The dispersion phenomenon always accompanies the resonant absorption of energy from the microwave field. It represents a shift in the cavity's resonant frequency (or other resonators) in the spectrometer. Therefore, the phase lock of the spectrometer to the absorption or absorption has a significant impact on the EPR signal shape. Because the absorption is visualized as more narrowed EPR signal (see Fig. 2.11), most commercially available spectrometers have the source frequency-locked to the resonator's resonant frequency, that absorption is dominant in the measurement.

2.3.4 Linewidths

Homogeneous Broadening: Homogeneous broadening is situation, when all spins are affected by m.w. and magnetic field equally. That means that the external magnetic field has the same magnitude over the whole studied sample and all spins have the same spin Hamiltonian parameters. The signal will be a Lorentzian-shaped peak, and it contains information about the effective T_2 relaxation time:

$$T_2 = (\kappa\gamma\Delta\omega_{1/2})^{-1}, \tag{2.36}$$

where $\omega_{1/2}$ is width at half height of peak and κ is a factor depending on the lineshape ($\kappa = 1$ for Lorentzian, $\kappa = (\pi \ln 2)^{1/2}$ for Gaussian).
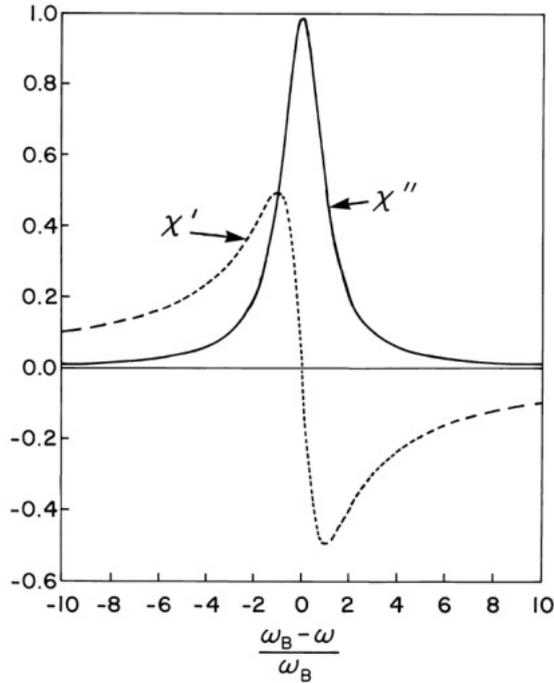
Fig. 2.11: The in-phase (χ') and out-of-phase (χ'') components of the dynamic magnetic susceptibility versus the angular frequency deviation. Taken from [6].

When $T_2 = \infty$ the interaction is negligible and it is assumed that spins are isolated. When $T_2 \to 0$ the spin coupling is very strong (for example ferromagnetic or antiferromagnetic systems).

Inhomogeneous Broadening: Typically, electrons in a sample with an external applied magnetic field B_0 are subjected to a range of magnetic fields due to internal contributions. The EPR signal is then a superposition of a large number of individual components, each one slightly shifted against the other. Another reason for inhomogenous broadening could be the unresolved hyperfine structure of anisotropic interaction in randomly oriented systems such as poly-crystal or powder glasses. One last reason for inhomogeneous broadening can be dipolar interactions with a paramagnetic center. This may impose a random local field at a given paramagnetic electron.

2.4 Methods for studying relaxation times

CW-EPR has many advantages and applications, but it gives limited and mostly indirect information about magnetic relaxation and spin dynamics [94], which plays

an important role in the field of dynamic polarization [17, 18, 95] and quantum computation [19,96]. Generally, to get information about spin dynamics pulsed EPR is used [97–100]. In pulsed EPR, by irradiating the sample with a series of short m.w. pulses, an echo is created as a response from magnetization. Echo measurements can provide T_1 spin-lattice relaxation times and T_2 spin-spin relaxation times [6]. However, pulsed EPR requires high power pulses, which require very expensive m.w. components. In the THz frequency range, such high power devices are solid-state sources [101] or high power klystrons, gyrotrons, and free-electron lasers [102], which besides being expensive are large, the tuning range is usually smaller than 2 GHz and therefore to cover the broader hundreds of GHz range is not possible. The alternative to the pulsed EPR starts to be Rapid Scan EPR. The rapid scan EPR is based on fast frequency/field sweeps, where the sweep rates are fast compared to the spin dynamics times. The fast sweep rate influences the lineshape by "wiggles" (passage effects) which allow the determination of spin relaxation time. So far, there is only one working rapid scan spectrometer worldwide in frequency domain that operates below 95 GHz [103] and recently one in 170-250 GHz range [28]. In generall, pulsed and rapid scan EPR require less time to acquire spectra with comparable signal-to-noise than conventional CW EPR. The comparison between Pulsed EPR, Rapid Scan EPR and Cw-EPR can be found in [65].

This section will introduce the basic introduction into pulsed EPR and theory behind rapid scan.

2.4.1 Pulsed EPR

Pulsed EPR is the most common method to study the relaxation times of spins. The main idea of pulsed EPR is to keep an external field (B_0) constant and irradiate the spin system with a high-power, short microwave pulse. In the simplest experiment, the magnetization is flipped by 90° from z direction to xy-plane. After the pulse irradiates the system, magnetization starts to relax back into the original position, while it is processing about the z-axis at the Larmor frequency (similar to Fig.2.9 A), but the magnetization was flipped into position M^{int} by m.w. pulse). If the EPR homogeneous line is fully excited and following induction in xy-plane is measured, the curve called free induction decay (FID) will be obtained [102] (see Fig. 2.12):

$$Y(t) \sim \exp(e\omega_s t) \exp\left(-\frac{t - t_0}{T_2}\right),\tag{2.37}$$

where ω_s is the Larmor frequency, and t stands for time. The first term describes a circular precession about the z-axis. The exponential decay differs in the relaxation time used from equation 2.37 because the decay of magnetization from the xy-plane is detected here and reading out the voltage induced by the changing M_{xy}.
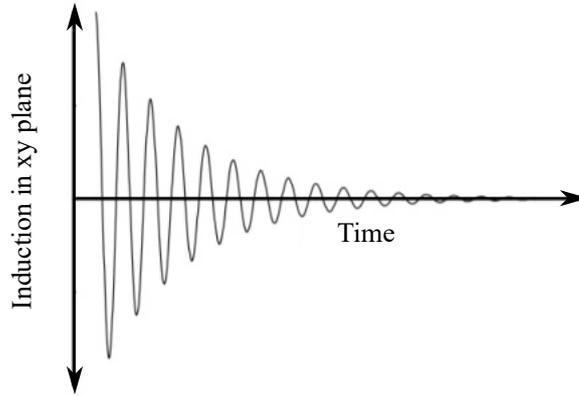
Fig. 2.12: Observable relaxation of xy magnetization M_{xy} after a pulsed excitation. The exponential decay is proportional to T_2. For the first time, it was observed in an NMR experiment by inserting a detection coil into the xy-plane [104].

Generally, a series of pulses is applied to change the magnetization M of the spin system in a convenient way according to the information one wants to obtain [6,51, 69,105]. The first pulse rotates the magnetization, which starts immediately relax to its original state in inhomogeneous dephasing (see Fig. 2.9). This dephasing can be removed by applying a $180°$ inversion pulse that inverts the magnetisation vectors. If the inversion pulse is applied after a period τ, the inhomogeneous evolution will rephase to form an spin echo (Hanh Echo) at time 2τ. To measure the Spin-spin relaxation T_1 or Spin-Lattice relaxation T_2 the different pulse sequence is applied (see Fig. 2.13) [106].

The pulsed EPR experiments in high magnetic fields requires the application of high power m.w. pulses, which is challenging to accomplish. For example, in 9.3 GHz X-band spectrometers (most common EPR spectrometers), the power of up to 1 kW is used. At frequencies above 100 GHz, a spectrometer's typical output power with solid-state amplifiers is not much above 100 mW. Moreover, it is extremely hard to access relaxation times in ns scale because of the spectrometer dead time (time between the end of the excitation pulse and the start of the signal acquisition, which protects the m.w. detector). The experiments and pulsed EPR spectrometer design which reduce the dead time to minimum, can be found in [107–109]. Furthermore, the sample is placed in a cavity to enhance signal to noise ratio. For example, at frequency 263 GHz samples are placed into a capillary with only 30 μm diameter [101].
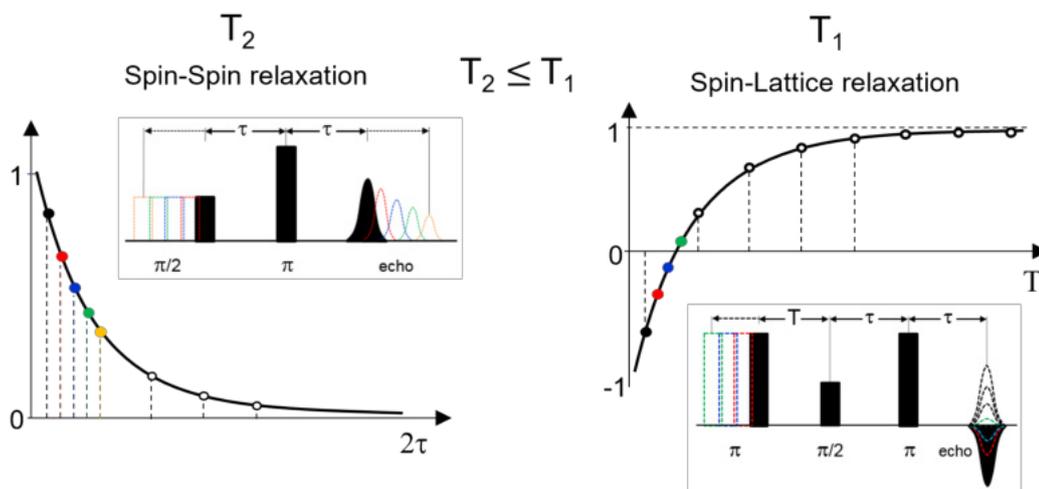
Fig. 2.13: The pulsed sequence of simple experiment for measure spin echo of T_2 and T_1 relaxation time. T_2 represent relaxation of magnetisation in xy plane, whetever T_1 represent relaxation of magnetisation in z plane. After $\pi/2$ pulse and time period τ always follow π pulse which rephase magnetisation dephasing and creates echo signal in time 2τ. Kindly provided by Dr. Petr Neugebauer.

2.4.2 Rapid Scan

The alternative to the pulsed EPR is Rapid Scan (RS) EPR, which gives us access to nanosecond relaxation times in a much broader frequency range [16]. In this method, either the frequency or magnetic field is swept through the resonance faster than the sample's spin relaxation time. The fast sweep rate influences the line shape, creating "wiggles" (RS signal), which allows the determination of the spin dynamics (2.14). In RS is not possible to measure T_1 relaxation, but it measure T_2* relaxation [110]. Then, the relaxation time T_2 can be obtained by fitting the signal with the modified Bloch equations [15,64]. The deconvolution of the RS signal removes "wiggles" giving a non-distorted EPR absorption spectrum.

This work is focused on developing frequency domain RS, which has several advantages over the pulsed EPR and field domain EPR. Frequency domain RS is not limited by sweeos coils, therefore it has much broader operating range (tens of GHz) with the absence of a dead time (in which the detector is protected from the m.w. source's high power). Therefore, RS can sweep measure extremely fast 61 500 THz/s (which would corresponds to impossible sweep of 349 kT/s in field domain RS) giving access to T_2 relaxation times in ns range at any frequency within the spectrometer's frequency range with low power source (mW). Additionally, sample holders without resonating cavities lift the limitations of sample size but on the other hand, lack of cavity decrease the sensitivity [27]. Moreover, the absence of

eddy currents and heat created by sweeping coils in field domain RS allows the experiments in frequency domain RS to be performed at low temperatures [28, 110].

Modified Bloch equation: Bloch equation were introduced in the section 2.3.2, with their steady state solution. The steady solution describes the slow passage through the resonance to observe an absorption 2.11. In RS-EPR, the fast passage through resonance is applied, which allows for observation of relaxation effects ("wiggles"). The main condition to observe wiggles is that passage (of frequency f or field B_0) has to be faster than the relaxation time of the system:

$$\gamma \left| \frac{dB_{ext}}{dt} \right|, \left| \frac{df}{dt} \right| \geq \frac{1}{T_2^2}. \tag{2.38}$$

The RS wiggles are the result of the beating process of two oscillations: B_1 excitation via microwave oscillation (in field domain, it is the oscillation of magnetic field B_0) and magnetization oscillation of the spin system. The number of wiggles is proportional to the difference in the frequencies of the two oscillations. The rapid scan signal $r(t)$ is described as convolution of slow-scan signal $s(t)$ and drive function of the excitation $d(t)$:

$$r(t) = (s * d)(t) = \int_{-\infty}^{+\infty} s(\tau)d(t - \tau)d\tau. \tag{2.39}$$

The solution to the equation through convolution is complex. However, applying the Fourier transformation, the convolution operator is transformed to the multiplication operator, thus equation 2.39 becomes:

$$R(\omega) = S(\omega)D(\omega), \tag{2.40}$$

where $R(\omega)$, $S(\omega)$ and $D(\omega)$ are operators $r(t)$, $s(t)$ and $d(t)$ in Fourier space ($t \rightarrow \omega$). In this form can be calculated driven function easily, because it depends on experimental setup:. Generally, the drive function is:

$$d(t) = \exp\left(\int_0^t \omega(\tau)d\tau \right), \tag{2.41}$$

where $\omega(\tau)$ is the waveform of the sweep. If the sweep is linear then: $\omega = b\tau$, b is the sweep rate in rad/s^2 results into

$$d(t) = \exp\left(\frac{ibt^2}{2} \right) \Rightarrow D(\omega) = \exp(-i\omega^2/2b). \tag{2.42}$$

If the sweep is broad enough comparable to signal, sweep as sine waveform can be approximated by a linear function. Then the b is equals to the maximum sweep rate ($2\pi A_{mod} \times f_{mod}$, A_{mod} is modulation's amplitude and f_{mod} modulation frequency)

occurring in the center of sinusoidal scan. Then, for obtaining the relaxation time T_2 it is necessary to simulate rapid scan spectra by solving a modified system of Bloch equations [28, 111–113]:

$$\frac{dM_x}{dt} = -\frac{M_u}{T_2} - [\Delta\omega + A_{mod}\cos(2\pi f_{Mod}t)]M_v, \tag{2.43a}$$

$$\frac{dM_v}{dt} = -\frac{M_v}{T_2} + [\Delta\omega + A_{mod}\cos(2\pi f_{Mod}t)]M_u - \gamma B_1 M_z, \tag{2.43b}$$

$$\frac{dM_z}{dt} = \frac{M}{T_1} + \gamma B_1 M_y - \frac{M_z}{T_1}, \tag{2.43c}$$

where $\Delta\omega$ is offset of a spectrum from the center of the sweep, M_u, M_v, and M_z are projection of the total magnetization M. The example of measured freqeuncy domain RS signal with the simulation is shown in Fig.2.14.
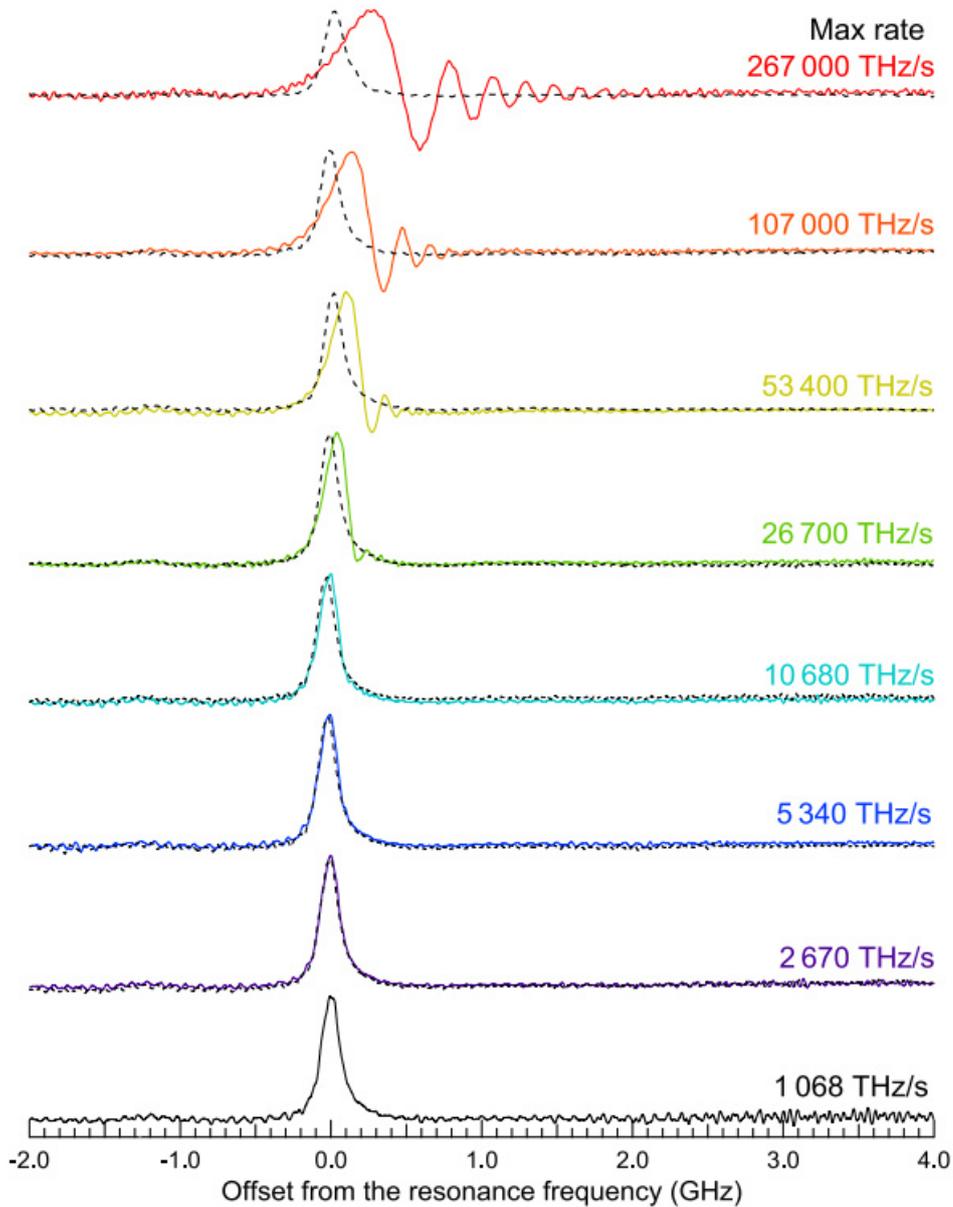
Fig. 2.14: The effect of different frequency sweep on LiPc spectra. Rapid scan spectra of the LiPc sample recorded at the fixed field of $8\,\mathrm{T}$, temperature of $13\,\mathrm{K}$ and several modulation frequencies, 20, 50, 100, 200, $500\,\mathrm{kHz}$, 1, 2, $5\,\mathrm{MHz}$, and constant modulation amplitude of $8.5\,\mathrm{GHz}$. Each trace is labeled by the maximum sweep rate achieved at the center of sweep. Dashed curves are the deconvoluted spectra. Taken from [28].

3 HF-EPR instrumentation

This chapter introduces the concept of cw-EPR at high magnetic fields and frequencies. The text gives an overview of the overall assembly of cw-EPR, m.w. sources, detectors, magnet, and m.w. propagation solution. Although this chapter describes the general EPR spectrometer scheme, most of the text is bound to the development of the HF-EPR spectrometer operating in frequency and magnetic field domain and able to perform rapid scan measurements at CEITEC.

3.1 General design

There are five general requirements for a cw-EPR spectrometer [51]: 1) The magnetic field has to be stable and homogeneous. 2) the m.w. source has to have enough power, produce a low level of noise, and a stable m.w. phase as well. 3) The m.w. propagation solution should have low m.w. power losses. 4) The sample holder must concentrate the incident m.w. radiation onto the sample, allowing detection of the small amount of energy absorbed or emitted when the EPR resonance condition is met. 5) The detector should have low noise floor to enable a high signal-to-noise ratio (SNR). If these conditions are met, the absolute detection sensitivity is determined by the minimal number of detectable spins:

$$N_{min} \propto \frac{V_s T_s}{\eta Q} \left(\frac{\Delta f_{pp}}{f_{ex}} \right) \left(\frac{\Delta B_{pp}}{B_{mod}} \right) \left(\frac{P_{System}}{P_W} \right)^{1/2} , \qquad (3.1)$$

where V_s and T_s are the volume and temperature of the sample, Q is unloaded quality factor of the cavity, η is filling factor ($\eta \approx V_s/V_c$), f_{ex} is irradiation frequency, Δf_{pp} and ΔB_{pp} is peak-to-peak EPR linewidth ($\Delta f_{pp} = \gamma_e \Delta B_{pp}$). B_{mod} is the modulation amplitude, P_W is the incident m.w. power and P_{system} is the effective noise power and is given by $P_{system} = \Delta f$ k T_d , where Δf is the effective detection bandwidth and T_d is the effective noise temperature of the spectrometer system.

Important characteristics of m.w. sources are amplitude noise and phase noise. The amplitude noise describes fluctuation of incident m.w. power level and phase noise is related to the offset of the m.w. frequency from the carrier frequency. Under certain conditions, the source noise can overcome the detector noise and limit the sensitivity of the cw-EPR detection. A detailed description of these noise influencing EPR measurements can be found in references [62] and [114].

HF-EPR spectrometer: The schematic drawings of the cw-HF-EPR spectrometer with homodyne or heterodyne detection scheme is shown in Figure 3.1. There are different EPR detection schemes, but for our purposes, we will only deal with

homodyne and heterodyne detection schemes. Description of other configurations can be found elsewhere [51, 115, 116].
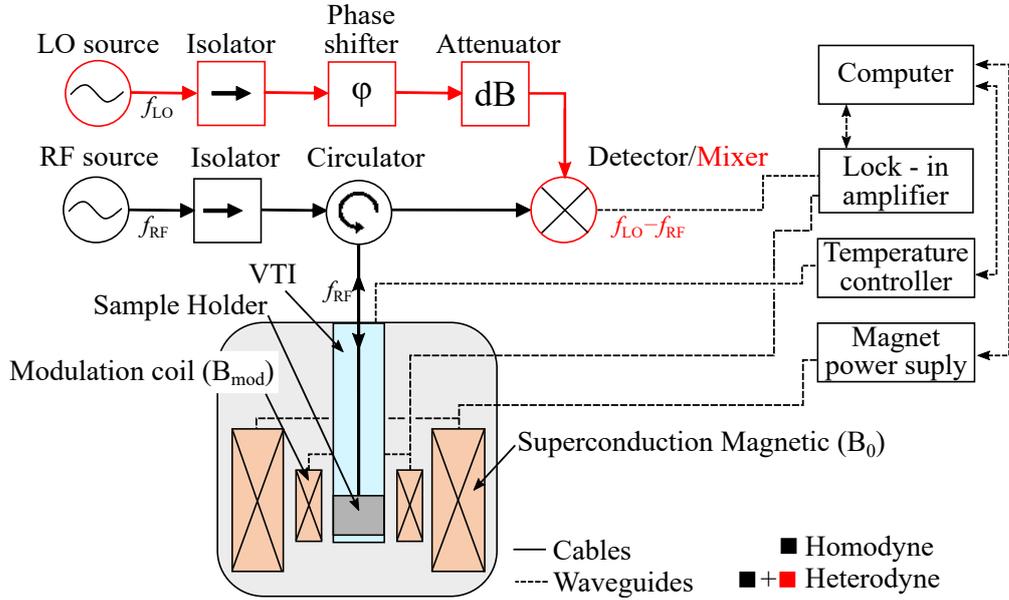
Fig. 3.1: The scheme of cw-HF-EPR spectrometers with heterodyne or homodyne detection.

Conventional homodyne cw-EPR employs a continuous microwave source (RF source) to irradiate samples located in the sample holder, which is placed inside a magnet cryostat. The m.w. is generated by RF source (part of the RF sources are often multipliers which upconverting generated frequency), and propagates to the sample through a circulator. Circulator is a passive device with three or four ports that allows a m.w. to exit through the port next to the one it entered. It protects the sensitive m.w. sources to be damaged from back-reflected m.w.. The mirror located under the sample reflect m.w. back to circulator and to the mixer (heterodyne detection) or directly to the detector (homodyne detection (see Fig. 3.1). To increase the EPR signal, the m.w. passes through the sample two times (radiated m.w. from source and reflected m.w. from mirror), *double pass configuration*. For optimum sensitivity, the sample holder is exactly aligned to the transmission line waveguide in the way that all the incident m.w. power interacts with the sample. Furthermore, a small modulation coil is placed around the sample for SNR enhancement.

The more common EPR configuration is homodyne detection. Homodyne detection uses only one source and one detector (see Fig. 3.2). The advantage of homodyne setups is lower construction demands. The second configuration, heterodyne detection uses also a second source, *Local Oscilator* (LO Source), and mixer.

An attenuator is typically connected to the Lo source to avoid mixer saturation. The excitation m.w. (from RF source) carrying EPR signal with the signal from the local oscillator source (LO) are mixed, which resulting intermediate signal (IF) is produced (see Fig. 3.2):

$$A\cos(2\pi f_{LO}t) \times B\cos(2\pi f_{RF}t) = \frac{AB}{2}\left[\cos(2\pi(f_{LO} - f_{RF})t) + \cos(2\pi(f_{LO} + f_{RF})t)\right]$$
(3.2)

After mixing, result consists of high and low-frequency signals. By applying a low pass filter, the output product of the detector will be a low-frequency signal carrying the EPR information from the sample. In this way, signals carried by high frequencies can be converted to low frequencies. Heterodyne detection is frequently used for high frequencies EPR because high frequencies low noise amplifiers are expensive and not so common.
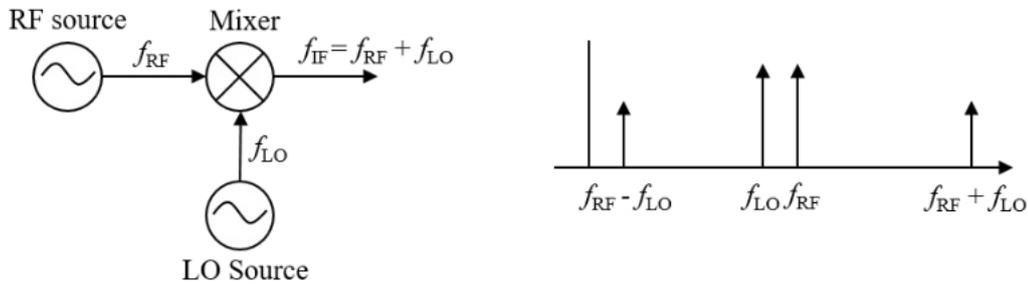
Fig. 3.2: Scheme of heterodyne mixing frequency functionality. In most spectrometers, down conversion is used to decrease the input frequency.

Systems with heterodyne detection have more components and thus are more complicated to build and optimize. On the other hand, they should theoretically achieve higher sensitivity than a system with homodyne detection, because of lower noise level and downconverting m.w. frequencies to lower frequencies, where low noise amplifier and filters are available [51].

Microwave source: Nowadays, X- or Q-band spectrometers use solid-state sources like in higher frequency spectrometers. To generate high frequencies, one can use low-frequency sources (10 GHz range phase-locked synthesizer) in combination with a series of active or passive frequency multipliers. This approach can deliver an operation range of 90–1100 GHz [33]. The problem with this solution is the performance of the sources at high frequencies. At frequencies above 300 GHz, the power drops below one milliwatt. Another m.w. source for broadband high field spectrometer is the photoconductive antenna (PCA) based m.w. emitters [117]. The other

solution for high-frequency m.w. sources is to employ gyrotrons [118], solid-state sources [116], far-infrared (FIR) lasers [48], backward wave oscillators (BWO) [119], free electron laser [102] which offer a very large excitation power but their use is rather rare due to their dimensions, complicated operation and high costs.

Microwave detector: The Detector in EPR spectroscopy typically acts as a device to transform m.w. radiation to signals of lower frequencies (typically DC) which can be fed into a recording device. In order to measure well-defined, low noise spectra, detectors need to have high sensitivity with low intrinsic noise, and furthermore, their dynamic range must be large enough to register intense signals. Bolometers are devices based on the conversion of m.w. power into heat that is detected as a change in resistance [120]. The biggest advantages of bolometers are a broad range of detection (from GHz to THz radiation) and low base-noise levels. However, on the opposite side, bolometers are very slow in the detection and for good performance have to be cooled down to cryogenic temperature. One of the fastest bolometers applied in astronomy has a response time around 42 ms [51]. Such response time is unacceptable for our system where the scan of the spectrum takes a few ms. The development of bolometers is still in progress, and InSB bolometers show responses in μs range [121].

The second type of detectors, the diode detectors, are typically the Schottky-barrier type. The diodes flourish where bolometers fail. Schottky diodes have a ns response time and do not require cryogenic cooling. Moreover, they can detect m.w. frequencies up to the THz region. However, it is very complicated to work with the signal of high frequency. Even nowadays, there are no suitable low noise components on the market that could work with high-frequency signal. Special care should be given to the phase noise in heterodyne systems, which is generally higher than in homodyne systems. In heterodyne, the noise is reduced by phase-lock the excitation and local oscillator source to one stable oscillator (master reference). Generally, to obtain the highest signal-to-noise ratio in high field/frequencies EPR heterodyne detection is implemented with an intermediate frequency sufficiently large to eliminate $1/f$ noise from the Schottky diode.

Magnet: Magnet systems in EPR are the foundation for well-performing experiments. The magnets have to generate a homogeneous static magnet field at the sample's position. The stability should be higher than the EPR linewidth to avoid EPR line broadening. Moreover, the range of the produced magnet field must cover the full EPR spectrum range. Generally, the X-band EPR spectrometer has an electromagnet with the field going up to around 1 Tesla. However, a HF-EPR spectrometer needs higher fields, in the range of 10 T and more to fulfill the resonance

condition. The resonance condition shows that the irradiation frequency ratio to the magnetic field scales as $28\,\text{GHz/T}$ (for $g=2$), comprising the microwave (m.w.) range. High fields magnets are often based on low-temperature superconductors, which require liquid He as a cooling medium. Sometimes, high-power resistive magnets are employed for a field greater than 20 T.

Typically, the magnets are equipped with the cryostat for sample cooling, which is cooled down by liquid helium. Modern cryostats are called VTI (Variable Temperature Insert). The VTI ensemble enables controlling the temperature of the sample from 1.5 K up to 300 K and more. However, employing a VTI raises the m.w. propagation problem to the sample and back to the detector. Therefore, special care has to be taken with waveguides.

3.2 HF – EPR transmitting system

In HF-EPR development, the low-loss transmitting system is critical. A low-loss m.w. transfer system, which operates in a broad frequency range, has been one of the aims of EPR development for decades. In X-band spectrometer ($9.6\,\text{GHz}$), the transmission line is made of rectangular waveguide WR90, which attenuates the power by $0.1\,\text{dB/m}$. For a typical X-band transmission line length of $1\,\text{m}$ such loss does not disturb the outcomes significantly. However, at high m.w. frequencies, a transmission lines are generally longer, and losses in standard rectangular lines are higher. For example in our case, the pathway distance source to the detector is around $3\,\text{m}$. At $140\,\text{GHz}$ the rectangular waveguide WR7 attenuates by $5.6\,\text{dB/m}$ at room temperature [51]. One of the general solutions for a low loss system is to used an oversized waveguide [122]. Therefore, Gaussian Quasi-Optical (QO) approach is often used in the design of HF-EPR spectrometers.

Since the late 1980s, several groups have begun replacing waveguides in their HF-EPR systems with a more efficient quasioptical system for microwave propagation which soon become standard in HF-EPR spectrometers [33, 49, 55, 102, 123]. This method considers both ray-like and diffraction-causing optical phenomena when tracing the beams as they interact with the surfaces of optical elements and the matter in the pathway. The optimized m.w. transfer systems operating in free space can have negligible damping of dB/km (damping is mostly caused by molecular air absorption). The overall benefits of the QO approach for HF-EPR are numerous [51, 122]:

- Accurate determination of m.w. propagation in the EPR system.
- Achievable Low-loss transmission (250 GHz, $1{,}5\,\text{dB/m}$ in free space versus $12\,\text{dB/m}$ in waveguide WR4 [51]).

- Possibility to create the basic components usually used in a classical EPR spectrometer while maintaining the same properties.

3.2.1 Gaussian beam

The components of a Quasi-optical table, such as mirror, polarize, or horn antennas, can be described in Gaussian beam modes and Gaussian beam propagation theory. Therefore, the basic formulas of Gaussian beam description will be introduced in the following text.

To be able describe the system by the fundamental Gaussian beam (see Fig. 3.3), an angular divergence of the beam from the propagation axis should be smaller than 0.5 radians (about 30°). This statement is so-called paraxial approximation for the collimated wave. Paraxial approximation has to fulfill two assumptions. Firstly, the variation of the wavefront beam amplitude is small over a distance comparable to the wavelength. Secondly, the variation of the wavefront beam amplitude should be smaller than the variation perpendicular to the propagation axis. Then equation which describes a diverging beam with a minimum diameter at $z = 0$ is:

$$u(r, z) = \frac{\omega_0}{\omega} \exp\left(\frac{-r^2}{\omega^2} - \frac{i\pi r^2}{\lambda R} + i\varphi_0\right), \tag{3.3}$$

where ω is the distance from the beam axis where the amplitude has reached $1/e$ times that on the axis.

Then, the fundamental Gaussian beam is described as:

$$z = \frac{\pi\omega_0,^2}{\lambda} \tag{3.4}$$

$$R = z + \frac{1}{z}\left(\frac{\pi\omega_0^2}{\lambda}\right)^2, \tag{3.5}$$

$$\omega = \omega_0\left(1 + \frac{\lambda z}{\pi\omega_0^2}\right)^{1/2}, \tag{3.6}$$

$$\tan\varphi_0 = \frac{\lambda z}{\pi\omega_0^2}, \tag{3.7}$$

where R is the wavefront radius, ω is the radius at which the electric field falls to $1/e$ relative to its axial maximal value at the position z. ω_0 is the minimal radius of the beam, called beam waist, φ_0 is phase shift. For better understanding see Fig. 3.3.
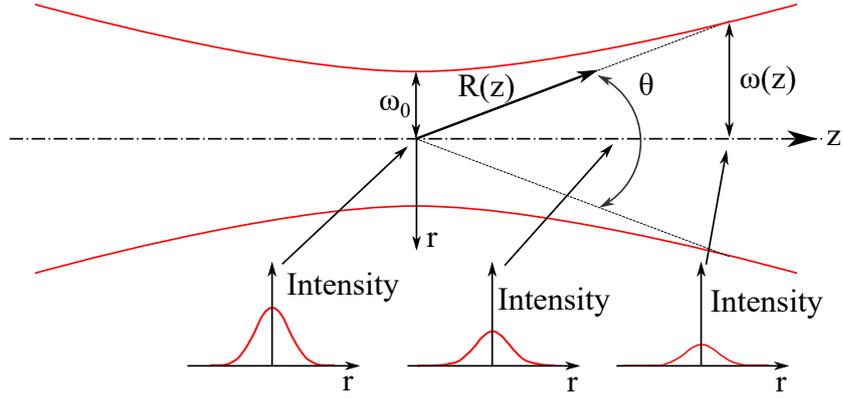
Fig. 3.3: Schematic picture of the Gaussian beam propagation with the cuts in different z positions.

The normalised intensity of electric field distribution E(r,z), shown in Fig. 3.3, can be expressed as:

$$E(r, z) = \left(\frac{2}{\pi\omega^2}\right)^{1/2} \exp\left(\frac{-r^2}{\omega^2} - ikz - \frac{i\pi r^2}{\lambda R} + i\varphi_0\right). \qquad (3.8)$$

The equations 3.5 to 3.8 describe the behavior of the fundamental Gaussian beam mode in the paraxial region completely. It is the simplest fundamental wave equation solution, which is typically used for calculation. That is a good approximation for the "large" lenses and mirrors, where the wave is attenuated minimally. In some cases, a more complex electric and magnetic field distribution perpendicular to wave propagation is used. Such solutions are called higher-order Gaussian modes. More information about the Gaussian beam propagation theory can be found in [122].

3.2.2 Gaussian beam coupling

Modern HF-EPR spectrometers can be divided into two parts: an EPR table with m.w. source and detector; and an EPR probe, consisting of a waveguide and the sample (see Fig 3.4). The sample is placed in the center of the magnetic field of a superconducting magnet. During the process of sample changing, the EPR probe is pulled out of the magnet. Then, the EPR probe with a new sample is again inserted into the magnet and the m.w. beam from the EPR table has to be coupled with the EPR probe. Therefore, it is essential to understand the coupling between two Gaussian beams (the function of power transmitted from the EPR table to the probe), to avoid attenuation EPR signal.

Imperfect coupling, describing how much power is transferred from beam a into
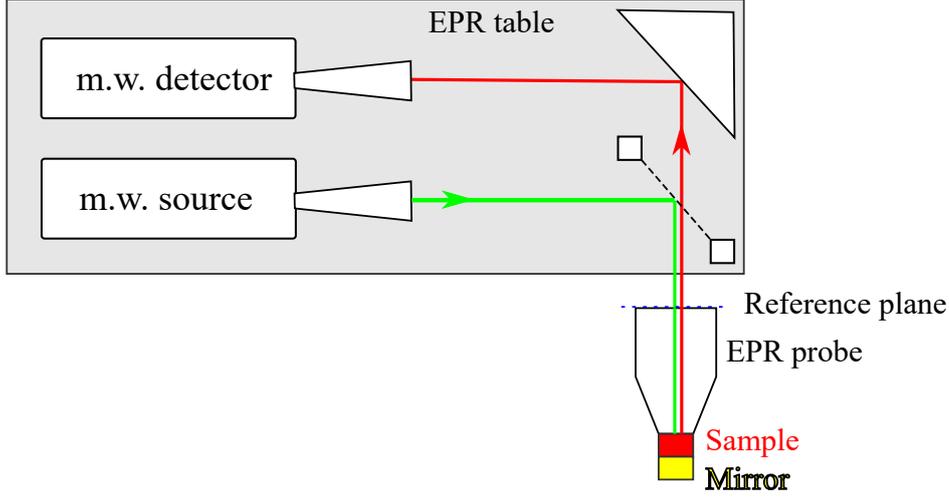
Fig. 3.4: Scheme of arrangement for coupling in our spectrometer. The sources and detectors are located on the table. The beam is led by quasi optics components to the corrugated probe, which is placed in a magnet. The sample holder is attached at the bottom end of the probe.

beam b, is defined by coupling coefficient:

$$c_{ab} = \int \int \psi_a^* \psi_b \, dS. \qquad (3.9)$$

The integration is taken over the plane perpendicular to optical axes where the beam waists are located, the so-called reference plane. Because we are interested only in power transmission, we will assume that the polarization states of the incident and reflected beam are the same. Both beams are propagating in the same direction with no phase shift. We can rewrite the equation 3.9 into:

$$c_{ab} = \int \int u_a^* u_b \, dS. \qquad (3.10)$$

Two dimensional filed coupling coefficient is then obtained:

$$c_{ab}^2 = c_{ab}^{1x} c_{ab}^{1y}. \qquad (3.11)$$

Then, the fraction of the power that is coupled from beam a into beam b is given by power coupling coefficient:

$$K_{ab} = |c_{ab}^2|^2. \qquad (3.12)$$

There are three main Gaussian beam misalignments shown in Fig. 3.5:
- The beams are axially aligned, symmetric around the optical axis and they have the same beam waist. The coupling coefficient can be obtained from the

longitudinal displacement, where Δz is the distance between the beam waists ω_0 along the axis:

$$K_{\text{long}} = \frac{4}{4 + (\lambda \Delta z / \pi \omega_0^2)^2}. \qquad (3.13)$$

- The beam waists perfectly match but suffer from a mismatch of their axes position:

$$K_{\text{offset}} = \exp\left[-2\left(\frac{x_0}{\omega}\right)^2\right]. \qquad (3.14)$$

- The beam waists perfectly match but suffer from mismatch of axes in small angles θ:

$$K_{\text{tilt}} = \exp\left[\left(\frac{\pi \theta \omega_0}{\lambda}\right)^2\right]. \qquad (3.15)$$
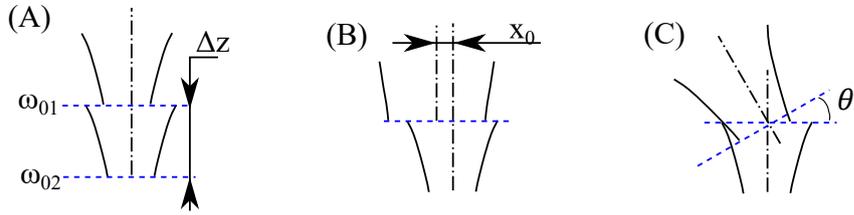

Fig. 3.5: Three general cases of Gaussian beam misalignment, where the dotted lines mark reference planes. (A) Axially aligned beams with offset waists Δz, (B) radially offset beams of x_0, (C) tilted beams by an angle θ.

The expressions derived above allow one to estimate how critical each alignment parameter $(\Delta z, \Delta r, \theta)$ is at various places in the QO transfer line. In our case, the manual coupling is realized between the EPR probe and the EPR table since the transfer line components on the optical board are mounted entirely independently from the EPR components in the magnet bore (see Fig. 3.4).

In Fig. 3.6, the frequency dependence of the coupling between our EPR probe and EPR table is shown. The coupling error in an angular mismatch is dominant primarily at high frequency. The error of 1.7 degrees can cause almost complete attenuation of m.w. at 600 GHz. In contrast, longitudinal mismatch has a higher impact at lower frequencies. The lateral offset has minimal impact on beam coupling and is independent of frequency. In Fig. 3.6, the huge Δz offset of 150 mm was used for demonstration, and still, the coupling coefficient is high. Therefore, one can assume that Δz offset plays a minor role in beam waist coupling. The result that a small beam waist is less sensitive to angular misalignment at first seems not right, but it can be deduced from the inverse dependence of the beam growth angle on the beam waist [122]. Therefore, less divergent beams are more sensitive

to angular deviations of the optical axis. From this discussion, we conclude that longitudinal deviations are uncritical, the lateral offset will be easy to avoid, but angular deviations are extremely critical. More information about a quantitative analysis of the beam coupling can be found in [124].
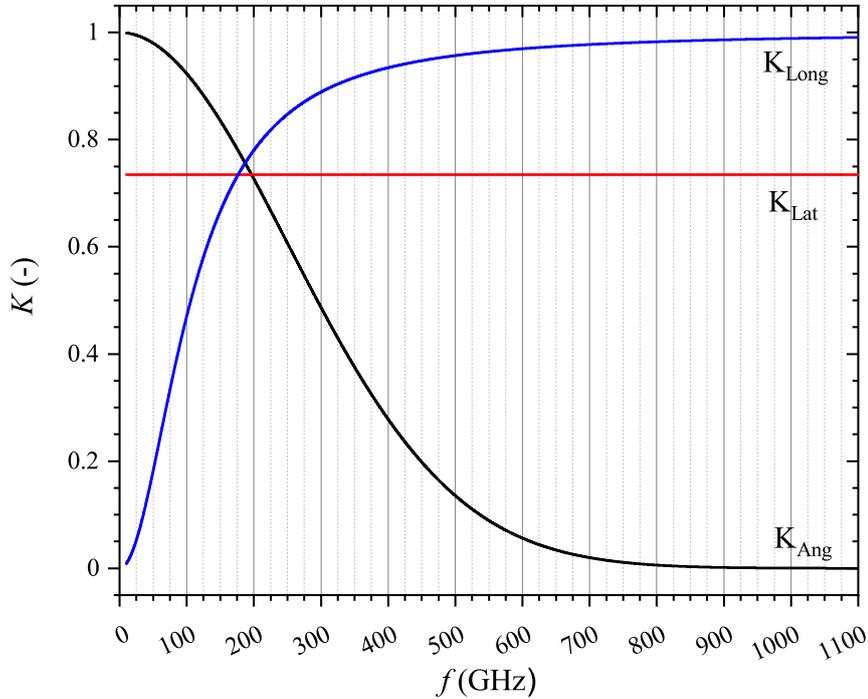
Fig. 3.6: Power distribution for different coupling errors. Parameters for calculation: beam waist $\omega_0 = 9\,\text{mm}$, Longitudinal displacement $\Delta z = 150\,\text{mm}$, Lateral displacement $\Delta h = 5\,\text{mm}$,Angular displacement $\Delta\phi = 0.03\,\text{rad}$.

3.2.3   QO components

Mirrors, polarizing wire grid, Faraday rotators, and corrugated horns are employed in our system. Therefore, they are introduced in the following text.

Mirrors: In QO systems, mirrors are used more often than lenses for several reasons. One of them is their non-disperse behaviour, which allows designing a QO system with a broader frequency range. The metallic mirrors are typically made of aluminium and they reflect and focus m.w. with negligible losses. On the other hand, lenses need an anti-reflect coating to reach similar performance. Mirrors are

also usually arranged in an off-axial manner thus suppressing unwanted standing waves. The design of the system has to be done carefully to minimize polarisation errors as well as beam distortion [122].

Ferrite: Ferrite, one type of Faraday rotators, rotate the polarization of m.w. by a given angle. The behavior of traveling m.w. though the Ferrite is independent of m.w. propagation direction. The direction of the polarization rotation is the same for m.w. propagation in "forward" and "backwards" directions (see Fig. 3.7).
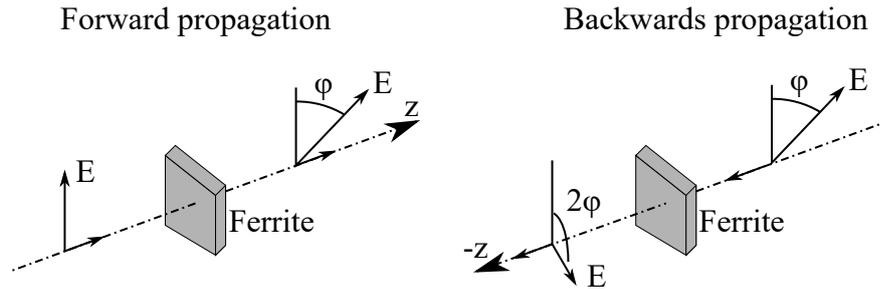

Fig. 3.7: Schematic drawing of beam propagation through Ferrite. The output of the rotation angle of polarization is independent of m.w. propagation direction. Therefore, the output of 45° ferrite rotation is for m.w. going "forward" and the same m.w. going later "backward" direction has polarization rotate by 90°.

Ferrites are made by sintering a compound of metallic oxides, which creates high electrical resistance and dielectric constant ($\epsilon \geq 10$). The product of the magnetic moment of an individual spin and the number of spins per unit volume results in the magnetization M of the ferrite [122]. The rotation angle θ produced by propagating a distance L of m.w. in Ferrite is given by:

$$\frac{\theta}{L} = 2.93 \; n_f \; \mu_0 \; M_s, \tag{3.16}$$

where n_f is the refraction index of the Ferrite, M_s is saturated magnetization, the number 2.93 is a result of $e/2\,c\,m_e$ in which e is electron charge, m_e is mass of electron and c is speed of light. Well performing Ferrite materials have saturation magnetization M_s of 0.1 to 0.4 T, which give a few radians per centimeter rotations. For most applications, the Faraday rotator length is designed to change polarization by 45°. In that case, we can rewrite the equation 3.16 into:

$$L_{45} = \frac{\pi}{n_f \mu_0 M_s}. \tag{3.17}$$

Typically the thickness of ferrite starts from 0.2 cm [122].

Polarizing Grids: Another QO component in our HF-EPR system is a polarizing grid. It transforms polarized radiation into the orthogonal linearly polarized component m.w. of frequencies below 3 THz (see Fig. 3.8). It is made of thin metallic round wires or stripes, typically tungsten or stainless steel, welded in metallic frames. To ensure the straightness of wires, they are stretched to the point just before breaking. The specific size of wires a are in the line with certain spacing g. The general rule for wire grids is that the spacing between the wires must be significantly smaller than $\lambda/2$ of the incident beam.
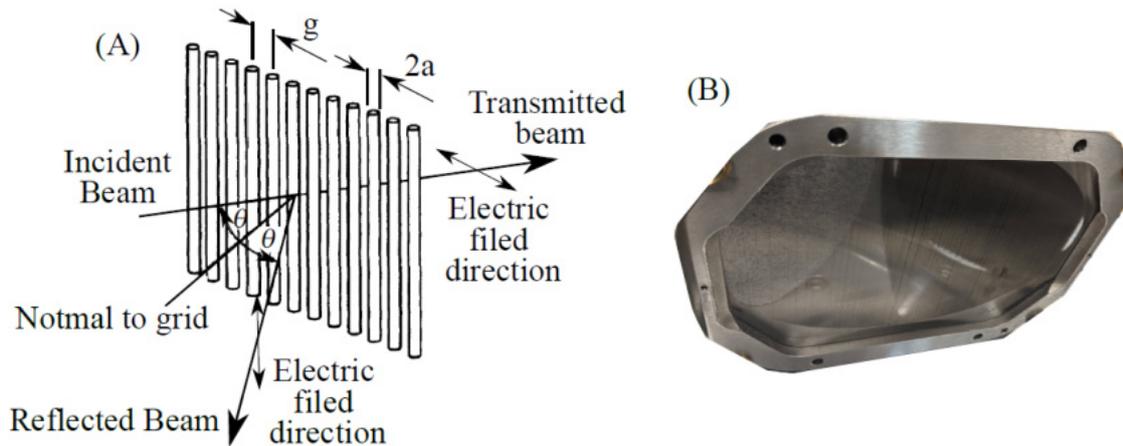
Fig. 3.8: A) The drawing with illustrative description of wire grid function. Taken from [122]. B) The picture of the wire grid which is mounted on the HF-EPR table.

In our system, we are using a wire grid of tungsten wire of $5\,\mu$m diameter with spacing $10\,\mu$m. This set of parameters gives us well-working wire grid polarizers up to 3 THz.

Quasi-Optical circulator: The QO circulator serves to control m.w. propagation in almost every EPR spectrometer. It is consisted of a set of polarizers and Faraday rotators (see Fig. 3.9) [125]. Its basic role is to modify and differentiate m.w. propagation to get multi-port output or input from source to sample cavities and detectors. The most common application of QO circulator in HF-EPR is to isolate source from back-reflected m.w. beam, in the induction mode implementation, and combining LO beam with RF beam before it is fed into the mixer.

Corrugated waveguide: A corrugated waveguide is often used at frequencies above 100 GHz, which provides low loss transmission in the area with limited space as the case of the cryostat. Moreover, they are used as horns and antennas [122]. The corrugated waveguide is formed by a circullar metallic waveguide with grooves on
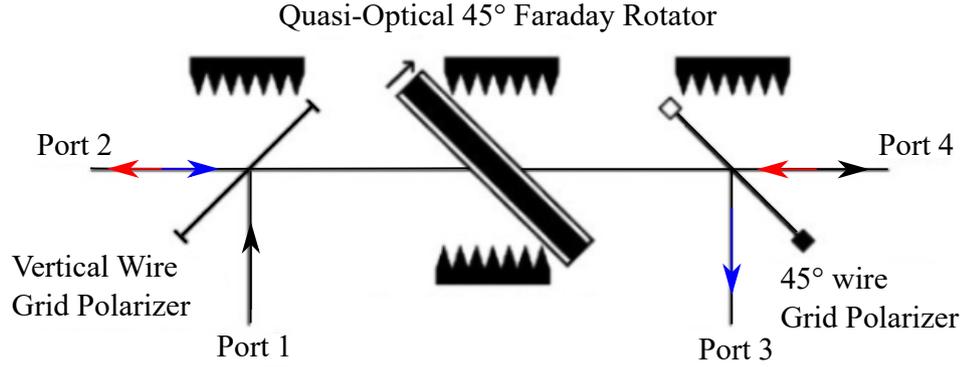
Fig. 3.9: Schematic of a QO circulator based on a Faraday rotator and two wire polarizers. A vertically polarised m.w. (red) inputs in Port 1 leaves −45° polarised at Port 4. The m.w. reflected back, which enter Port 4 with 45° (black) polarization leave the setup in port 2. And the same m.w. which is reflected back and enters Port 2 (blue) with horizontal polarization leaves by Port 3 with −45° polarization. Taken from [125].

the inner side, which dimensions are smaller than the wavelength 3.10 (If the grooves are larger, the corrugated waveguide serves as an attenuation line).

For our present purposes, we can consider that propagates the hybrid HE_{11} mode, where the period of the grooves is much less than a wavelength (typically < lambda/3) to achieve low loss transition. The deeper treatment of corrugated feed horn is complex and can be found in [122]. The benefits of corrugated waveguides used instead of the smooth waveguide are mainly negligible losses in transmission ($\approx 1\%$ per 100 meters), large bandwidths at the HE_{11} mode (up to 8:1 to others Gaussian mode), it is also a good choice for high-power transmission (up to 1 MW in the air).
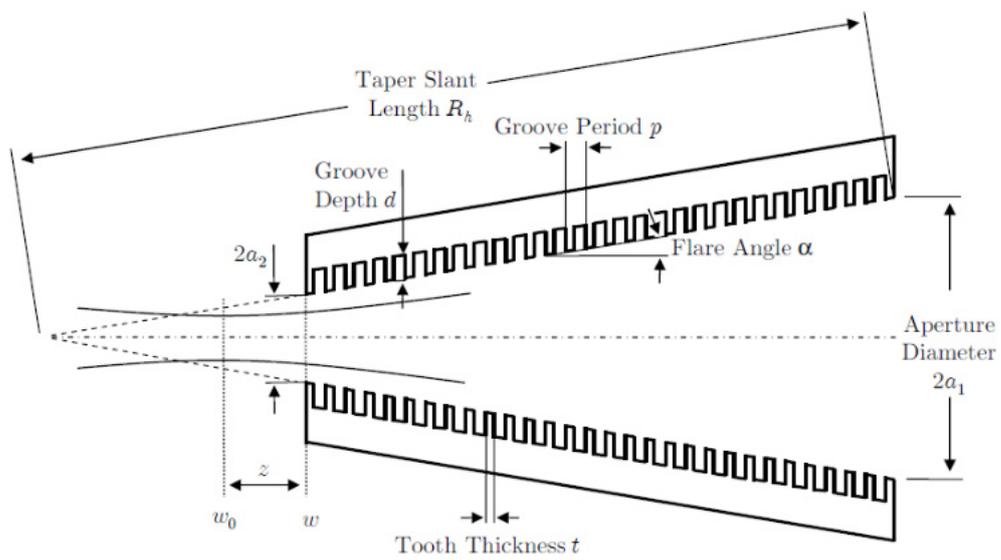
Fig. 3.10: Cross section of corrugated feeding horn. Taken from [82].

4 FRaSCAN EPR

This chapter describes the design and development of the sub-THz Frequency Rapid Scan (FRaSCAN) EPR spectrometer (see Fig. 4.1), the main task fulfilled for the writing of this thesis. The chapter is divided into four sections describing the overall description and individual three main parts of the spectrometer: Magnet Frame, EPR Table, and EPR probe. The assembly drawings main parts are in Appendix B.

Tab. 4.1: Parameters of FRaSCAN EPR spectrometer:

Frequency Range	m.w. power	Magnetic Field	VTI Temperature
$(82 - 1100)\,\text{GHz}$	$(100 - 0.003)\,\text{mW}$	$(0 \pm 16)\,\text{T}$	$(1.8 - 400)\,\text{K}$
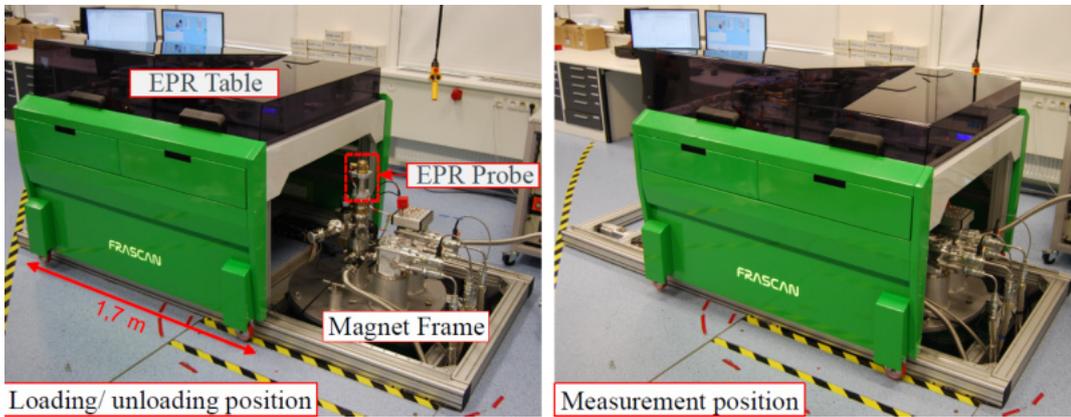
Fig. 4.1: The photograph of FRaSCAN EPR spectrometer in position for loading/unloading of the probe and measurement position. The picture was taken in June 2020.

Overall design: The FRaSCAN EPR spectrometer is spectrometer working in the induction mode, and with heterodyne detection. To perform the EPR measurement, firstly, the probe with a sample is inserted into the magnet. After that, the EPR table moves above the magnet into the measurement position where the m.w. beam from the EPR table is precisely coupled to the EPR probe (see Fig. 4.1). The main spectrometer specifications are listed in the table 4.1. It can work in the field domain with maximal constant ramp speed to $15.5\,\text{T}$ is $3\,\text{mT/s}$, and in the frequency domain with sweep rate $14\,\text{ms}/1\,\text{GHz}$ (or $90\,\mu\text{s}$ per 25 MHz for sweep over less than 50 MHz) simultaneously. Therefore, spectrometer is capable of measuring EPR maps, and HF-frequency domain rapid scan over a wide range.
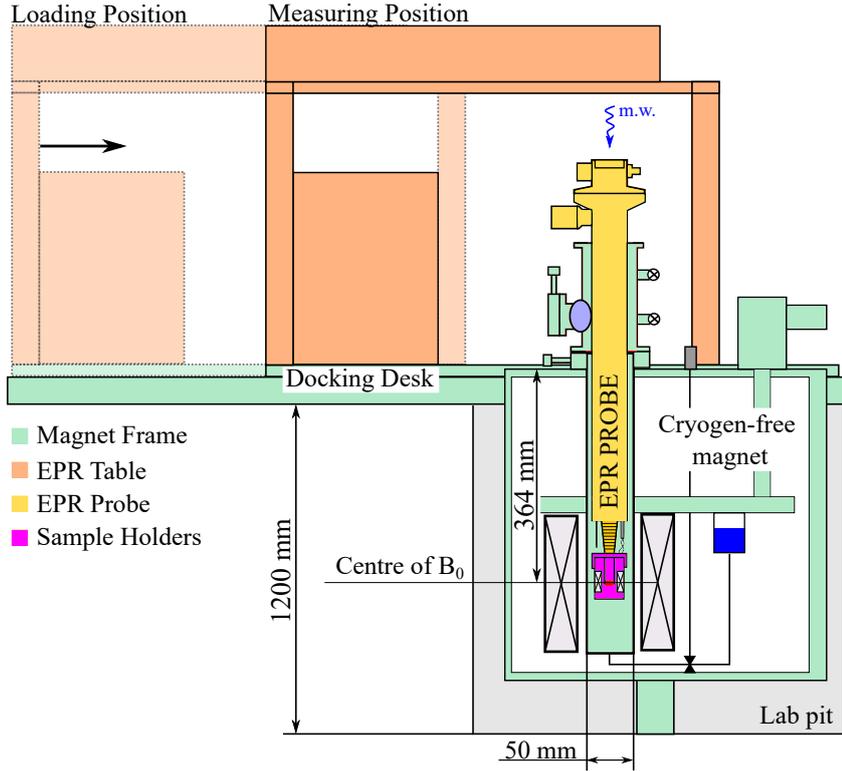
Fig. 4.2: Schematic drawing of the THz-FRaSCAN-EPR spectrometer. The spectrometer consists of a removable EPR table, magnet frame, EPR probe, and sample holder. After the probe is inserted into the magnet, the sample is located in the centre of the magnetic field. Then, the EPR table moves above the EPR probe to the Measuring Position, where the m.w. from the EPR table is coupled to the EPR probe, and the experiment can be performed.

The spectrometer has four main parts: Magnet Frame, EPR Table, EPR probe, and seven different sample holders shown in Fig. 4.2. All parts are standalone. The superconducting cryogen-free magnet is partially in the lab pit. Therefore, the loading port for the EPR probe is at a reasonable height, and the stray field of the magnet in the lab is low (230 G with magnet at 15 T in a circunference of 1 m around the magnet). That means the magnetic field does not penetrate the space as much as it would be if the magnet would sit directly on the lab floor. Moreover, the pit gives space for Variable Temperature Insert (VTI) pump, and electronics, which would in another case, consume working space in our lab. The only equipments of magnet that is not placed in the labare magnet compressors for the closed helium cryogenic system. They are installed in the cellar one floor below our lab to avoid their working noise in the laboratory.

The EPR table can be replaced with another movable setup allowing our magnet
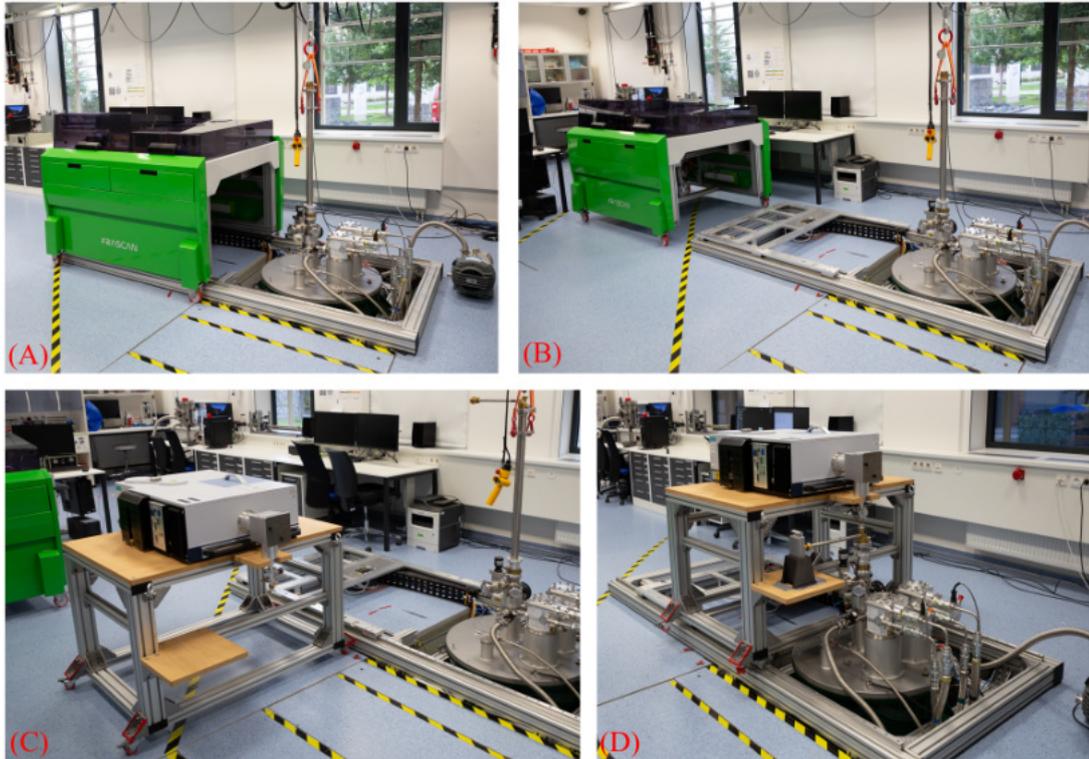
Fig. 4.3: Series of pictures showing table replacement. A) EPR Table is docked onto magnet frame docking desk in the loading position. B) The EPR table is lifted on the retractable wheels and moved away from the magnet frame. C) The FIR table is moved next to the magnet frame and prepared to put onto the magnet frame docking desk. D) FIR table was moved by automatic magnet frame docking station into the measure position and coupled with FIR probe placed in the magnet.

to be used with other techniques such as a far-infrared resonance spectrometer (FIR). Therefore, the magnet frame has a servo-driven docking desk, which delivers any table to the measurement position above the magnet and contains all necessary connections. The replacement was performed between the EPR table and FIR table, designed by Jana Dubnická Midlíková, a member of MOTES group (see Fig. 4.3). The whole substitution procedure takes five minutes and provides a huge advantage for multi-user and multi-equipment experiments.

Methodology: All 3D models and drawings were done in Creo parametric (PTC Inc., USA). Some of the 3D models (holders of cables, shafts, holders for Faradaz Rotator, etc.) were 3D printed on 3D printer Delta M (TriLAB Group s.r.o., CZ) to reduce the final cost and speed the spectrometer development. All programs were programmed in LabVIEW (National Instruments, USA).

The QO analysis was done with the Vector Network Analyser and TK power meter. VNA measurements were done with a set of 260-400 GHz and 325-500 GHz frequency extenders (RSZC400 and RSZC500, RohdeSchwarz, Germany). The measurements with the TK power meter were done within the whole range with FRaS-CAN spectrometer m.w. sources. The modulation of power to enhance the signal of the TK power meter was done with power modulation of m.w. sources.

4.1 Magnet Frame

The magnet frame (see Fig. 4.4) is mostly assembled from Aluminum profiles (Bosch Rexroth s.r.o., Germany). The main advantages of aluminum profiles over the welded assembly are the modularity and simple construction of the frame. That was demonstrated more than once during the troubleshooting of the spectrometer, where the position and dimensions had to be changed to fit the spectrometer requirements. The other parts of the magnet frame are the superconducting cryogen-free magnet, airlock, docking desk with the servo-driven system (x-movement system).
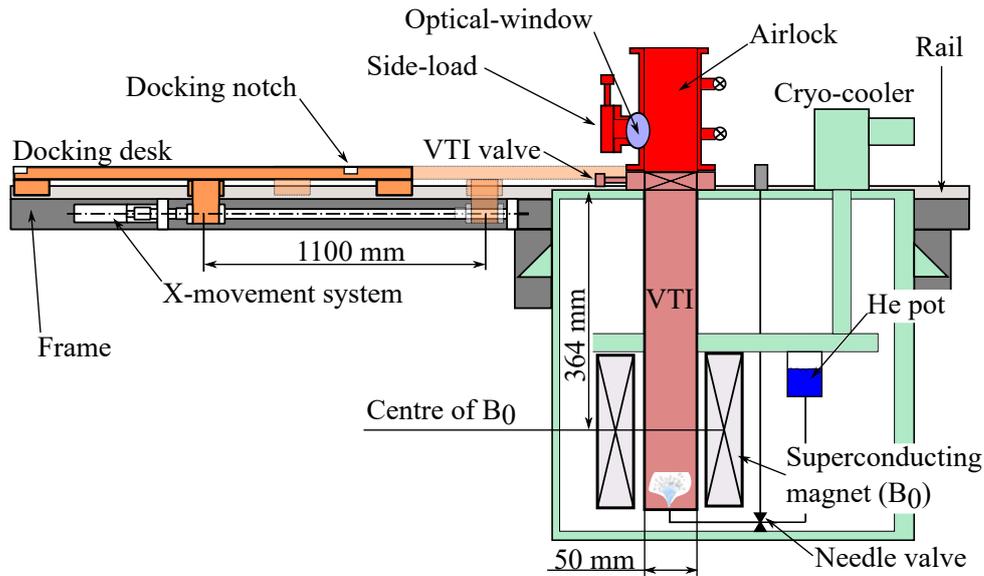
Fig. 4.4: The illustrative scheme of magnet frame.

The superconducting magnet (Cryogenics Ltd., UK) is attached to the frame in a way that the airlock inserting bore is in the user-friendly height of 512 mm. It is a cryogen-free magnet, i.e., using a closed circuit of helium to cool down coil to superconductive temperature. The helium gas is compressed and sent into two cryo-coolers, where it expands and goes back to compressors. The helium gas expansion cools down the magnet coils to temperatures bellow 4 K. The most significant

advantage of such a system is that it does not need refilling liquid helium and nitrogen every few hours/days as a wet magnet (magnet cooled down by liquid helium, which has to be refilled after certain time, typically several days). Moreover, with the rising price of helium, cryogenic-free magnets are a more sought-after option from an economic point of view. However, it has some disadvantages, such as the limited cooling power that limits the possible sweeping rates of the magnetic field (mT/s) and maintenance of the cooling system, during which the system has to be warm up for several days.
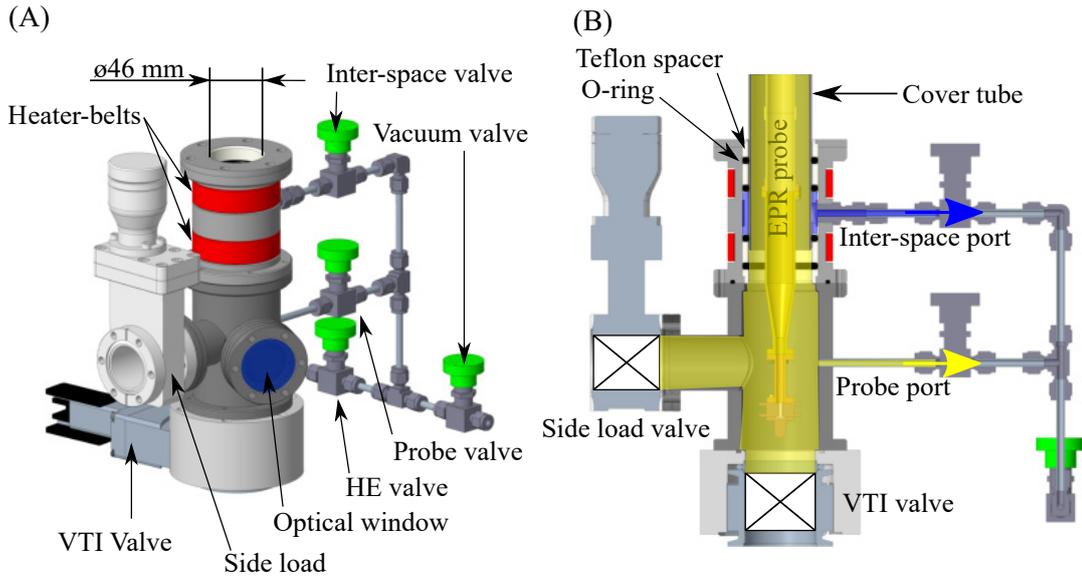
Fig. 4.5: A) The 3D model of Airlock. B) Cut view of the airlock with loaded EPR probe.

The magnet cryostat, VTI, allows to control the temperature in the sample space from 1.8 K to 400 K by circulating He gas in a separate circuit. The circuit is thermally connected to cryo-coolers which cool down the gas and condense it in the He pot. The temperature is controlled by adjusting the flow through a needle valve and the heater located at the bottom of the VTI chamber. The VTI enables performing accurate temperature-dependent experiments (more information and scheme of VTI is shown in Appendix C). However, it also requires special handling with loading a sample, namely when inserting and removing the probe, because the circuit is prone to blockage caused by air contamination. Therefore part of the magnet frame is a home-made loading airlock mechanism mounted on the top of the magnet (see Fig.4.6 and Fig. 4.5) Moreover, the airlock has a port for side-loading samples that can be transferred from a glove box or Ultra High vacuum (UHV) system with an optical window to check the sample in sample holders visually.
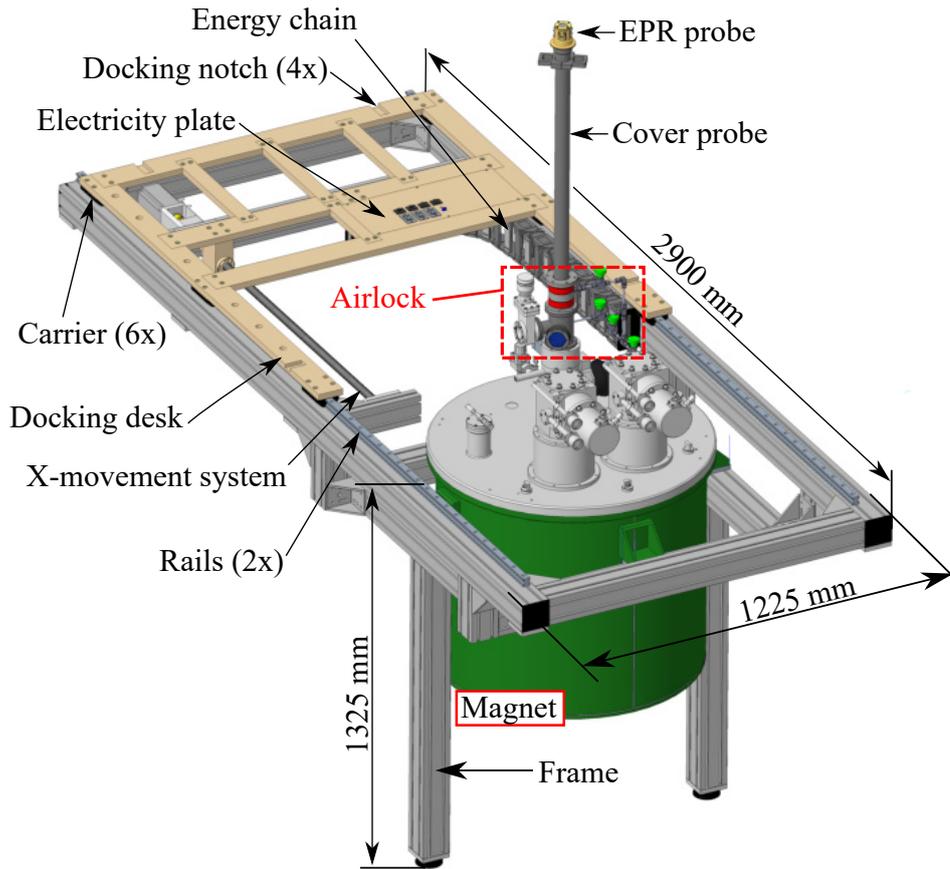
Fig. 4.6: 3D model of the magnet frame. The docking desk is in the loading/unloading position, while the EPR probe is inserted inside the airlock.

To insert the EPR probe into the VTI, the probe has to be loaded into the airlock first with the VTI valve closed. When the probe is loaded into the airlock (see Fig. 4.5), the operator opens the inter-space, probe, and vacuum valves connected to the scroll pump. Air from the airlock and the EPR probe (waveguide, sample holder, etc.) is pumped out by the airlock's probe port. The inter-space port serves for pumping the space between the o-rings. He-valve is used to flash the probe and airlock with He gas to reach a better vacuum level. When the vacuum inside the EPR probe reaches a sufficient level, the operator closes the probe port. Then, the VTI valve is opened, the EPR probe is slowly inserted into the magnet. Since the inter-space port remains open, any air that would pass the first two o-rings will be pumped out, and the He gas inside VTI will not be contaminated, a procedure known as differential pumping. The process of unloading the EPR probe is following: The Probe is pulled out from the VTI to the height above the VTI valve. Then the valve is closed, and the airlock is filled by air. If the EPR probe is cold, it remains in the He atmosphere until it reaches room temperature to avoid moisture condensation in

the waveguide. Later, the airlock is filled with air, and the EPR probe is taken out.

As mentioned, one of the innovative aspects of our spectrometer concept is the possibility of sharing the magnet with other spectroscopic methods. That means the frame with the magnet is standalone and is equipped with a servo-driven (x-movement system) movable docking desk with all accessories for plugging in other tables (see Fig. 4.6). The docking desk has a moving range of 1100 mm (movement systems is discussed in the next section). Four docking notches are cut into the docking desk to ensure table position during the docking. Therefore, there is no need to repeat table position calibration after re-docking. All communication and electrical hubs are in the distributor plate together with the nitrogen port (USB, Ethernet, nitrogen access, 240 V sock, 24 V, and ground connectors). The cables from the distribution plate are led to the lab by the energy chain (Igus inc., DE) to the lab pit from which they are distributed. The controlling lab computer is placed at the table next to the frame.

4.1.1 Vacuum transfer system

Part of the EPR table design was the system for transferring the air-sensitive sample from the UHV chambers (see Fig. 4.7). The main idea is to transfer the sample prepared via a custom-made vacuum case, which prevents exposure of the sample to the atmosphere and enables the study of air-sensitive systems by EPR and other methods without air contamination. The main reason for the custom-made vacuum case was more flexible and broad compatibility not only with our EPR Table and the cost. Our final solution costs €17 243, including the pumping system. The cheapest commercial solution for the UHV case company Henniker-scientific costs €24 780. But, it is without the angle adjustment component and vacuum pumping by only an ion pump.
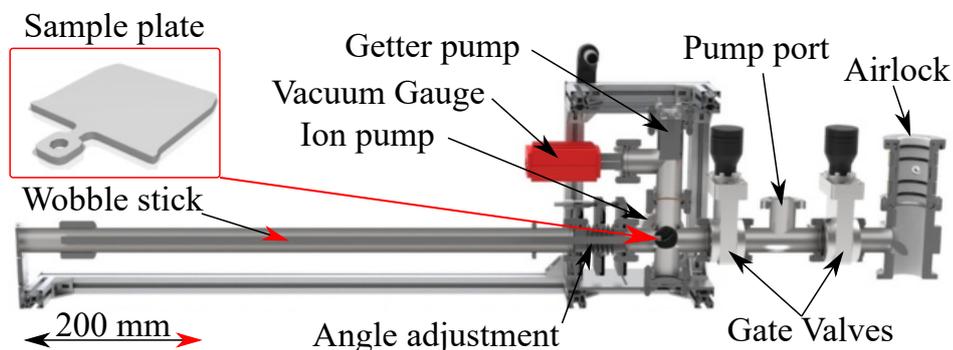
Fig. 4.7: Design for the EPR transmission system connected to airlock system (without supporting frame) for loading samples into EPR magnet.
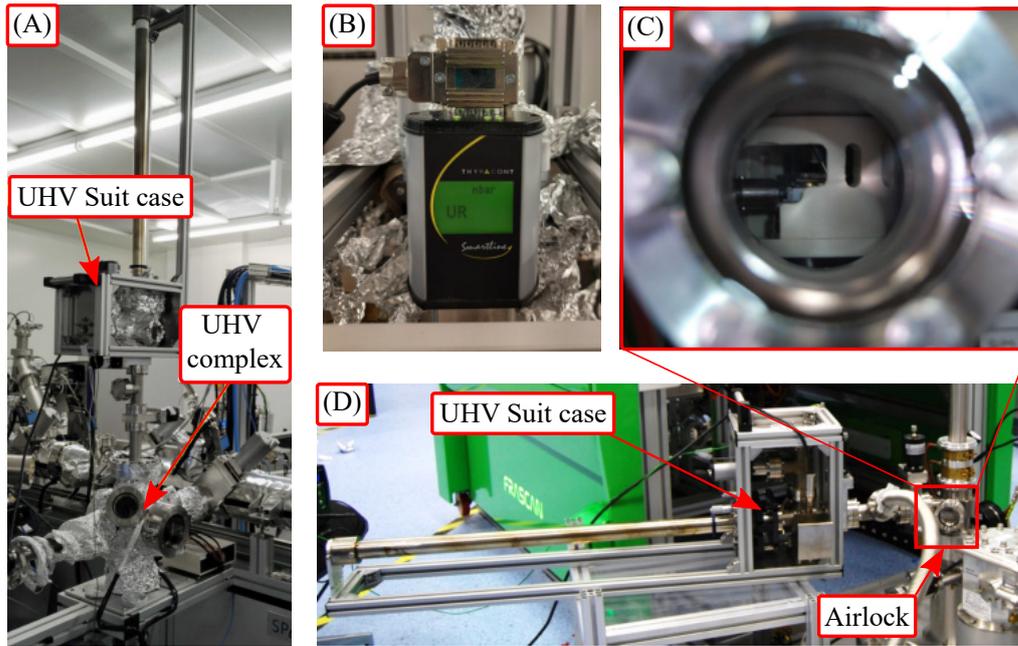
Fig. 4.8: Photo of the connected UHV case to the airlock. The inset shows the view through the optical window of the loading procedure of omicron plate into Vacuum Sample Holder, discussed in Chapter 5.

Sample transfer from the UHV chamber to the EPR spectrometer without exposing its surface to the ambient conditions works as follows (see model at the Fig. 4.7 and photography at Fig. 4.8 A): The sample, prepared in UHV is moved under similar UHV conditions into the airlock, then our homemade vacuum case is attached to the side-load port (CF-60) of the airlock through a permanently mounted separating valve. Once evacuated (and baked out for better pressure), the sample is transferred by a wobble-stick (M-RM40-500-30, LewVac, UK) to the vacuum case, the valves closed, the suitcase is disconnected and moved to the EPR laboratory. To ensure UHV conditions during the transfer, a combined ion (5SCV2VSCNN, Gammavacuum, USA) and getter pump (NEGQ2E2SSN, Gammavacuum, USA) powered by batteries is used. More information on how these vacuum pumps work can be found in [126]. In the EPR laboratory, the transfer suitcase is connected to the EPR spectrometer through a homemade airlock loading system and evacuated (see Fig.4.8 D). Then, the sample is inserted into the Vacuum Sample Holder (see Fig. 4.8 C), which is discussed later, mounted at the end of the EPR probe, and prepared in the airlock under the vacuum. When the probe with a sample is ready for inserting into the magnet cryostat, the vacuum case is disconnected. Inside the cryostat (VTI), the sample is at clean He atmosphere (10 mbar).

The test transfer between the magnet frame and UHV complex was tested with a
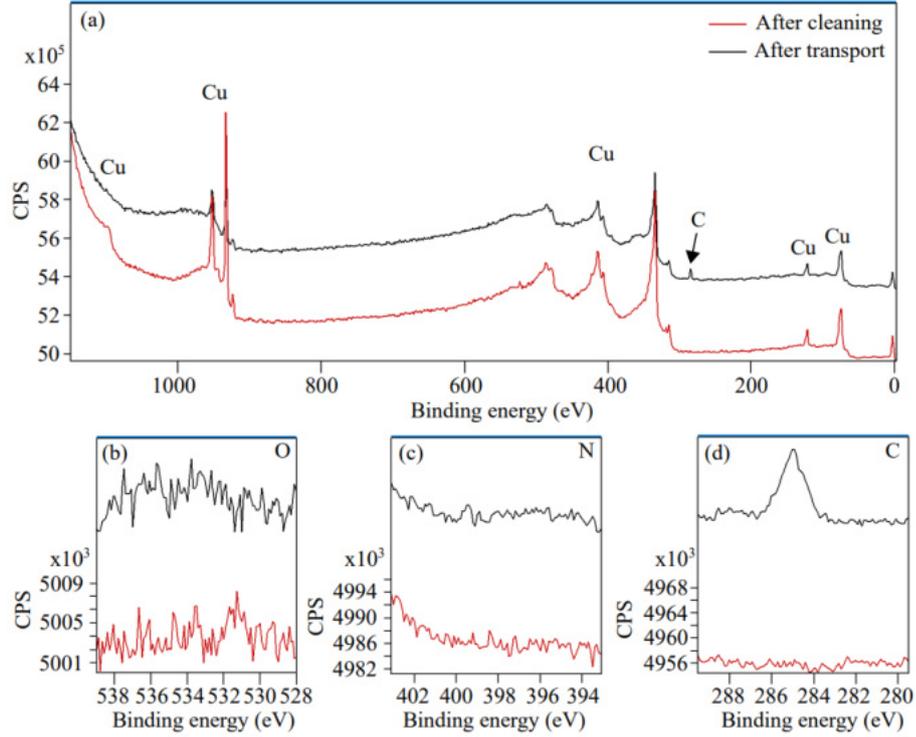
Fig. 4.9: XPS spectra of the Cu test sample before and after the transport to the HF-EPR spectrometer. (a) Wide field spectrum of the Cu test sample. (b) Detail region, where the potential peak of oxygen should be observed. (c) Detail region, where the peak of nitrogen element should be observed. In (b) and (c), there can be seen just noise. (d) Detailed region where the peak of carbon element is observed. Taken from [5].

copper crystal mounted in an omicron plate, and without the getter pump (pump aws malfunction). The vacuum pressure, in that case, was during the transfer $5.7 \cdot 10^{-9}$ mbar with a drop to 10^{-6} during the loading of the sample into the airlock. The transfer test monitored the level of copper sample contamination during the transport. The copper sample was chosen due to its reactive surface. The contamination levels of nitrogen, oxygen, and carbon elements, the main polluting elements, were measured before and after the transfer. XPS spectra were acquired and compared with the XPS spectra before transportation (see Fig. 4.8), resulting in a minor carbon contamination.

With a fully working vacuum system (ion pump and getter pump) and after the baking procedure (heating up the chamber to 150˙C), the pressure in the chamber extended the gauge range. Therefore it was assumed that a pressure smaller than 10^{-10} mbar) was achieved (see Fig. 4.8 B).

4.2 EPR Table

The illustrative scheme of the EPR table is shown in Fig. 4.10, the main parts are the aluminum frame (similar to magnet frame), EPR bridge for m.w. manipulation (QO), m.w. sources, and m.w. detectors), and electronics for EPR experiments. The EPR bridge is covered by two removable plexiglass covers to protect QO components from mechanical damage and dust (Fig. 4.11). Some of the QO components like the Faraday rotator and corrugated waveguides/horns of sources and detectors operate only in a certain frequency range and need to be replaced for each frequency band. Therefore, the plexiglass cover is split into two halves to be easily taken down for QO components replacement.
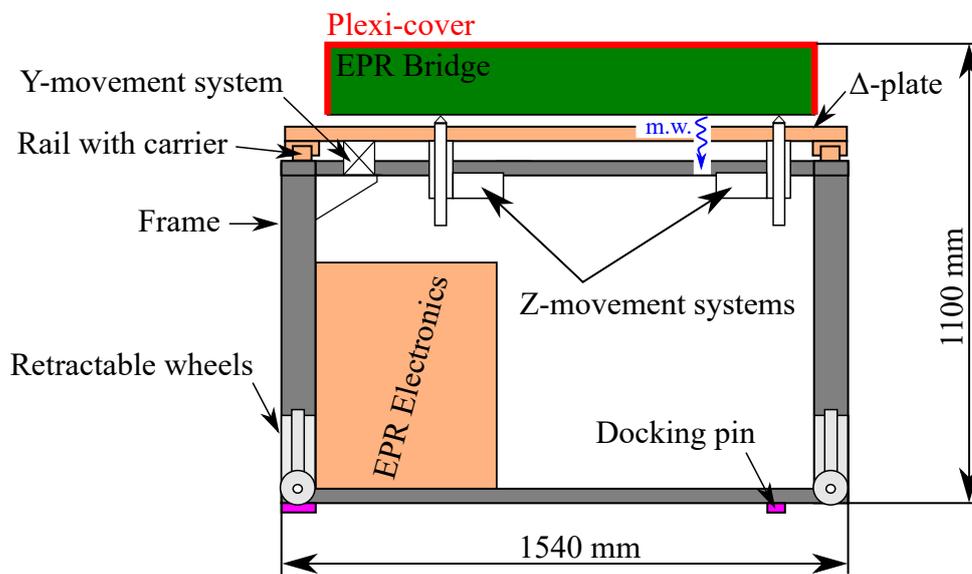
Fig. 4.10: The illustrative scheme of the EPR table. The table is standalone, therefore all electronics, movement systems and m.w. components are permanently part of it. All m.w. components are in the EPR bridge (m.w. sources, m.w. detectors, QO), which sit on the z-movement system. Those are mounted to the Δ-plate, which is screwed to carriers and the y-movement system.

To easily undock or dock the EPR table from the magnet frame, the table has four retractable legs and four docking pins. When the legs are extended, the table is lifted off and undocked from the magnet frame. The docking pins serve for precise and reproducible docking of the table into its exact position.

The coupling of the m.w. between the EPR probe and EPR bridge is realized through an automatized coupling mechanism. It consists of four independent servo-driven movement systems (plus the x-movement system mounted in the magnet frame), one for y-direction, and three for z-direction (height and angle adjustment).

The QO sits on pins of three z-movement systems mounted to the delta plate, which is screwed to the linear rails with the y-movement system connected.
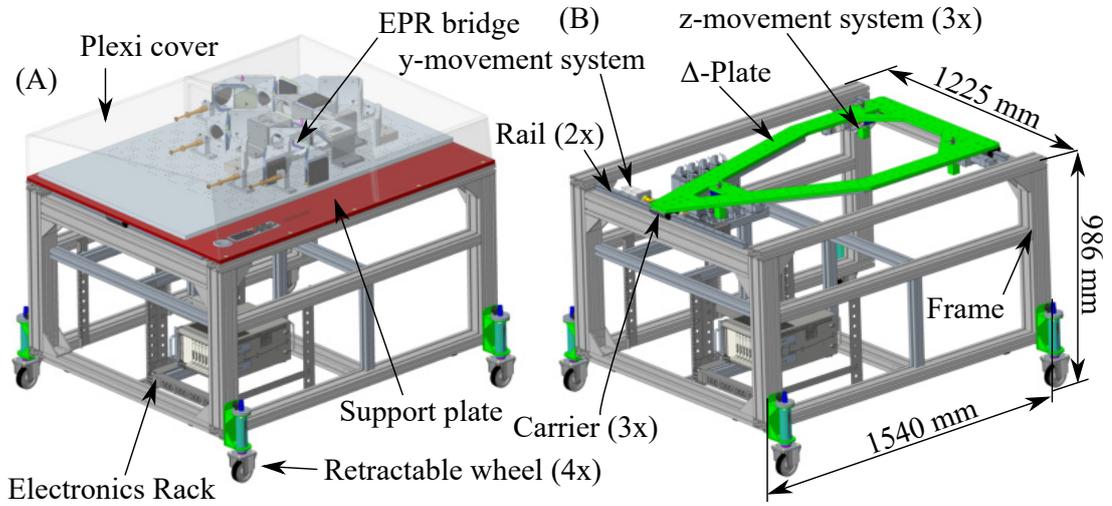
Fig. 4.11: The 3D model of EPR table. A) The model displays the EPR bridge covered by plexiglass covers. B) The model without EPR bridge, plexiglass covers and support plate.

All controllers such as lock-in, digitizer, servo-electronics, source meter, and 9V/24V power sources are mounted in the electronic rack. The support desk, screwed to the top of the aluminum frame, contains a variety of connectors (USB, Ethernet, 240V, nitrogen, and ground) and a basic tool set (see Appendix D.1).

4.2.1 EPR Bridge

The EPR bridge contains m.w. source, m.w. detector and QO solution with reasonably low m.w. attenuation. Most of the parts of the spectrometer are frequency-independent parts with low losses. However, some components are specific for a "narrow"-frequency range (100 GHz) and have to be replaced according to the desired operating frequency. Therefore, the nominal operating frequency range of the spectrometer - 82 to 1100 GHz - is divided into seven bands with different frequency ranges and powers (see Table 4.2). Mirrors, wire grids, and absorbers can be in our frequency range taken as frequency-independent components [122]. Faraday rotators, corrugated waveguides (EPR probes and antenna horns) connected to mixers and multipliers are frequency dependent. A unique detector and multiplier combination is also specific for each frequency range.

Tab. 4.2: The basic information about the separate frequency bands.

f(GHz)	82-125	110-170	170-280	250-350	350-500	500-750	750-1100
λ (mm)	3.6-2.4	2.7-1.8	1.8-1.1	1.2-0.9	0.9-0.6	0.9-0.4	0.4-0.3
Horns[1]	WR9.0	WR6.5	WR4.3	WR2.8	WR2.2	WR1.5	WR1.0
P(dBm)	$+20$	$+17$	$+13$	0	-3	-5	-25
P(mW)	100	50	20	1	0.5	0.32	0.003
Mult.[2]	9	12	$9+x_2$	$9+x_3$	$12+x_3$	$9+x_{2+3}$	$12+x_{2+3}$

In our setup, desired m.w. frequency is generated by a combination of multipliers fed by m.w. from AMC (Amplifier / Multiplier Chains) and synthesizers. The output frequency of synthesizers is still the same, 9.11 to 13.9 GHz. Therefore, more multiplication has to be used to achieve a higher frequency, which causes that source m.w. output power is smaller at higher bands. At highest frequency band, sources output power is 0.003 mW[3]. All m.w. sources, detectors, AMC and multipliers were bought from VDI (Virginia Diodes, Inc., USA).

A closer look at the Fig. 4.12 reveals two source lines, local oscillator (LO) and radio-frequency (RF), and three detectors, cross-polar mixer (XP), co-polar mixer (Co), and final mixer. The LO does not propagate to the sample. Instead, the polarizer splits the LO beam into two separate lines, propagating directly to the mixers. The RF m.w. propagates into the EPR probe (corrugated waveguide) and is reflected from the mirror under the sample. Then, the reflected RF beam at the output of the EPR probe can be split into two m.w. beams of the same frequency but different polarization. The m.w. beam whose polarization was changed by the sample is deflected by the polarizer above the probe and continues to the XP mixer. The unchanged m.w. beam goes through the polarizer and continues to the Co mixer. After the first stage mixing, the signal at the intermediate frequency (1800 MHz in our case) goes to the final mixer, where the signal is converted to the DC (m.w. from Co-mixer works as LO, here). In the first stage mixing. DC signal is then going into Lock-in *MFLI 500 kHz/5 MHz Lock-in Amplifier* (Zurich Instruments AG, CH), which is also feeding AC current into modulation coil. That helps to reduce the $1/f$–noise from the system's noise figure.

---

[1]Horns line specify the output size of waveguide for corresponding horn antennas.

[2]The multipliers are described according to the used AMC (9 or 12 multiplication) and the specific doubler x_2 or tripler x_3.

[3]This power is smaller when it reaches the sample as it is attenuated during the propagation of m.w. through the QO system.

The spectrometer works in induction mode. The polarizer above the EPR probe reflects into the detector only m.w. beam containing information about the sample. The induction mode increases the sensitivity of the HF-EPR spectrometer by several orders. The principle is to detect only part of the signal which contains information about the sample. After passing of sample in resonance by linearly polarized beam, the polarization will slightly change. The polarizer above the probe will deflect part of the m.w. beam with changed polarization into the XP line. Unchanged m.w. passes the polarizer and continue into the Co detector.
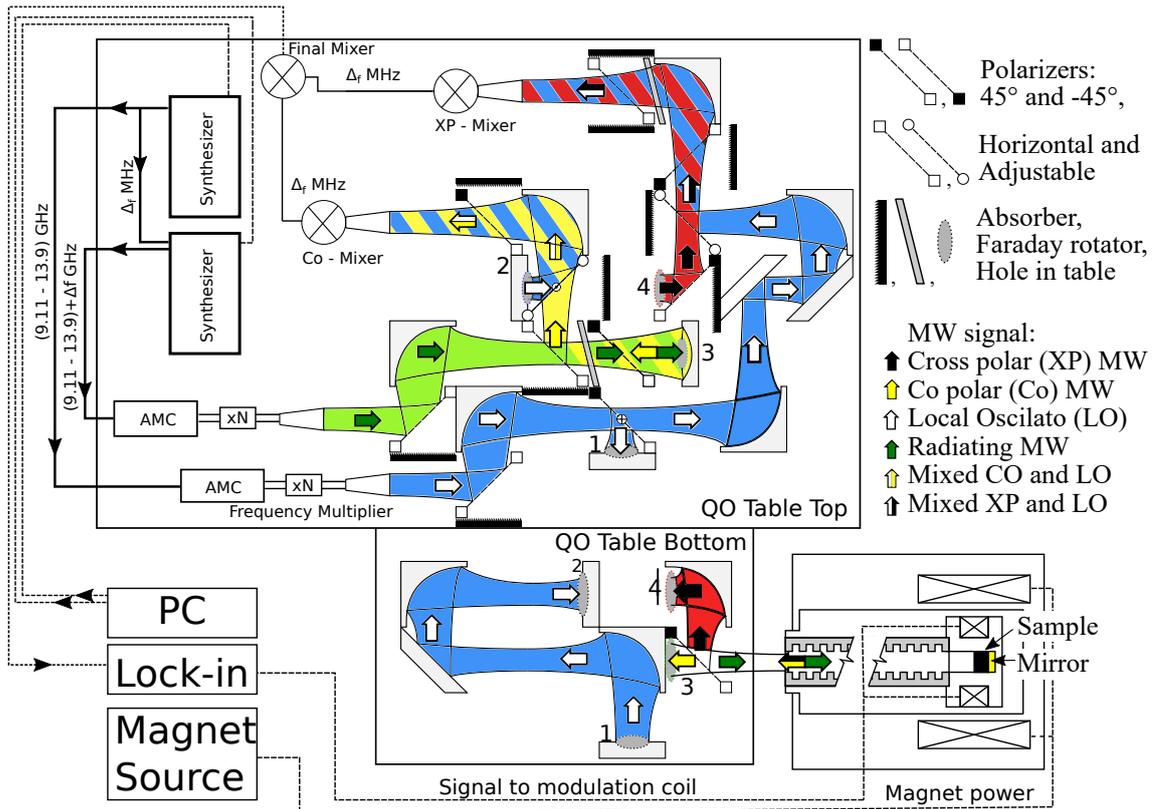
Fig. 4.12: Schematic drawing of QO solution of FRaSCAN. The legend describes the main symbols. The m.w. beam is generated in phase-coupled synthesizers multiplied by AMC and a set of multipliers (xN), depending on the required final frequency. The numbers in beam paths mark the holes in the QO where the beam propagates from table top to table bottom and vice versa.

4.2.2 Characterization of main parts of EPR bridge

The measurements were done with the help of a 26.5 GHz analyzer (RSZNA26, RohdeSchwarz, Germany) or by TK power meter (Thomas Keating Ltd, UK). The method is always specified with the results. The QO table with all components was

tested for m.w. losses and standing waves. From the measurements, we come to the following results:

- **Faraday Rotator**

The average power losses were determined for each frequency range with each isolator in the LO-XP circuit and are shown in Table 4.3. These values were compared to the reference power in each frequency range, which was the LO-XP circuit without the final wire grid and no Faraday rotators. The difference between the measured power and the reference power is the insertion loss of the Faraday rotator. It is anticipated that the insertion loss will increase with increasing frequency, which is consistent with the measured losses. There are two Faraday rotators marked with serial numbers for each frequency range; however, due to high losses and low efficiency, Faraday rotators aren't used for frequencies above 500 GHz.

Tab. 4.3: Faraday rotator losses determined over the full bandwidths. Measured by TK power meter.

Serial number	Frequency (GHz)	Average insertion Loss (dB)
BT11	$80 - 125$	0.21
BV11		0.53
CE11	$170 - 250$	1.33
BC11		1.22
BQ11	$250 - 375$	2.27
BU11		1.61
CD11	$325 - 500$	3.65
BS11		3.48

- **General loses of QO table**

The system optics were tested to obtain the overall quasi-optics losses. The performance of the RF and LO lines was determined by a TK power meter at the detector position. During testing the AMC-multiplier-horn combinations were used as specified in Table 4.2. The reference measurement was done using separate QO assemblies consisting of AMC-Multipler-horn, two focusing mirrors, and TK power meter. The modulation to the source was not at full amplitude, which results in slightly underestimated calibration. Additionally, the polarization at the power meter was not horizontal meaning the power detected is slightly underestimated as the beam was not at Brewster's angle. Therefore, some values are observed to be greater than that anticipated. Measurements were not performed at 940 GHz as the signal power was below the detection limit of the power meter. The roof mirror placed at EPR probe input serves as director of m.w. to chosen line (XP or CO).

Tab. 4.4: The overall insertion losses of the QO system with horns antennas and Faraday rotators. At a frequency above 500 GHZ, no Faraday rotators were used. Measured by TK power meter.

Freq.(GHz)	RF→XP	RF→CO	LO→ XP	LO→CO
80-125	0.52 dB	1.26 dB	-1.1 dB	-0.82 dB
170-250	1.78 dB	0.50 dB	1.41 dB	0.41 dB
240-380	1.40 dB	0.63 dB	1.44 dB	2.57 dB
320-500	1.42 dB	2.54 dB	0.13 dB	0.57 dB
500-750	4.98 dB	2.84 dB	2.52 dB	1.24 dB

- **XP isolation**

A well-performing induction mode system must have sufficient isolation between the XP and the CO line. The leakage of CO into XP can cause the rise of background signal and, therefore, attenuation of the EPR signal. In our case, isolation of the XP line from the CO line is done by wire grid polarizers in the XP line. Therefore, the isolation of the XP line defines how well the spectrometer works. From Vector Network Analyzer (VNA), we know that isolation is 20 dB (see Fig. 4.13), as it should be from the wire grid specification. To increase the isolation, a moveable roof mirror has to be installed under the sample. Such systems can get up to 80 dB XP isolation.
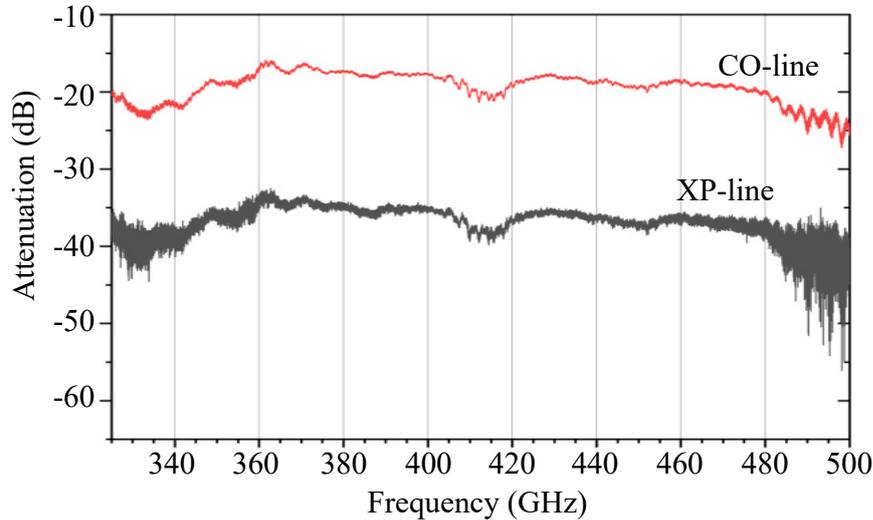
Fig. 4.13: Signal in Co and XP line with a VNA extender as RF source. The extenders were not calibrated, Therefore, there is a drop in power. Valuable information is the difference between the CO and XP lines, 20 dB.

The measurement was done with VNA and with the roof mirror at the probe

m.w. window. By rotation, the roof mirror was set up to a position enabling maximal Co signal. One of the extenders of VNA was used as an RF source. The second extender measures data at the position of XP and Co mixer. The extenders were not calibrated before these measurements therefore, there is this attenuation in the Co-line.

- **Standing wave reduction**

To reduce the standing waves in detection, m.w. in Lo and RF paths go through the same number of QO components. The last components in the XP line - Faraday rotator and polarizer - work as a standing wave filter. The demonstration of its functionality is shown in Fig. 4.14. When the component is removed, the standing wave pattern of higher intensity signal appears. The higher intensity is mainly caused due to a mismatch of the detector by 45 degrees. When Faraday Rotator was removed, the detector remained at the same orientation. The standing wave pattern has a frequency step of 0.063 GHz. That is equal to a wavelength of 4760 mm. If we divide this wavelength by two, it equals 2380 mm, the distance between the XP detector and RF source.
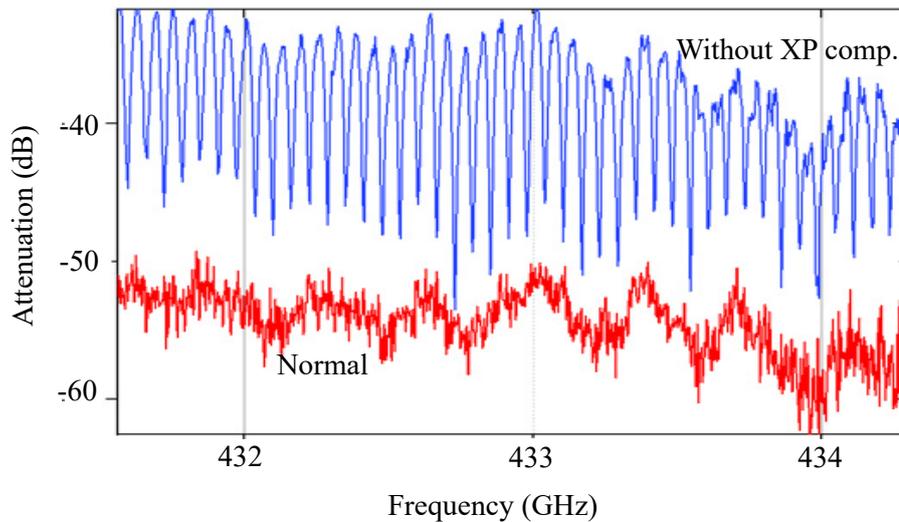
Fig. 4.14: Red) The measurement with the last Faraday Rotator and wire grid polarizer. Blue) The measurement without first the Faraday Rotator and wire grid polarizer in front of XP mixer.

4.2.3   Automatized coupling adjustment

The coupling of the m.w. beam between the EPR probe and QO is crucial (see Fig. 4.15). A few miliradians offset can cause significant signal damping, especially at high frequencies (see section 3.2.2.). In most HF-EPR systems [51] [33] [102], the coupling is realized by adjusting screws on which the EPR bridge is placed. This way of coupling calibration can take from a few hours up to several days. Additionally, in those HF-EPR spectrometers, the EPR bridge has to be moved away from the coupling position during each loading/unloading of the sample. Hence the coupling calibration process has to be repeated after several months.

RF   Copolar
LO   Cross Polar
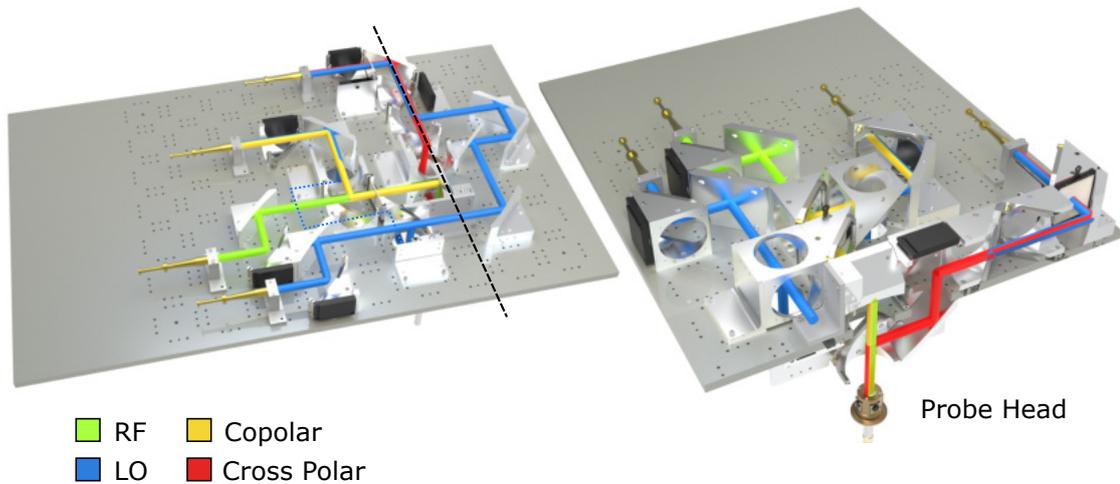
Fig. 4.15: The render of coupled QO with the EPR probe for the FRaSCAN EPR spectrometer. The QO has two sources, the LO and RF. The polarizer split the LO into two separate lines, going directly into the mixers. The m.w. from the RF source goes into the probe, reflected from the mirror under the sample. The m.w. with the signal information is deflected into the XP line. The unchanged m.w. pass the polarizer and continue as Co signal into Co mixer.

Therefore, the FRaSCAN spectrometer was designed with a highly-precise servo-driven movement system. It is realized by five independent assemblies, where each is powered by one servo driver of different size, power, and range (see Table 4.5).

The x-movement system driver is part of the magnet frame. It has the highest range of 1100 mm as it is used, except for precise position adjustment, to move docking desk (with the table docked) from the magnet when the probe is loaded into the magnet (see Fig. 4.16). The y-movement system is mounted on the Table frame and moves the Δ-plate perpendicularly to the x-movement system. The last three z-movement system are mounted on Δ-plate. They employ the gear that translates the rotary motion of the servo into the linear motion of the pin. QO

Tab. 4.5: Basic information about each servo-driven movement system. The angle value in the z-direction is for servo z_1.

Axis	X	Y	Z
Range (mm)	0 - 1100	0 - 100	0 - 50
Step (mm)	0.1	0.1	0.05 (minimal 0.002 deg)
Max load (kg)	550	350	125 x 3

sits without a permanent connection on those pins. Therefore, the precise angle adjustment is realized by moving one of the three z-movement systems. If all three z-movement systems are moving at once, the height is adjusted.
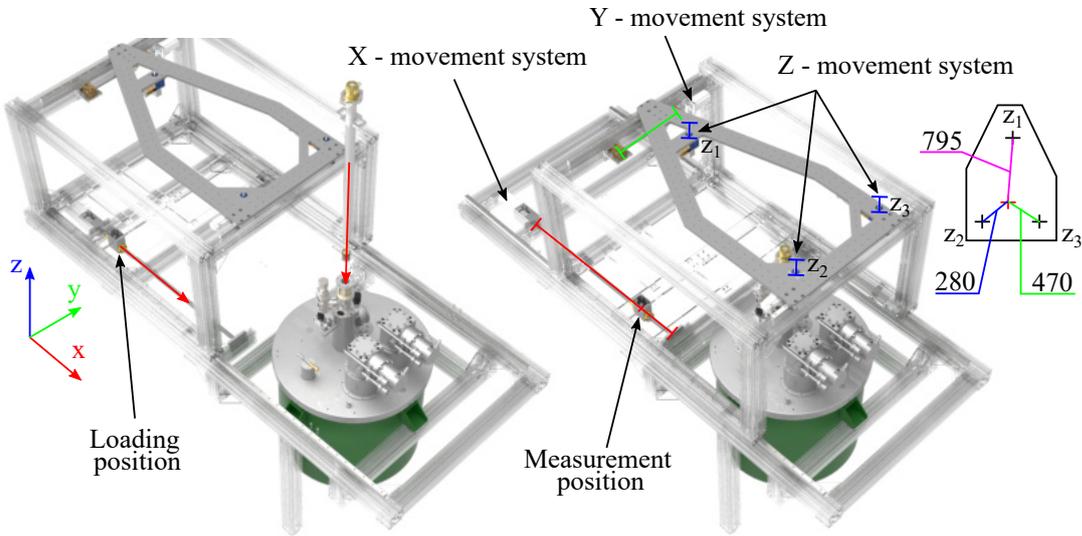
Fig. 4.16: Render of Coupling EPR Table with EPR probe via the servo-driven movement system. Left) the position of the table for loading the EPR probe into the magnet. Right) The position of the table at the measurements position. The x-movement and y-movement systems employ trapeze rods with driven and backslash nuts. The z-movement system is composed of three independent systems using a worm gearbox with a ratio of 4/1. The inset shows distances of z-movement systems from the m.w. output of the EPR bridge.

The x and y-movement system design are based on the same principle except for the different sizes and ranges (see Fig. 4.17). The servo transfers the motion via the clutch connected with the trapezoidal rod (TR12). The rod is seated in a solid house at one end and a free house with higher tolerance at the other end to avoid component damage due to misalignment. The rotary movement into linear

movement is realized through the control block, connected with rod via nuts and with Δ-plate (or docking desk in X-movement system) via screws. Two nuts from each side are used to avoid backslash when the direction of movement is changed.
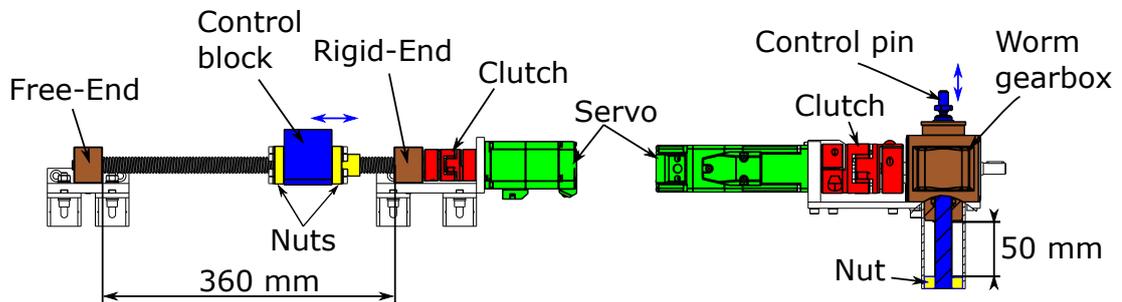
Fig. 4.17: The drawings of movement system. Left) X and y, Right) z-movement system.

The z-movement system uses a worm gearbox, which translates the rotatory movement of servo into the linear translation of the pin. The ratio of the gear is 20:1, which results in 0.002 deg of the step size on the z_3 servo drive. There is no need for a backslash nut to reduce error in change of direction due to constant pushing of screw on one side of the thread by mass of the QO table.
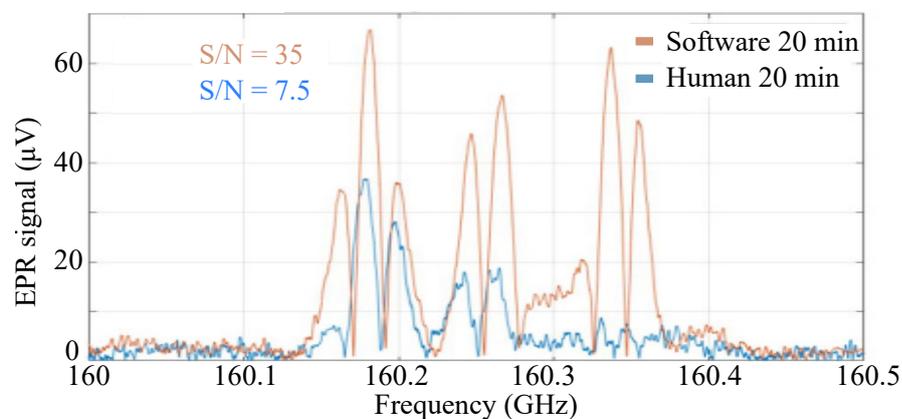
Fig. 4.18: Measured signal of 1mM TEMPOL dissolved in water before (blue) and after (orange) running the automatic adjustment program with values of S/N.

All servos are controlled manually via computer and software created in Lab-VIEW (see Appendix E.2). The coupling adjustment is fully automatic. The operator has to find the signal in the frequency domain, and then it turns on the program, which will find the best position in several interactions. The first version of the program is rather simple. The program moves one movement system by default step in

the range around the actual position. After it finds the best position, writes it to the table and moves with another movement system. This process repeats several times through all drivers. Even with this simple solution, it shows that the software can find the position much faster than the operator in roughly 20 minutes (see Fig.4.18). To compare, it took several hours to achieve the same results by adjusting the servos manually.

Cover plates   Part of the work was focused on the spectrometers' external design. Therefore, in collaboration with the professor of design from BUT, Mr. Křenek, the EPR table, and EPR Frame cover were designed (until nowadays, only EPR table cover was realized). Covers for the EPR table contain practical shelves to store EPR table-related stuff such as Faraday rotators, cables, tools, horns, and mixers. The covers are made from nonmagnetic stainless steel 316 and held in a fast lock system on the table. Therefore, if needed can be detached within a few seconds.

Fig. 4.19: The render of covers for EPR table and EPR frame. The render created by doc. Ladislav Křenek.

4.3 EPR probe

Fig. 4.3 depicts schematically the FRaSCAN EPR probe. The sample in a sample holder (SH) is at the end of a corrugated m.w. waveguide (Thomas Keating Ltd., UK), about 1 m long designed either for 430 GHz or 100 GHz made from German silver. The waveguide is placed inside a non-magnetic stainless steel cover (cover tube) and centered by sets of thermal shields along the waveguide. At the top of the probe, the m.w. corrugated waveguide is attached to the head, which contains 3 electrical connectors DBEE104A056, SFE104A086, SFE102A053 (Fischer Connectors, CHE) and one custom-built optical connector. The uniqueness of each connector prevents them from being changed unintentionally. The m.w. window in the head is replaceable. At the figure is shown a 2.213 mm-thick high density polyethylene (HDPE) film. The electrical wires (see Appendix) are shielded and guided in two stainless steel tubes to a fast loading flange (FLF), where the SHs are attached. The first tube carries wires for cus-

Fig. 4.20: Scheme of EPR probe.

tom made modulation coils, temperature sensors (T-sensor) Cernox CX 1050 HT (LakeShore Cryotronics Inc., USA), and optional heaters and field sensors, the second tube guides wires for sensitive electrical measurements. Then, the m.w. is focused with EPR table through the HDPE window into the oversized corrugated waveguide with inner diameter 18 mm and propagates there with minimal losses to the inlet m.w. port of a SH using a focusing corrugated taper from 18 mm down to 5 mm diameter. The m.w. waveguide is used to guide also the reflected m.w. from a sample back to the outside optics. Furthermore, the cover tube is equipped with a port for a piezo step-motor (PiezoMotor Uppsala AB, SE) which is used to rotate a shaft used in CSH. The shaft goes down along the corrugated waveguide to the FLF. This motor can operate in a magnetic field and vacuum, but its functionality is uncertain at liquid helium temperatures. Therefore, the motor was placed in the upper part of the EPR probe, where the temperature is close to room temperature and hermetically sealed. Motion is then transferred to the sample platform by a perpendicular gear (1:1), approximately 90 cm long main shaft, a parallel gear (1:5), and a

short second shaft that is inside a sample holder (4.21). Described mechanical parts are all made of brass to ensure the same temperature expansion and reduce stress (tension) that may evolve from room temperature down to cryogenic temperatures. In order to reduce temperature sinking through the main shaft, it was separated by two mechanical connectors, which were made of PEEK.
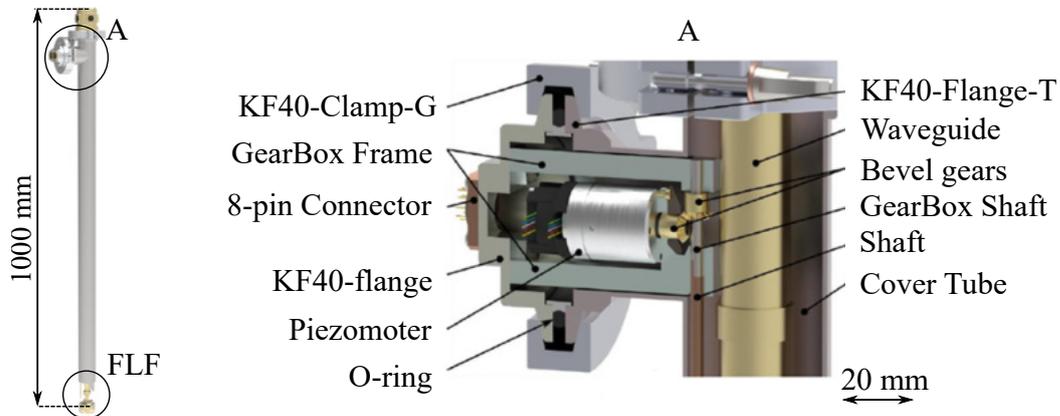
Fig. 4.21: 3D view of the EPR probe A) View of the top part of the EPR probe where the piezo step motor is located. Through shaft and set of ratio 1:1, the rotary movement is translated to FLF.

Fast Loading Flange (FLF) The design of the FLF consists of two main parts: a rotary and a base part (see Fig. 5.1). The rotary part is free to rotate in a given range on the base part and it has four grooves for the locking pins, one of which is larger to ensure a single coupling position for the SH. The base part is connected directly to the end of the corrugated waveguide. It has 24 female contacts CPINM-10 (LewVac, UK) divided into 3 connector blocks and a hole for a shaft connection. The rotary part rotates 90° around the axis of the waveguide, pushing the SH body and locking pins into the flange. Also upon rotation, all required contacts CPINM-10 are fastened to the female connectors grouped into three custom-made insulated 8-connector blocks. For good electric insulation and stability, the connector blocks are made from PEEK. The central 8-connector block contains electric contacts that are the same for all SHs: two for modulation coils, two for the T-sensor (Cernox CX 1050 HT, LakeShore Cryotronics Inc., USA), and four auxiliary ones can be used, for instance, for a magnetic field sensor (HGA-2302, LakeShore Cryotronics Inc., USA) or additional heater if needed. The other lateral 8-connectors blocks contain connectors for Rotator SH, Carousel SH and Chip SH (for more details see Appendix D.2). The rotary part of the flange is made from brass, whereas the

base part from PEEK to provides thermal insulation of the SH from the corrugated waveguide resulting in better thermal control of the sample. Experimentally, we observe that this solution decreases the cooling time of the SH from 300 K to 4 K to six hours, which is 1/3 less of the time compared to the situation where the base part is made from brass.
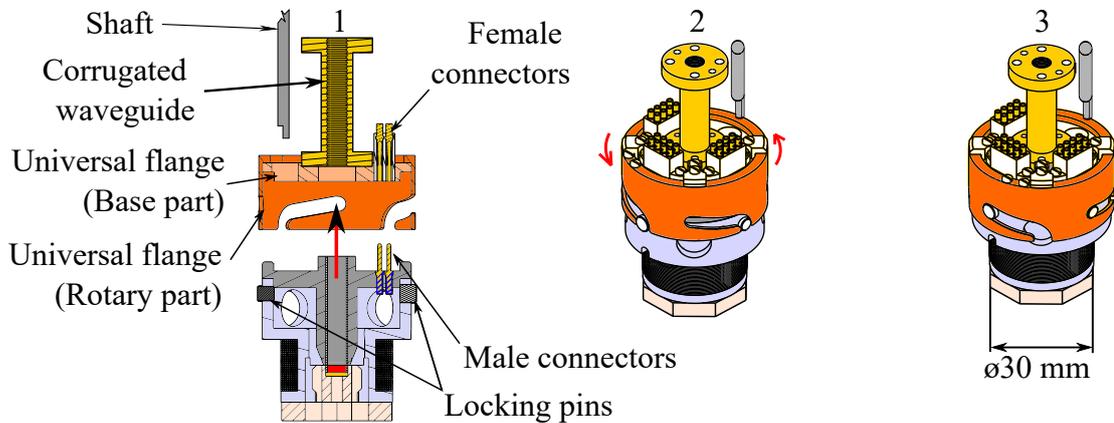
Fig. 4.22: 3D drawing of the FLM. 1) Orientation of the grooves of the universal flange (Rotary part) with the locking pins in sample holder, together with electrical connectors. 2) Rotation of the universal flange causing the full insertion of the male into the female connectors. 3) Locked position.

Our probe is shielded by a stainless tube with an open bottom end, where the sample holder is mounted. The connection feedthroughs are placed on the top of the probe. The beam enters the probe through a thin Teflon or PET (Mylar) window, which is transparent for most of the EPR signal. Additionally, the probe is equipped with copper rings each having ⌀150 mm. These rings serve as temperature isolators, thanks to it the helium flow will be concentrated around the sample and not around the whole probe, i.e., the temperature gradient in the probe will decrease.

4.3.1 EPR probe features:

Attenuation of m.w. by EPR probe: Two factors were considered during the characterization of the EPR probe. The effect of the window on the standing wave pattern and the overall damping of the signal by the EPR probe. In the test, we characterized only the 430 GHz probe. The main reason is that attenuation from the 100 GHz probe was extreme, and there is no point in using the 100 GHz probe for higher frequencies. A TK power meter and VNA measured the 430 GHz probe attenuation with the flat mirror at the end. The average attenuation measured by

the TK power meter is shown in the table 4.6. Fig. 4.23 shows the frequency dependence attenuation of 430 GHz probe from range 260 to 500 GHz. The measurements shows that the best performance of the EPR probe is at 430 GHz, where the m.w. attenuation is only 0.15 dB. It is also obvious that the probe starts to attenuate up to 3 dB around this frequency. The edges of the band 490-500 GHz and 330-350 GHz are noisier. The reason is the edge of the extender range. The average number from the TK power meter is different from the VNA measurements mainly due to the much harder setting and normalization. Therefore, VNA measurement are considered more precise.

Tab. 4.6: The double pass attenuation of the probe measured by TK power meter.

Range (GHz)	80-125	170-250	240-380	320-500
Attenuation (dB)	3.7	2	2.71	1.6
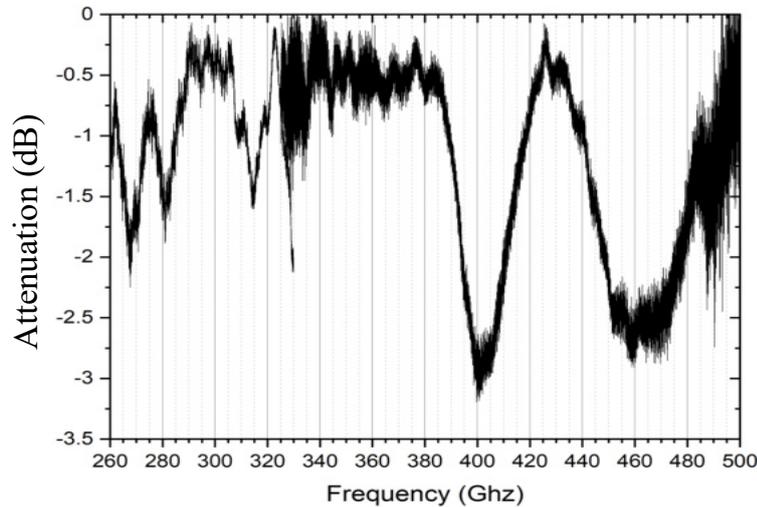
Fig. 4.23: Normalized overall double-pass attenuation of EPR probe measured by VNA without window. The reference data were taken with the mirror placed on the probe input.

Standing wave pattern: The standing wave patterns of three different windows are shown in Fig. 4.24. The flat window manufactured from HDPE film has the highest intensity of standing wave patterns. The conical window from Teflon attenuates the m.w. by 4 dB compared to the flat mirror. Moreover, it has the same standing pattern. Both windows have standing waves pattern with the same step between knots, 0.063 GHz, which equals 2080 mm. Half of this distance is equal to the length of our probe. A 30μm-thin PET (Mylar) film (typical food product packaging) can

still hold a low vacuum inside the probe (needed due to airlock system loading) and is the best performance window.
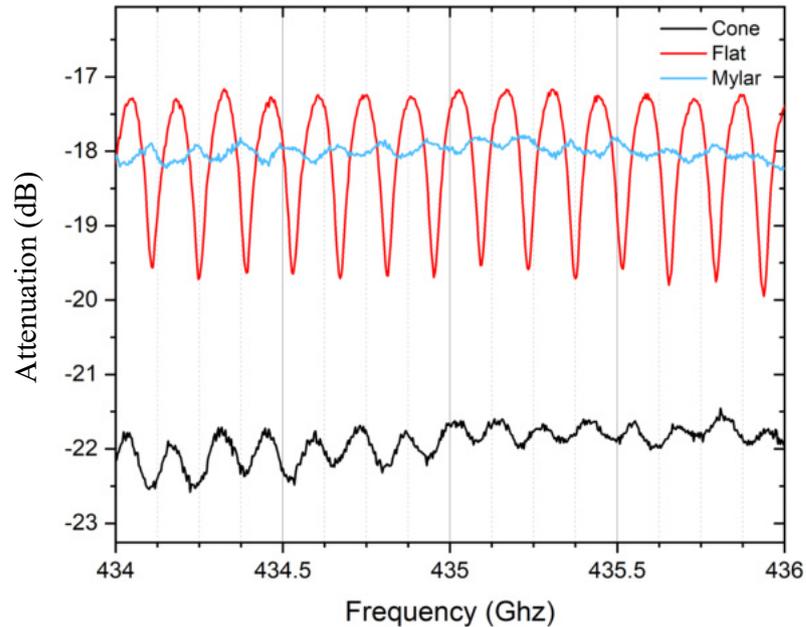
Fig. 4.24: VNA measurement of different EPR probe windows. A different standing wave intensity is observed with a similar pattern for each of the tested windows: conycal (teflon), flat (teflon) and PET (Mylar).

Therefore, the EPR probe was equipped with a PET (Mylar) film window for most of the frequency domain measurements shown in this work. Due to higher rigidity, field domain or long-term measurements were done with the flat window.

The cooling performance: Fig. 4.25 shows the temperature behavior of the EPR probe during the cooling down process. Due to prolonged cooling performance, we decided to investigate the temperature gradient of the probe during the cooling. At the time of the test, the wires were placed around the corrugated waveguide of the EPR probe, and FLF was made from brass. The needle valve was at manual control with an initial flow set to 18 mbar.

The cooling performance test was done with two slightly different setups, where five temperature sensors were used across the EPR probe and the simple sample holder. The difference between Setup 1 and 2 is the brass part of the FLF between the EPR probe and the sample holder (in setup 2 was removed), and an additional copper plate for the increasing flow of cold He through the sample in Setup 2. Therefore, Sensor C was installed on the FLF in setup 1, and in setup 2, it locates at the top of the sample holder because FLF was removed for test. The distribution
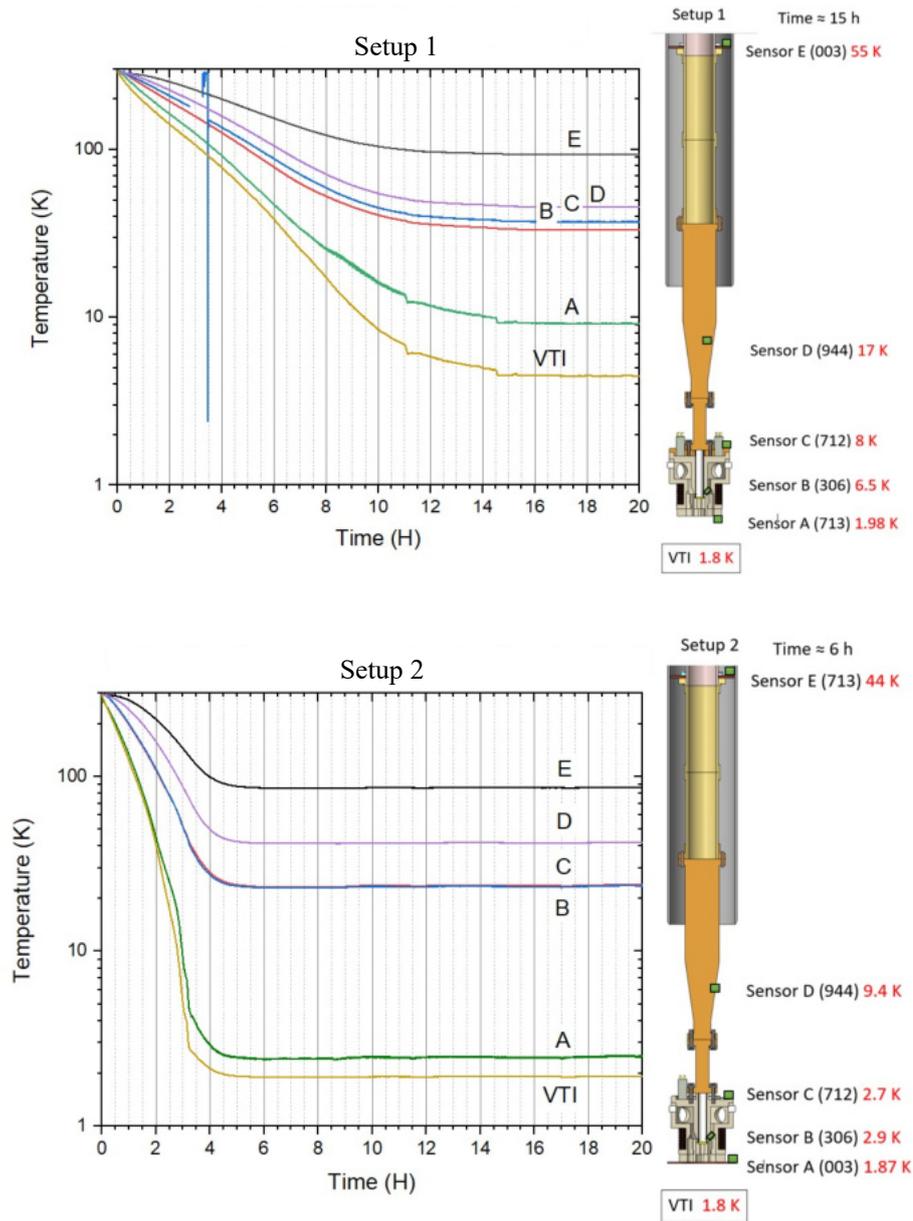
Fig. 4.25: EPR Probe temperature characteristic during the cooling. Five sensors were installed across the EPR probe. The difference between Setup 1 and 2 is in the brass part of FLF (in setup 2 was removed) and an additional copper plate for the increasing flow of cold He through the sample in Setup 2. In setup 1, the wrong pressure was set on the needle valve (too low). Therefore values at the scheme are taken after the needle valve pressure was fixed and temperatures stabilized. The time for cooling in setup 1 (15 h) was taken from another loading of the EPR probe, during normal spectrometer operation, with the same configuration of FLF and sample holder.

of other sensors was following: Sensor A was placed at the bottom of the sample holder. Sensor B was placed close to the sample cavity. Sensor D was placed on the focusing taper and sensor E on the lowest radiation shield.

Due to this improvement (FLF made of peek and disk mounted at the bottom of the probe), the lowest possible temperature of the sample decreased from 6.5 K to 2.9 K. Furthermore, the time needed to cool down the selection dropped by more than half. The biggest improvement was uninstalling FLF and thus decreasing thermal flow from the corrugated waveguide. Therefore, we are using FLF made of PEEK in the current setup with an average time to cool down the sample of approximately 8 hours (time was measured from the loading procedure of EPR probe with PEEK FLF during regular operating of spectrometer).

5 Sample Holders

This chapter expanded version of the accepted paper to the journal IEEE named: *Sample Holders for Sub-THz Electron Spin Resonance Spectroscopy* [127]. Reproducible, fast and user-friendly exchange of SHs is very desirable for any measurement system, not only to HF-EPR spectroscopy. It speeds up the setting of a typical experiment, prevents user errors, i.e. a bad wiring or misalignment, which may affect reproducibility of the experiment and waste expensive measurement time. For that reason, we developed a set of SHs compatible with the FLF (see Fig. 5.1). All parts of the SHs need to withstand an operating temperature between $4 - 400\,\mathrm{K}$ with negligible volume changes to keep the m.w. alignment and thus to ensure good m.w. coupling with the sample. Additionally, they have to be non-magnetic and preferably non-metallic in order to provide sufficiently large field modulation (B_{mod}) on a sample and to prevent generation of eddy currents. For these reasons we found PEEK to be an optimal material, and most parts of the SHs are fabricated with it. The PEEK withstand the required large thermal cycling in EPR experiments and is easy machinable with a good mechanical stability [128].

The design of different SHs can be split into two main categories: bottom-load and side-load SHs. The bottom-load SHs are easier to manufacture thanks to their cylindrical symmetry, have a modulation coil of a solenoid shape and provide an optimal m.w. alignment during the screwing of the functional part into the body. The side-load SHs possess an extra level of complexity that allows insertion via a side-load port of the airlock in case of air-sensitive samples or allow inserting multiple samples which can be loaded at once into the VTI, and use Helmholtz modulation coils. Both category are designed to have maximal outer diameter of $42\,\mathrm{mm}$ and can be split into three parts (Fig. 5.1): A) the Fast Loading Flange (FLF) that redistributes all the necessary contacts and is attached to the end of the corrugated waveguide; B) a body docked by four aluminium pins to the FLF with electrical connectors, and that contains a modulation coil and a smooth-wall m.w. waveguide; C) a functional part that contains the sample and is inserted into the body. All parts are described in the following text with greater details with demonstration measurements (the information about the sample preparation are in Appendix A). The assembly drawings of each sample holder are in Appendix B.

5.1 Methodology

This section will describe the main steps during the design of each sample holder. First, the simulation of modulation coil homogeneity and its calibration on the
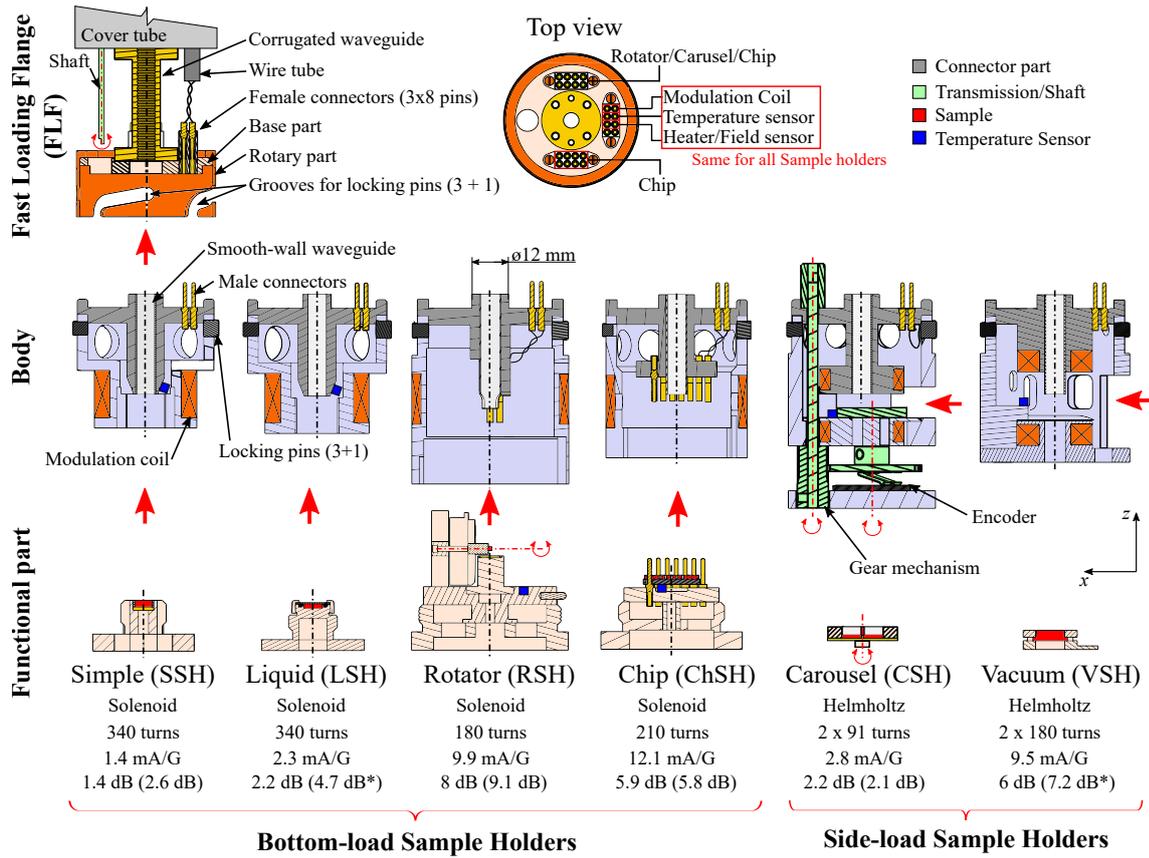
Fig. 5.1: Schematic picture of the sample holders' concept. The SHs can be divided into three parts: FLF attached to the end of the corrugated m.w. waveguide, body of SHs and functional parts, where the samples are located. All functional parts with their respective body are compatible with the FLF. The FLF consists of a set of three 8-connector blocks linked by wires to the probe head connectors, rotary part with grooves for locking pins at bodies, and shaft used in combination with step-motor to exchange sample in the CSH. During loading of bodies into FLF, all electrical contacts and m.w. alignment is made smoothly during the sliding of the locking pins into the grooves by rotating the rotary part of the flange. Furthermore, the bodies can be divided into two groups: *Bottom-load SH* and *Side-load SH* with solenoid and Helmholtz modulation coils, respectively. The *Bottom-load SHs* have a functional part with a sample screwed into the body, whereas the *Side-load SHs* have a sample placed on the platform inserted from the side. The functional parts with location of the SHs are also shown and are described in great details in Figs.3-6. Additional parameters of the modulation coils, including the number of turns, the current for creating 1 G at 1 kHz modulation, the m.w. attenuation at 430 GHz, and the average of m.w. attenuation of the assembled SHs measured in frequency range (260-500) GHz or (325-500)* GHz are listed.

sample are presented. Then, the prototyping of mechanical properties and user-friendly handling followed by the analysis of the m.w. propagation via VNA is discussed.

Modulation Coil: The modulation coil is one of the essential components of sample holders. The parameters of the modulation coils were simulated via the COMSOL Multiphysics® software (see Fig. 5.2).
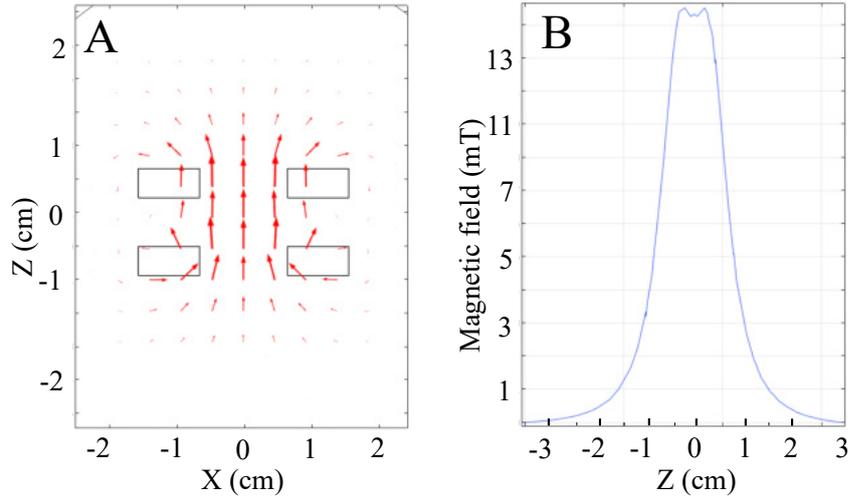
Fig. 5.2: Simulation of the Helmholtz modulation coil for the CSH. A) The 2D sketch of coils with vectors of modulation field with DC current applied. B) Magnetic field distribution along the coils axis.

The most important feature taken into account in the simulation was the homogeneity of the field in the centre of the modulation coil, to assure that the whole sample will be affected by modulation equally. The simulations were performed in the same manner for modulation coils of all SHs.

Tab. 5.1: Modulation coil constants for each sample holder.

Sample Holder (SH)	Conversion coefficient (G/mA)
Simple Sample Holder (SSH)	0.682
Liquid Sample Holder (LSH)	0.422
Rotator Sample Holder (RSH)	0.110
Chip Sample Holder (ChSH)	0.080
Carousel Sample Holder (CSH)	0.351
Vacuum Sample Holder (VSH)	0.105

By modulating the external magnetic field, we can achieve the EPR signal to noise enhancement by several orders. However, the big modulation amplitude can affects the shape of an EPR spectrum. Therefore, the modulation amplitude should not exceed ¼ of the EPR line width. Otherwise, the spectrum will be distorted - overmodulated (see Fig. 5.3). This phenomenon can be used for precise calibration of the coil. When overmodulated, the peak-to-peak line width is equal to the peak-to-peak modulation amplitude. In Fig. 5.3 A, we show the effect of overmodulation on the signal of LiPc. The spectra were measured in the frequency domain with different modulation amplitudes for faster processing, and a conversion factor of 28.012 MHz/mT (g = 2.0014 for LiPc) was used to recalculate the frequency to the field. For each sample holder, the measured values were linearly fitted (see Fig. 5.3). The conversion coefficient of the AC current to AC magnetic field for all sample holders are written in table 5.1.
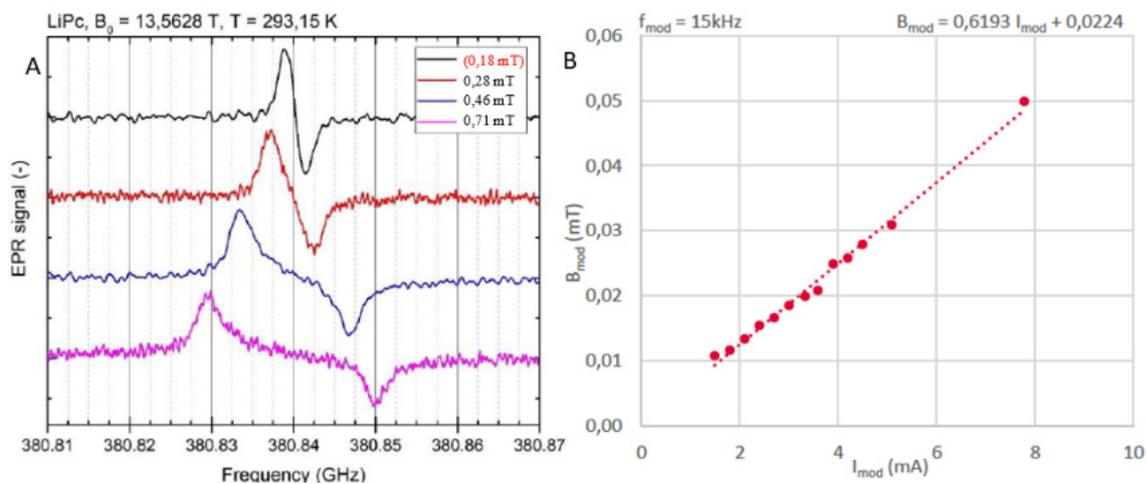
Fig. 5.3: A) Overmodulated ESR spectra of LiPC obtained during modulation coil calibration. The spectrum has to be overmodulated to allow determining the modulation amplitude. The black line corresponds to the case when the spectrum is not overmodulated enough to determine the modulation amplitude directly. However, it can be re-calculated from the calibration curve (value in brackets in legend). B) Field Modulation amplitude as a function of AC current in the coil and its linear fit.

Prototype testing: All 3D models and drawings were done in Creo parametric (PTC Inc., USA). After the 3D models of the sample holders were finished, models were 3D printed and troubleshot(see Fig. 5.4).

That allowed us to test them in terms of mechanical principles before putting them into the workshop to eliminate all possible problems that could occur during
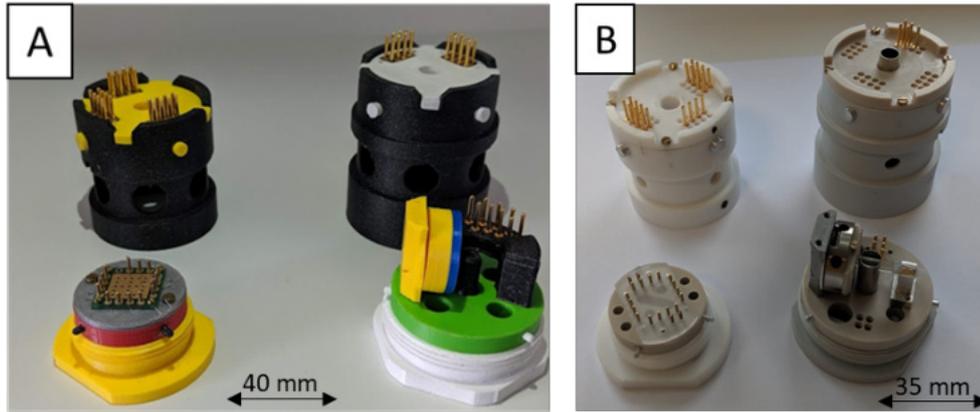
Fig. 5.4: A) Printed sample holders, B) Manufactured sample holders. On the left chip set sample holder, on the right crystal rotator.

the manufacturing or subsequent assembling. For 3D printing, we used a high-resolution 3D printer Delta M (TriLAB Group s.r.o.,CZ).

Vector Network Analyzer (VNA) measurements   The VNA measurements were done with a set of 260-400 GHz and 325-500 GHz frequency extenders (RSZC400 and RSZC500, RohdeSchwarz, Germany). The measurement configuration is shown in Fig. 5.5.
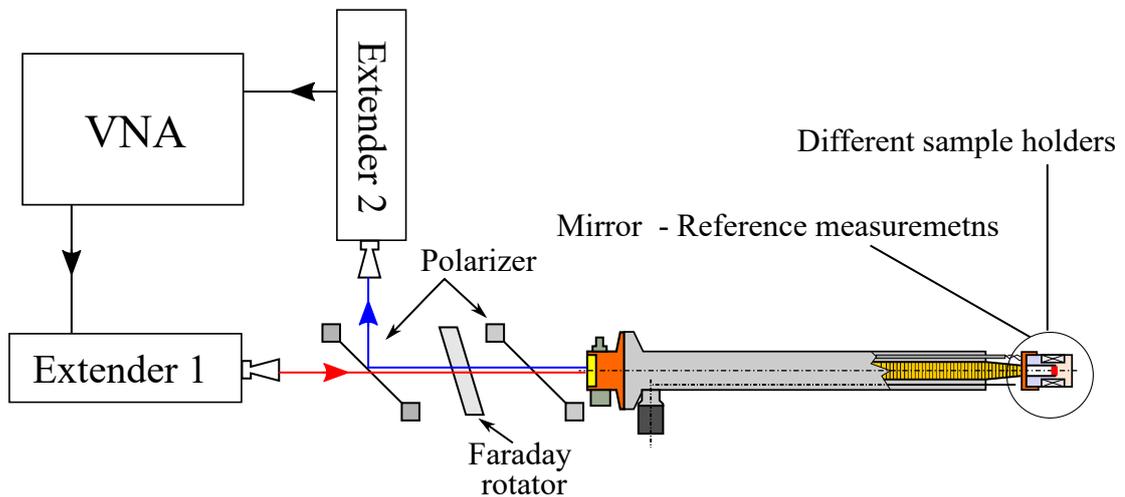
Fig. 5.5: Schema of the reference measurement configuration. The measurements normalization was done by putting the mirror at the end of the probe.

Data presented in this paragraph is not filtered but normalized to that obtained

83

with a mirror attached to the probe's end instead of SH (see Fig. 5.6 B). Due to this normalization, the measurements show the attenuation only from the sample holders itself. Fig. 5.6 A) shows the overall performance of SH calculated as the average attenuation of the microwaves over the measured frequency range. The error bars are calculated as the standard deviations. Red square marks show the results at 430 GHz, where the quasi optics have the best performance. The best performance SH is SSH as is also the simplest, the worst is RSH due to sapphire rod in the m.w. path.
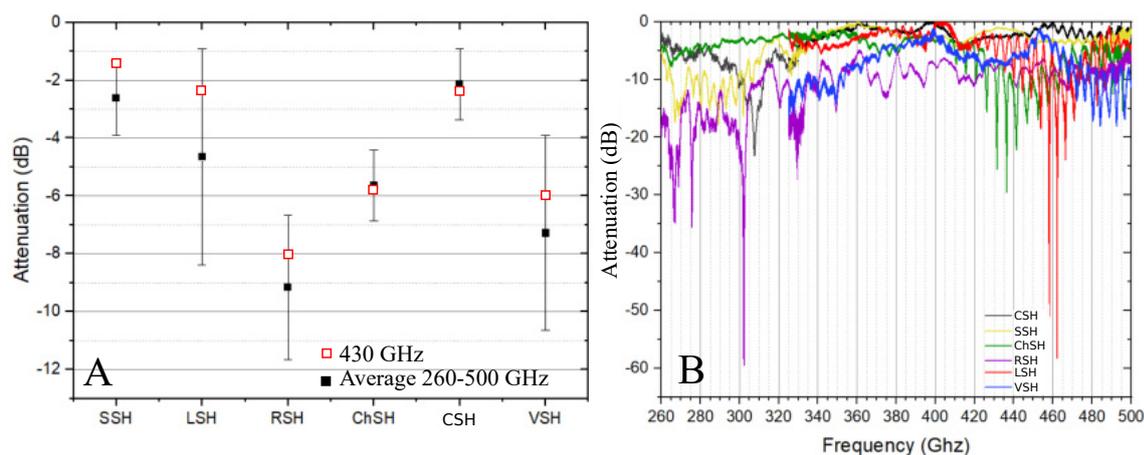
Fig. 5.6: A) Average attenuation of SH with the standard deviation. The red square indicates SH attenuation of m.w. at 430 GHz. B) VNA measurements over the whole frequency range.

5.2 Sample Holders Features

5.2.1 Body of sample holders

The body of SHs are made of PEEK with four aluminium pins to fit into FLF groves and several holes to allow effective Helium cooling. The body contain a modulation coil, smoth walled m.w. waveguide and a connectors part. As mentioned, we divide the SHs for bottom and side loaded, with solenoid or Helmholtz modulation coils, respectively. The precise field modulation amplitude was measured experimentally by overmodulating the EPR spectrum on a reference sample Lithium Phthalocyanine (LiPc). Obtained current values to create of 1 Gauss modulation at 1 kHz frequency are listed at the bottom of Fig. 5.1 including the type of coil and number of turns, wide from Cu 32 AWG wire (LakeShore Cryotronics Inc., USA).

Smooth walled m.w. waveguide out of aluminium has inner diameter 5 mm with the thickness of the wall 0.5 mm. It is pressed into the PEEK connector part of the body and aligned at FLF by a rim of diameter 12 mm to ensure proper m.w. coupling. The length of the waveguide vary from body to body and in case of rotating SH it has a cut out for entering a sapphire rod with a sample.

All SH bodies contain all necessary wire connections, therefore, there is no need for further interaction from the user besides the placement of a sample on a functional part. In case of simple, liquid, carousel and vacuum SHs bodies also contains T-sensor, only in case of rotating and chip SH the el. connections are further transferred from the bodies to functional parts.

5.2.2 Functional parts

All functional parts are designed to enable a visual and manipulation access to the sample, helping with its alignment and visual check outside of the SH body (for example by an optical microscope). The six functional parts for different sample types are described individually with illustrative HF-EPR measurements. If not indicated, m.w. mirrors reflecting the incident m.w. back to the corrugated waveguide are made of about 10 nm of gold deposited on $1\,\mu$m of aluminum to prevent oxidation on a $500\,\mu$m thick silicon wafer.

5.3   Description of Sample Holders

The six functional parts for different sample types are described individually with HF-ESR measurements:

Simple Sample Holder (SSH)

has the simplest functional part (Fig. 5.7). It is used for powder samples pressed into pellets of diameter 5 mm and thickness of (1-3) mm, or other solid materials (wafers or crystals) placed directly on the mirror with maximal dimension of cube with the edge 3.2 mm in order to fit in 5 mm diameter. The SSH functional part is manufactured from PEEK, is equipped with a 5 mm diameter smooth-wall cylindrical waveguide and a mirror at the bottom. This part is screwed into the body during the measurement, where the corresponding waveguides are aligned with a minimal gap. The simple construction results in the holder with the lowest attenuation of the m.w. (double pass) 1.4 dB (2.6 dB) at 430 GHz (average attenuation between 260-500 GHz) (see Fig. 5.1). Moreover, the holder's advantage is a large modulation coil,

which gives the best current to field conversion: $1.4\,\mathrm{mA/G}$, a useful feature when recording broad EPR lines where large modulation amplitude B_1 is preferable.
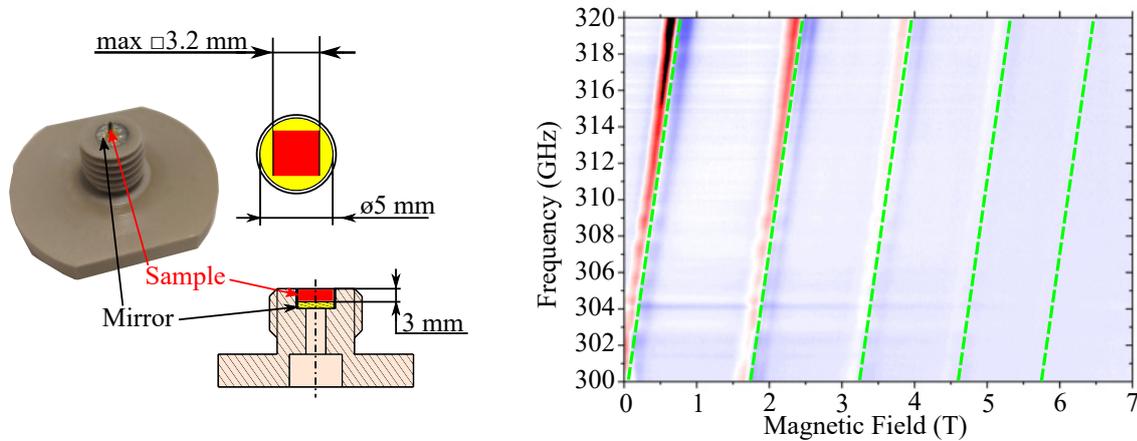
Fig. 5.7: Left) Photograph and drawings of the SSH functional part. A sample in the form of a crystal or a press powder pellet is fixed on the mirror by an EPR silent vacuum grease inside a $5\,\mathrm{mm}$ diameter waveguide. The maximal size of crystal that can be loaded into the SSH, is a cube of edge $3.2\,\mathrm{mm}$. Right) The measurement are showing EPR map 1200x800 resolution of $Mn_{12}Ac$ crystal together with simulation (green lines).

Fig. 5.7 shows test EPR measurements for this holder on $Mn_{12}Ac$ presented as a Frequency Domain Magnetic Resonance (FDMR) map. $Mn_{12}Ac$ is a coordination compound with the total spin S = 10. This is a good example of a system with zero field splitting, meaning that EPR lines are observed even without applying the magnetic field. The presented data shows that the sample holder is capable of measuring in both the frequency and field domains. Parameters of simulations: S = 10, g = [1.93, 1.96], D = - 13790.5 MHz, B_4^4 = 1.19917 MHz, B_0^4 = -0.659543 MHz.The parameters of the measurements: Temperature $12\,\mathrm{K}$, frequency sweep rate $40\,\mathrm{GHz/s}$, number of averages = 4, magnetic field sweep $0.25\,\mathrm{mT/s}$, modulation coil frequency $20.1\,\mathrm{kHz}$ and amplitude $5\,\mathrm{G}$.

Liquid Sample Holder (LSH)

is designed to study liquids or air sensitive samples, has a similar design to SSH with a few adaptations to the functional part, such as a viton o-ring and a sapphire window with a nut placed on top. A nut (PEEK) seals the sample cell upon screwing into a thread on the top of the functional part (Fig. 5.7). The hermetically sealed cell can hold volatile liquids in a vacuum environment for weeks. Since our system

also operates in the FDMR regime, the studied solution is placed directly on the mirror surface (located at the bottom of the sample cell), where the magnetic field component B_1 of the m.w. has its maximum amplitude [129]. The functional part can be manufactured with a groove of different depths for solvents with higher or smaller dielectric losses to get the best possible SH performance [130]. The attenuation of the m.w. is 2.2 dB (4.7 dB) at 430 GHz (average attenuation between 325-500 GHz) in an empty LSH. Apart from the 1-mm thick sapphire window in the m.w. pathway, LSH and SSH have a similar design, and therefore similar attenuation figures.

The data presented in Fig. 5.7 display the high-frequency measurements of 1 mM TEMPOL dissolved in acetone. We found out experimentally that a 4-mm deep groove with $40\,\mu$ L of solution provides good EPR signal. FDMR measurements of liquids at frequencies above 300 GHz are worldwide unique. In future, we want to expand this measurement by acquiring T_2 relaxation time via rapid scan (Fig. 5.7 A), which would boost DNP development [29–32].
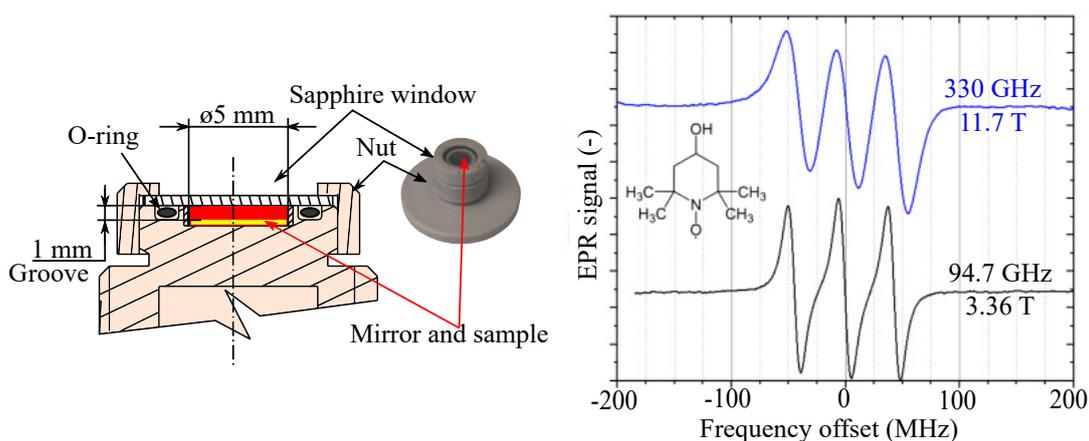
Fig. 5.8: Photograph and drawings of the liquid SH's functional part. The liquid sample is hermetically sealed in a cell with the o-ring and 1 mm thick sapphire window. The functional part can be manufactured with a different groove deepness according to the solvent needed for the measurements. B-Bottom) Frequency domain magnetic resonance (FDMR) measurement of 1 mM of TEMPOL in acetone at 330 GHz and 94.7 GHz at 300 K. The sweep time was 500 ms, with a field modulation of 6 G at 41 kHz. The final spectra is the average of 64 measurements acquired by lock-in amplifier.

Rotator Sample Holder (RSH)

is designed to rotate samples such as single crystals or thin films in the magnetic field during the HF-EPR measurements. The information extracted from those measurements can provide detailed information about anisotropy of magnetic interactions in paramagnetic materials or solid-state phenomena as cyclotron resonances in conducting materials [131–135].

The functional part consists of several cylindrical parts with holes providing a steady flow of Helium around the sample for a faster cooling down time. The top rotary base with the leading pin has one degree of freedom and can rotate 360 degrees. Three leading pins in the functional part and the guiding grooves in the body guarantee the correct alignment of the electrical contacts while the rotary base of the functional part allows transferring the rotary motion of the screw to linear motion. The unique position of the three leading pins ensures only one possible loading position (Fig. 5.9,). The RSH's functional part provides 11 contacts, five of them are used for the piezo-rotator (2) and built-in encoder (3), the remaining contacts are for T-sensor and an eventual heater or field sensor. A crystal sample is located on the sapphire rod (Crytur a.s., CZE), which is connected directly to a piezo-rotator (ANRv51/RES/LT, Attocube systems AG, DE). It can work at temperatures below $4\,K$, in UHV and high magnetic fields. Moreover, it has a built-in encoder allowing measurements with very fine resolution of $0.006\,°$ (Fig. 5.9 C). The direct connection of the sapphire rods minimizes errors caused by the rotation.

The mirror is placed $2\,mm$ under the axis of the sapphire rod. A magnetic field sensor can be placed under the mirror. So far, we have designed and manufactured two sapphire rods. One with a semicylindrical shape that offers the possibility of rotation and measurements of thin films or wafers. The second rod has a cylindrical shape that enables measurements of samples with a maximal cubic size with an edge up to $2.5\,mm$. To increase m.w. propagation the waveguide is prolonged down to the mirror with a cutout only for the sapphire rods (see Fig. 5.1). However, due to its complex structure, it has the largest return losses out of all SH, at $430\,GHz$ (average attenuation between 260-500 GHz) the return losses are of $8\,dB$ ($9.1\,dB$) with the semicylindrical sapphire rod.

The Fig. 5.9 in the middle and bottom displays FDMR rotation maps for a single crystal of copper acetate monohydrate $[Cu(CH_3COO)_2 \cdot H_2O]$. The four EPR signals observed at a single field/frequency correspond to the m.w. absorption by two rotated molecules in the lattice of this compound. The 0-280$\,°$ map was obtained by performing automated FDMR measurements and simultaneously rotating the crystal by a $1\,°$ step, whereas the detailed map in the range -10$\,°$-10$\,°$ has a 0.1$\,°$ step. This methodology with FDMR decreases measurement time from days to
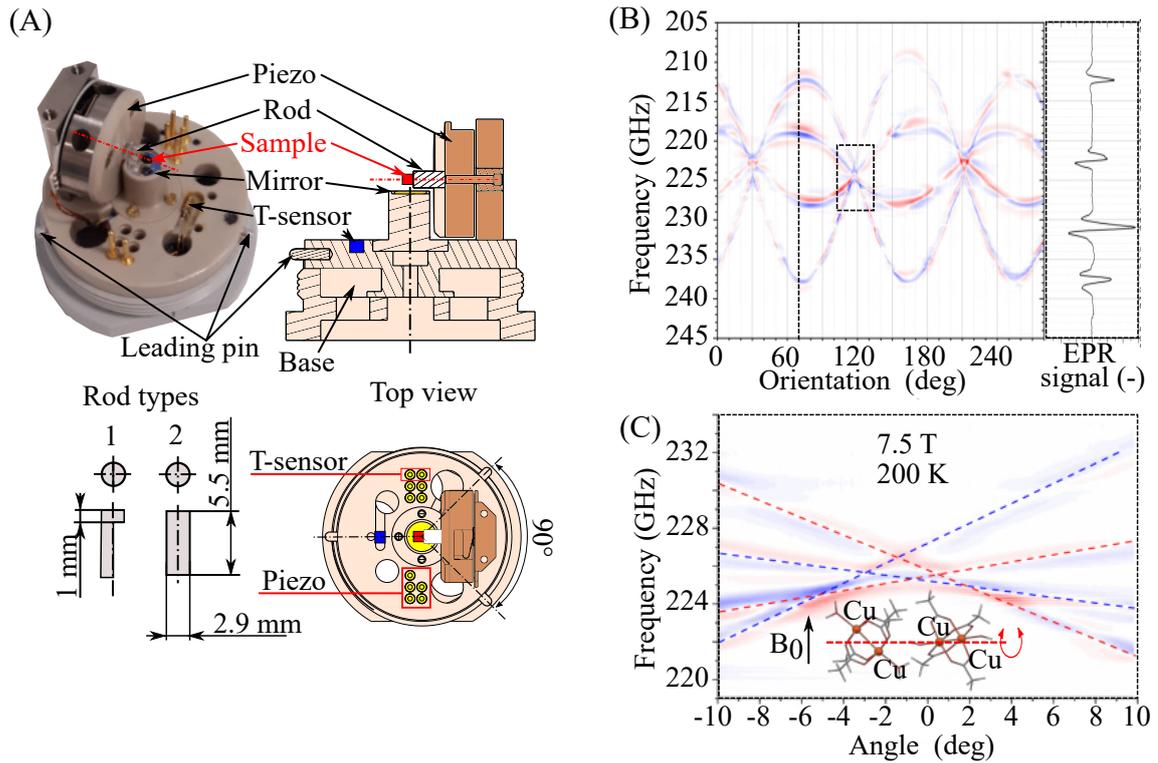
Fig. 5.9: A) Picture and drawings of the RSH functional part, rod types and top view. A sample is glued on the sapphire shaft by an EPR silent vacuum grease, eicosan or epoxy. Depending on the experiment, two types of rods are available. The first, with a *semi-cylindrical* shape, is mainly used for studying thin-layered materials (the maximal thickness of the layer is 1.2 mm). The second, with *cylindrical* shape, is used for studying crystals with a maximal size of a cube with 2.5 mm edge. The necessary electrical connection for piezo and T-sensor are connected automatically during the screwing of the functional part into the SH's body. The leading pins with unique orientation prevent the unwanted exchange of contacts. B) The rotation map of Copper acetate from 0 to 280° at a magnetic field of 7.5 T. The detail in the right displays a spectrum of one frequency sweep at 70°. The acquisition time of each FDMR spectrum is 16 s, and the map was measured in 103 minutes. C) A detailed map at the crossing of the EPR lines with an angular step of 0.1°.

hours, comparing to a field-domain measurement, and still, the spectrum at a single orientation can be extracted from the map.

Chip Sample Holder (ChSH)

allows characterization of electrical/electronic devices under m.w. irradiation or to perform magneto-transport measurements [136]. The functional part contains 20 connectors, 16 of them host a chip expander, while the other four connect the T-sensor and the heater. The chip expander is a small printed circuit board (PCB) with 16 gold deposited holes and contacts, prepared for wire-bonding of samples [136]. The maximal sample size which can be wire bonded is 8 mm x 8 mm. A small mismatch fit between the electrical connectors and the chip expander's holes guarantees tension for reliable connection. Any device prepared and wire-bonded to the chip expander can be easily loaded with the minimal user interaction (see Fig. 5.10). A sapphire heat sink is placed under the chip expander in order to dissipate the heat effectively to the sample. The heat sink has to be non-conductive to prevent short-cuts between contacts and eddy currents produced by the modulated magnetic field. Therefore, a sapphire plate was chosen for its non-conductance and good thermal conductivity at low temperatures [137]. The T-sensor and the heater are glued to the bottom side of the sapphire plate, which allows precise temperature control of the sample with an stability in the order of 10 mK. Furthermore, the effective Helium cooling is provided by holes in the functional part. Similarly to RSH, three leading pins in the functional part and the guiding grooves in the body guarantee the correct alignment of the electrical contacts, while the rotary base of the functional part allows transferring the rotary motion of the screw to linear motion. After screwing the functional part there is a gap between the sample and the waveguide to avoid touching wire bonds on the sample, resulting in a backward reflected EPR measurements with 5.9 dB (5.8 dB) loss at 430 GHz (average attenuation between 260-500 GHz).

The Fig. 5.10 shows an example of I/V characteristics of a graphene bolometer [138]. We tested the bolometer response to microwave radiation at 98 GHz (red line). The I/V response with (ON) and without (OFF) m.w. irradiation was measured at zero external magnetic field applied. The shift in curves is caused by m.w. irradiation and changes in the bolometer resistance. This represents the characteristic behavior of the bolometer [138].

Carousel Sample Holder (CSH)

was designed to load up to six samples in individual cells simultaneously inside a side loaded rotary platform in the functional part (see Fig. 5.11). The process of changing sample directly inside the magnet significantly reduce spectrometer usage time. The time-saving feature is especially significant for low temperature experiments. In the presented spectrometer, a typical time to cool down the SSH from 300 K to stable
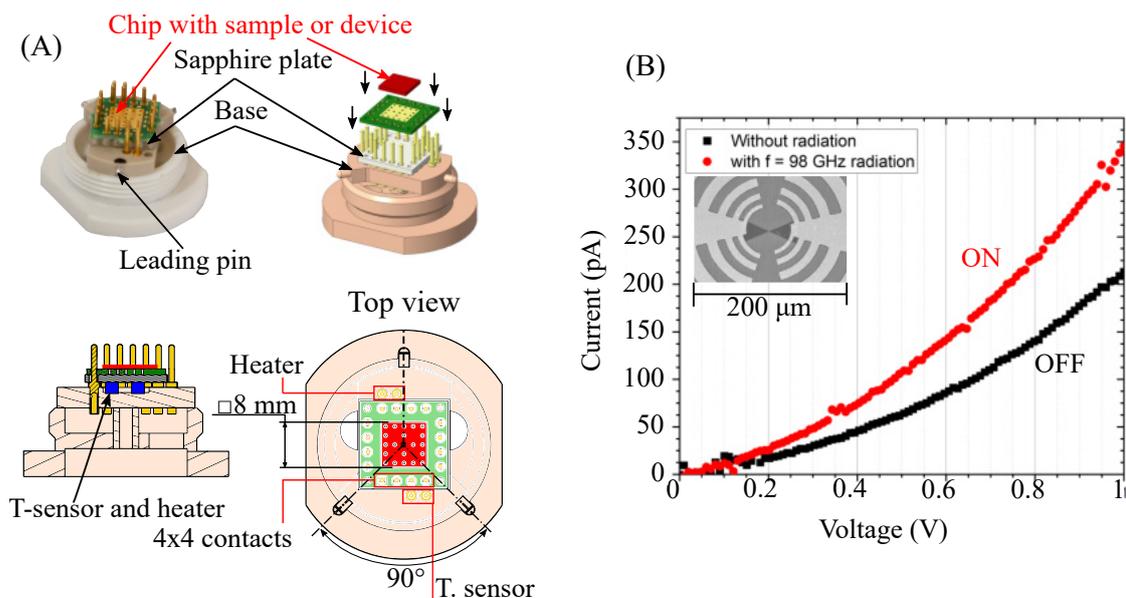
Fig. 5.10: A) Picture and drawings of the ChSH functional part. The T-sensor and the heater are under the sapphire plate, which works as a heat buffer. The sample is glued on the chip that is inserted into the male connectors of the functional part. The inter-space between the contacts is slightly bigger than the inter-space between the holes in chip, ensuring good electrical contact at any temperature. B) Measurements of a graphene bolometer's I/V curves with (ON) and without (OFF) m.w. irradiation at 15 K. The design of the bolometer is in the inset of the plot.

4 K is about 6 h. To exchange samples, the cryostat has to be warmed up before the EPR probe can be unloaded. This process takes an additional 1 h. With the carousel implementation, the user can switch between six samples directly in the cryostat without unloading the probe, thus saving overall up to 30 h. Moreover, one of the six cells can be used for the system optimization/calibration using a reference sample. Additionally, CSH is the best possible solution for future quantitative high field EPR applications, because the samples is switched directly inside the SH without changing the m.w. coupling. Each sample cell is 5 mm in diameter and 4 mm deep. For better m.w. propagation, the cells' walls are made from an aluminium smooth-wall waveguide as in the corresponding body.

The reflection in the CSH is achieved by a large home-made mirror shared by all cells cut from a silicon wafer coated by aluminum and gold in the same manner as previously mentioned. One large shared mirror minimizes the differences in the m.w. coupling between cells due to reflecting differences (see Fig. 5.12).

The precise position of the sample cells with respect to the body's waveguide is achieved by a piezo step motor (PiezoMotor Uppsala AB, SE) located outside
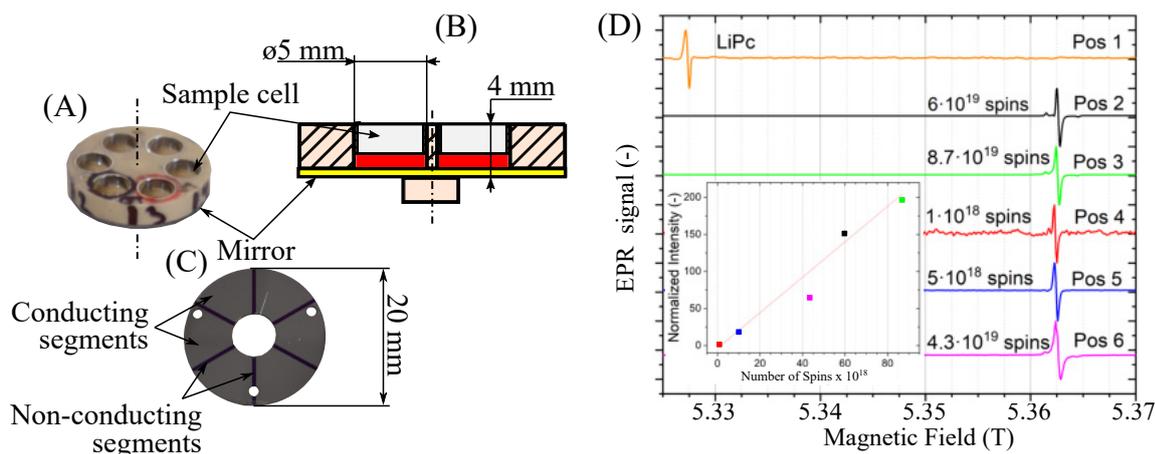
Fig. 5.11: A) Picture and B) drawings of the 6-cell rotary platform of the CSH. Samples are glued on the rotary C) platform's mirror by an EPR-silent vacuum grease. The mirror is divided into conducting and non-conducting segments, reducing the eddy-currents created by the modulation coil. D) Cw-EPR measurements using the different cells at room temperature loaded at once (five BDPA samples with different concentration and one reference LiPc sample). The magnetic field sweep was $0.5\,\mathrm{mT/s}$ with field modulation of $10.1\,\mathrm{kHz}$ and amplitude $30\,\mathrm{G}$. The measurements are normalized to the intensity of the weakest spectrum (red). The inset shows the plot of the normalized intensities for each sample against their number of spins. Changing among different samples takes a few seconds with the SH placed inside the magnet VTI.

of the cryostat. It is connected through a shaft to a gears mechanism in the body (Fig. 5.1) and with the rotating platform (functional part). With a $0.01\,°$ motor step and a gear mechanism (gears ratio $1/5$) made from brass, we have the theoretical step precision of $0.002\,°$. However, due to the large temperature operation range $(4 - 400\,\mathrm{K})$, all movable parts must have enough space, or a Teflon bearing, to avoid friction and freezing at low temperatures. With the temperature decrease, Teflon shrinks more than PEEK or metals, providing a clearance for rotation, but at the cost of the rotation accuracy [139]. To ensure proper m.w. coupling between the body and functional part, the positioning system is composed of a potentiometer/encoder ring (a graphite/silver thick film on the ceramic substrate, made by SEANT Technology s.r.o., CZE) glued to the bottom of the SH's body and a slider made of phosphor-bronze mounted directly to a bigger gear whose axis is parallel to the encoder axis and the sample functional part axis (Fig. 5.1). The encoder ring resistance is $22\,\mathrm{k\Omega}$ at room temperature, and $24\,\mathrm{k\Omega}$ at $4\,\mathrm{K}$. The feedback control of the SH is performed automatically via a script included in the home-built LabVIEW
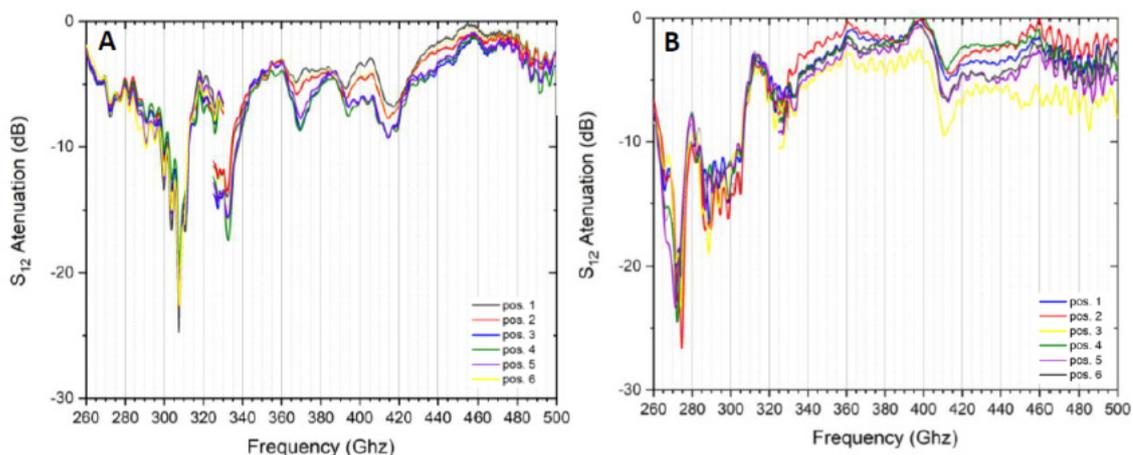
Fig. 5.12: Results from VNA measurements for invidual cells of carusel SH. A) Carusel cells share one big mirror, B) Each cell has its own mirror (diameter of 5.5 mm).

software (see Appendix D.3 for wiring of encoder and Appendix E.1 for positioning software) of the FRaSCAN spectrometer. It measures the resistance at the actual position and resistance of the whole ring by the application of a constant current value. The ratio between these two values does not change with the temperature. With this system, we can change the sample cell within our temperature working range with the precision of $0.05°$ and ensure good m.w. coupling. The m.w. attenuation in the CSH is $2.2\,dB$ ($2.1\,dB$) at $430\,GHz$ (average attenuation between $260\text{-}500\,GHz$). The worse results of the m.w. attenuation compared with the SSH is due to a small gap (≈ 0.2) between the waveguide in the connector part and the platform, and waveguide mismatches.

Preliminary results of our quantitative EPR measurements are shown in Fig. 5.11. The CSH was loaded by five differently concentrated α,γ-Bisdiphenylene-β-phenylallyl (BDPA) samples and one LiPc reference sample. The intensity of BDPA signal from each sample follows its concentration (see insert in Fig. 5.11).

Vacuum Sample Holder (VSH)

in combination with a mobile UHV suitcase allows to study air-sensitive structures prepared in a UHV chamber. It is based on an Omicron plate (Scienta Omicron GmbH, DE) for transporting air-sensitive samples which are often manufactured and studied in UHV systems (Fig. 5.13).

A sample in the form of a deposited layer on a single crystal of Copper, Gold, Iridium etc. (Structure Probe Inc., USA) or on a wafer is fixed to the Omicron
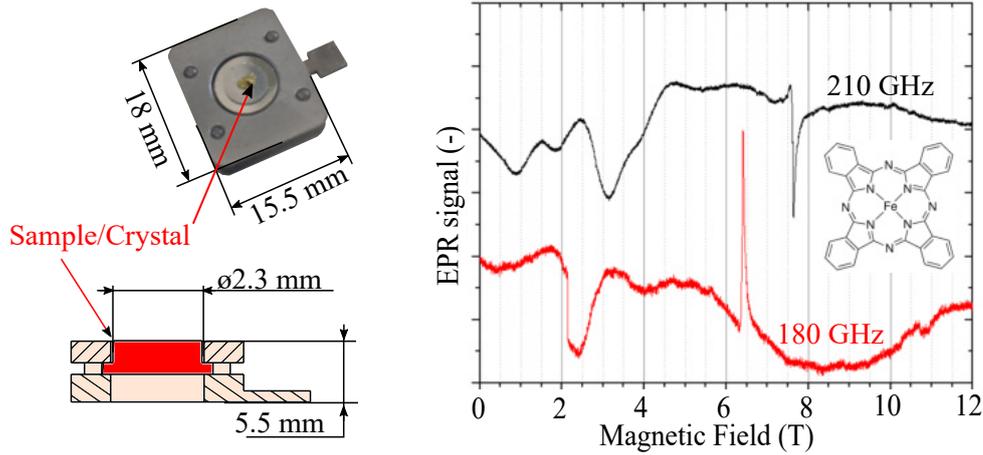
Fig. 5.13: Left) Picture and drawings of the VSH's functional part. The different crystals made of aluminum, gold, silver, or copper can be fixed between two Omicron plates, and the studied structure is then deposited on the top of it. Right) The cw-EPR measurements of Fe-Pt pressed-powder pellet placed on the functional part.

plate and side loaded into the VSH. A crystal or a wafer serves as the mirror for EPR measurements. The m.w. attenuation of the holder is 6 dB (7.2 dB) at 430 GHz (average attenuation between 325-500 GHz). However, the size of the crystal and the metallic plate decreases efficiency of modulation coil (Fig. 5.1). Thanks to the VSH, HF-EPR measurements are possible in addition to the XPS (X-ray photoelectron spectroscopy), STM (Scanning Tunneling Microscopy), LEED (Low-Energy Electron Diffraction), and other techniques often used in nano-fabrication clusters [140–142].

The proof of concept EPR measurements were done with pressed-pellet of Iron(II) phthalocyanine (FePc) placed on the Omicron plate (Fig 5.13), one of the candidate for future deposition in UHV.

6 Rapid Scan Measurements

This chapter presents the rapid scan measurements performed in the FRaSCAN EPR. The majority of Rapid Scan results presented here are measured on an LiPc crystal because of its narrow and thus intense line at room temperature, enabling the measurements with our available synthesizers. A sample with a broader signal must employ different RF sources that allow sweeping fast over a wider frequency range. At the end of the chapter, a rapid scan of BDPA dissolved in toluene is presented. All Rapid Scan spectra simulations were done by Dr. Oleksii Laguta.

It is important to note that the spectrometer is still under development. That means that the spectrometer's sensitivity, discussed in the following section, will differ in a few months as the improvement and troubleshooting proceed. The change in the frequency domain is more dominant as we focus on reducing standing waves. The example is shown in Fig. 6.1.
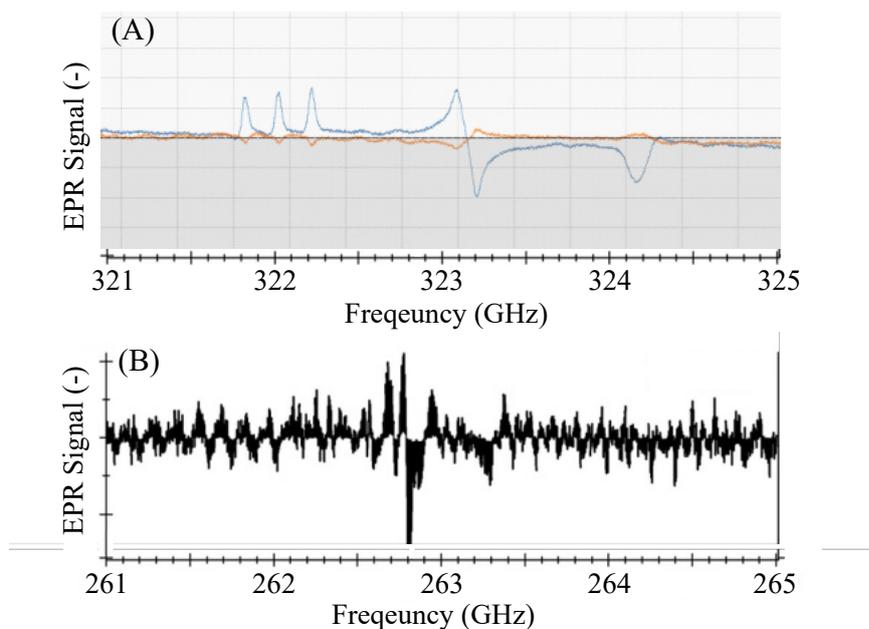
Fig. 6.1: Two spectra of TEMPO of concentration 10^{14} spins in polystyrene measured in FDMR show progress in troubleshooting over time. The difference between the spectra except for a slightly different setting is one-year troubleshooting and improvements of FRaSCAN EPR and sample holders. The main imporvements are discussed in the text bellow. Spectrum A) was measured with mylar foil as the EPR probe window, the wires connected to the sample holder are placed in two grounded stainless steel tubes, and the inner diameter of the sample holder waveguide is 5 mm. A) Signal from 5/2021. B) Signal from 7/2020.

Two spectra of TEMPOL in polystyrene were measured at 20 K with a time step of one year. Fig.6.1B shows one spectrum where the signal is barely visible, and a lot of post-processing and averaging had to be added. Fig.6.1 A is showing the print screen of lock-in without averaging. The improvement in sensitivity is visible at a glance. The main improvements were:

- EPR probe window

In the beginning, the HDPE window was used until it was found that it caused an intense standing wave pattern, which could bury the EPR signal in some cases. Therefore, if the spectrometer is used to record EPR maps using frequency domain EPR, the user should always use a mylar foil of thinkness $50\,\mu$m as the window. The mylar foil is replaced after several EPR probe loads to avoid unwanted foil breaking.

- Wiring

Before, wires were placed along the waveguide in one big string, causing interference between the wires. Moreover, the modulation coil was connected via stainless steel coaxial wire due to low thermal conductivity. Low electrical conductance was the reason for more noise in the spectrum, and drops in modulation current were often observed. Nowadays, wires go from probe head to FLF and sample holders in two separate stainless steel tubes. The signal wires are placed in one of them, and the wires for modulation coil, temperature, and field sensor are placed in the other one. The modulation coil is now powered by copper wires.

- The waveguide in Sample Holder

Before, the waveguide in a sample holder had a diameter of 5.5 mm. The reason for this dimension was good availability on the market. However, the diameters of the EPR probe waveguide (5 mm diameter) and the sample holder's waveguide did not match. Nowadays, the waveguide has a diameter of 5 mm. Moreover, the sample holder waveguide is more precisely aligned to the EPR probe waveguide through an additional rim (12 mm diameter).

6.1 Sensitivity

Generally, the EPR sensitivity is calculated from equation 3.1. However, many of the parameters are not well known in our case. Therefore, the sensitivity of the spectrometer was determined from the dependence of the SNR on sample spin concentration. The calculation follows the sensitivity determination shown in [33].

To demonstrate continual development first data for determining sensitivity were taken from the Carousel sample holder measurements (shown in section 5.1.2). If

the numbers of spins to SNR for each sample is plot and fit by linear functional (or assuming of linear function divided by SNR), it can be estimated minimal absolute sensitivity for SNR ratio equals to $1.3 \cdot 10^{17}$ spins. To determine the absolute sensitivity at room temperature, the number of spins is divided by detection bandwidth (50 ms), and line-width of spectrum 30.1 G. The exact calculation follows:

$$N_{CSH-minimal} = \frac{3.16 \cdot 10^{17}\,\text{spins}}{30.1\,\text{G} \cdot \sqrt{20\,\text{Hz}}} = 5 \cdot 10^{14}\,\text{spins}/(\text{G} \cdot \sqrt{\text{Hz}}). \qquad (6.1)$$

The absolute sensitivity was measured for SSH as well. Sample, DPPH in polystyrene, was made with concentration of 10^{15} spins (number of spin in the whole sample) and measured at 100 GHz. The detection bandwidth (1 ms) and modulation 15 G was used. The measurement results in SNR of 320, then the absolute sensitivity for SSH is:

$$N_{SSH-minimal} = \frac{10^{15}\,\text{spins}}{320 \cdot \sqrt{1\,\text{Hz}} \cdot 15\,\text{G}} = 2 \cdot 10^{13}\text{spins}/(\text{G} \cdot \sqrt{\text{Hz}}). \qquad (6.2)$$

Compared to the spectrometer described in reference [33] with sensitivity $5 \cdot 10^{10}$ spins, our sensitivity is worse. The low sensitivity is caused by performing the measurements at 150 GHz and 100 GHz ranges, where the QO is not well-optimized. Moreover, the result shown in [33] were obtained at 320 GHz and 60 K, using bolometer as the detector, which have generally higher sensitivity. As the spectrometer is still in development, it is expected that this number will get better in near future.

6.2   Rapid Scan measurements with FRaSCAN EPR

In the following experiments, the VDI synthesizer was used as the source of m.w. with the maximal sweep of 25 MHz/μs. The scheme of setup for the rapid scan is shown in Fig. 6.2. The main difference between this setup from FDMR setup used for previous measurements is in the digitizer and DC current source. The digitizer ADQ7DC (Teledyne Inc., USA) is an ultra-fast AD converter with a speed of Gsamples/second. That allows us to make hundreds of thousands of averages and thus seek for weak signals. Moreover, it is not possible to use a modulation coil in the rapid scan (modulation is too slow). Instead of that, the modulation coil is fed by a DC signal for shifting the signal resonance in the field and realizing background subtraction. This procedure will be discussed further in this text.

The main requirements for performing a rapid scan measurement is to sweep the microwave angular frequency f or magnetic field B_{ext} faster than the spin relaxation of the system:

$$\gamma \left| \frac{dB_{ext}}{dt} \right| \geq \frac{1}{T_2^2} \qquad or \qquad \left| \frac{df}{dt} \right| \geq \frac{1}{T_2^2}. \qquad (6.3)$$

Fig. 6.2: The schematic drawing of FRaSCAN setup for Rapid scan. Instead of a lock-in, a digitizer is employed to acquire the data. The modulation coil is fed by a dc current to shift the resonance between the measurements.

In this manner, the system with long spin (ms) relaxation time does not require such high sweep rates. For systems with shorter relaxation times (ns), it is harder to perform the rapid scan technique, especially in the field domain as the fast field sweep is more complicated. Our setup can generate a frequency sweep scan of 10^5 THz/s, which allows measuring T_2 times in the nanosecond scale. The exact rate in the field domain would be 10^7 T/sec, which is impossible nowadays. Furthermore, the rapid frequency scan allows us to perform rapid scans within the spectrometer range.

The downsides of rapid scan EPR in the frequency domain are undoubtedly the standing wave pattern and low power sources. Both have negative effects on the final spectrum. In our setup, we try to decrease the effect of the standing wave to a minimum by a thin Mylar window on the EPR probe (see Fig. 4.24) and additional QO filtering in terms of Faraday rotator and wire grid in front of XP mixer. Nevertheless, it will not completely attenuate the standing wave pattern, and the rapid scan signal is still buried in a broad low-intensity signal. The background correction for the narrow signal as LiPC can be done simply by applying the DC signal in the modulation coil, as shown in Fig. 6.3. In short, the whole description of the procedure is as following: first, the signal with background is measured. Then the signal is shifted by applying DC in the modulation coil, and only the

Fig. 6.3: The example of the method for background treatment using modulation coil to shift the sample on and off-resonance. Due to a crack in the single crystal final spectrum has a non-regular shape. (A) First, the Rapid scan signal is measured (blue). Then, the DC current of 1 A, in this case, is fed into the modulation coil, which causes a shift of the resonance, and the background spectrum is measured (green). B) The subtraction of spectra from each other results in a rapid scan signal without background.

background spectrum is measured. The substation of these two spectra results in the Rapid scan signal. This method works well only for narrow signals at room temperature. One of the reasons is heat due to the current, which is fed into the modulation coil. As the applied current raises, the introduced heat from a large DC influences the temperature in the sample holder, causing a background change. At low temperatures, this problem occurs even with narrow signals. Still, it can be partially avoided by applying the DC even during the first acquisition, and then for measuring the background, DC polarity is switched.

6.3 Rapid scan measurement at high frequencies

This section is the summary of the article [143]. For the case when the resonance line contains only homogeneous broadening, the EPR spectrum can be simulated,

and T_2 relaxation time can be numerically extracted via equations shown in sub-section 2.4.2. However, the rapid scan spectrum at high frequency also contains non-homogeneous broadening. The broadening is caused by (hyper)fine structure, g-factor anisotropy, g-strains, and nonuniform magnetic field distribution over the sample. Fig. 6.4 shows the fit of the rapid scan signal with homogeneous and non-homogeneous broadening at 430 GHz. The non-homogeneous broadening precludes the equations in subsection 2.4.2 to simulate rapid scan with an additional parameter. Moreover, the experiment needs to be changed too. Due to broader lines, the necessity of faster sweep rates as the condition becomes:
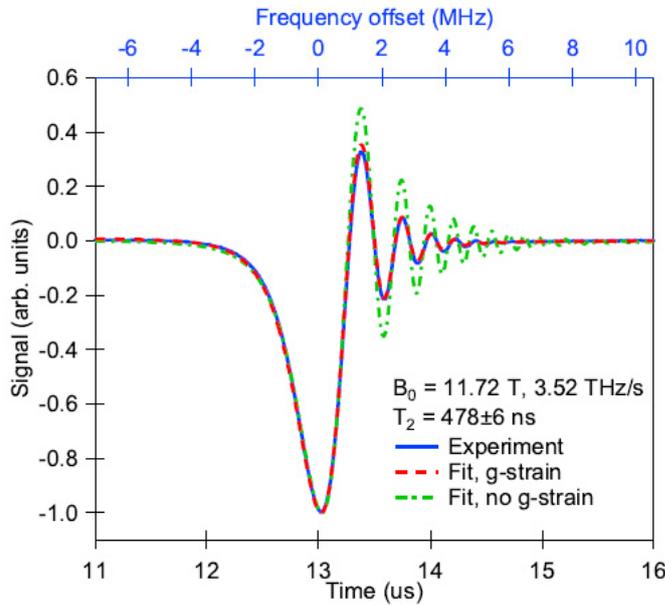
Fig. 6.4: An example of rapid scan ESR acquired on a single microcrystal of LiPc (blue) and its fit with homogeneous (green) and in-homogeneous (red) broadening models. Incident microwave power is 1mW, 10^4 averages, total acquisition time is 5 s. Published in [143].

$$\left| \frac{d\omega}{dt} \right| \geq \Delta\omega^2, \tag{6.4}$$

where $\Delta\omega$ is the half-width at half maximum of the slow scan EPR spectrum characterized by relaxation time:

$$T_2^* = \frac{1}{\Delta\omega} < T_2. \tag{6.5}$$

The sweeps rates are not such a problem in the modern spectrometer, where rapid scan on any ESR line with $\Delta\omega$ up to 100 MHz can be recorded [28]. However, to be able to simulate non-homogeneous broadening, the Bloch equation has to be modified by an additional relaxation mechanism. Such a modification is rather complicated as there typically several non-homogeneous broadening sources are involved. Regardless of the origin of non-homogeneous broadening, the resulted slow scan ESR spectrum is a sum of contributions from individual spin packets. The individual rapid scan responses from the overall spectrum can be written:

$$r(t) = (\sum_i s_i * d)(t) = \sum (s_i * d)(t) = \sum r_i(t). \tag{6.6}$$
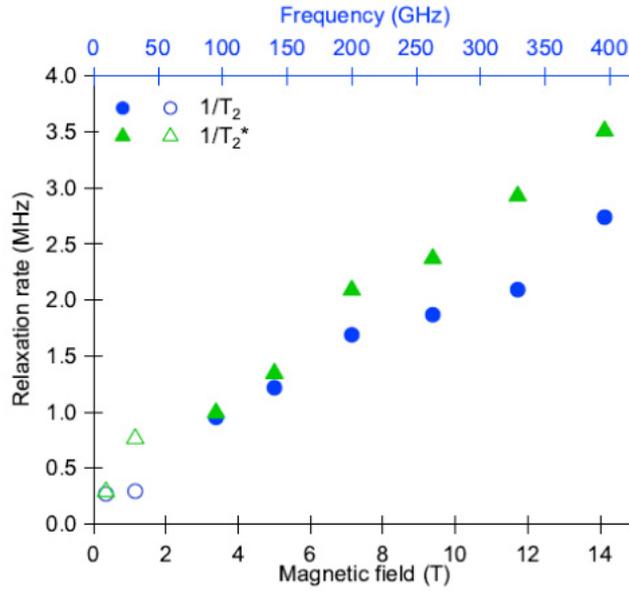
Fig. 6.5: Magnetic field dependence of the electron spin relaxation times T_2 and T_2^* for a LiPc single crystal sample at room temperature lying on the mirror that B_0 field is perpendicular to the crystal axis. Low field values (open markers) are taken from [144]. Figure taken from reference [143].

Then, the rapid scan spectrum of a complex system can be obtained as a weighted of these sum of the solutions of the Bloch equations. The demonstration of this theory was done on LiPc crystal needle (see Fig. 6.4). The benefit of LiPc is an extremely narrow signal width of 50 KHz at X-band [144]. The linewidth became broader with higher frequencies. That can indicate the shorter spin-spin relaxation time T_2. The origin of the non-homogeneous broadening in LiPc is probably unresolved hyperfine splitting from Li and N nuclei and g-factor strain. Fig. 6.4 shows that without the g-strain (green), the oscillation is more dominant than simulation

with g-strain (red), which matches well with the experiment data. The simulation with the g-strain was done by calculating 30 rapid scan spectra with the normal distribution of g-factor, then they were summed up with the corresponding weights.

In Fig. 6.5 is shown the spin relaxation rate of LiPc in the range of our spectrometer where the signal can be obtained (0-15 T, 80 - 400 GHz). This is proof of the capability of our spectrometer to perform a rapid scan within the 400 GHz range (higher frequencies were not done due to insufficient magnetic field).

6.4 Rapid Scan with the Rotator Sample Holder
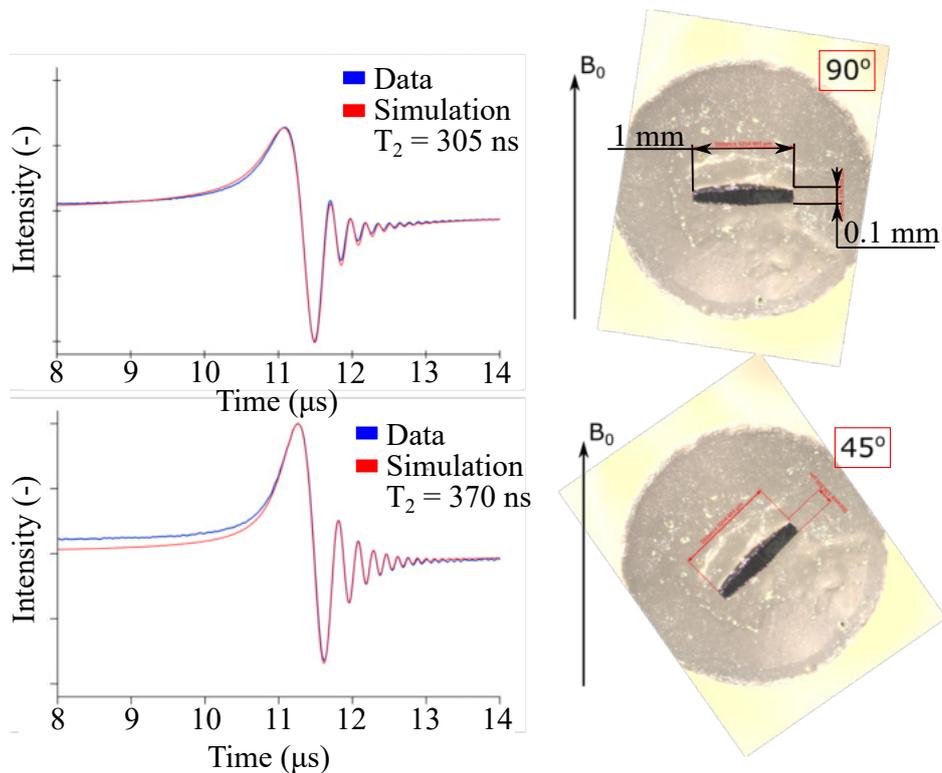
Fig. 6.6: Rapid scan measurement on LiPC with the different crystal direction to magnetic field B_0. Sample was glued to the rod of RSH by epoxy. Parameters of the measurement: $B_0 = 5.452$ T, T = 293 K, frequency sweep 152.56 - 152.63 GHz, number of averages 2 000 000.

This section presents a study of the spin relaxation of crystals during their rotation in a magnetic field using the RSH. The test sample, LiPc crystal, was glued by epoxy to the rotator rod, and then rapid scan measurements were performed with different orientations (see Fig. 6.6). The spectra were obtained at room temperature and B_0 of 5.5 T, corresponding to the m.w. frequency in the 150 GHz range. Even

without quantitative analysis, it is seen that the oscillations' amplitude is smaller for the crystal orientation perpendicular to the magnetic field, meaning the shorter spin relaxation time. The spectra simulation with the modified Bloch equations resulted in $T_2 = 305$ and $370\,$ns for the perpendicular and $45\,°$ orientations.

From the measurements performed with pulse X-band EPR [145], it is known that LiPc acts like a 1-D organic conductor (T2 depends on the direction of magnetic field relative to the conductive direction) with the slowest spin relaxation when the crystal is oriented perpendicularly to the external field B_0. However, the measurement at high fields shown in Fig. 6.6 suggests that a redistribution of different relaxation mechanisms occurs. A detailed study has to follow within a broader field range and finer angular steps to understand these results. However, this is the only demonstration of how the rapid scan on the FRaSCAN EPR spectrometer can be used in the future.

6.5   Rapid scan on radicals with Liquid Sample holder

In this section, the combination of Rapid scan with the LSH is presented. The measurement in Fig. 6.7 demonstrates the proof of concept and the possibility of using our spectrometer to study the relaxation time of radicals in liquid solutions.
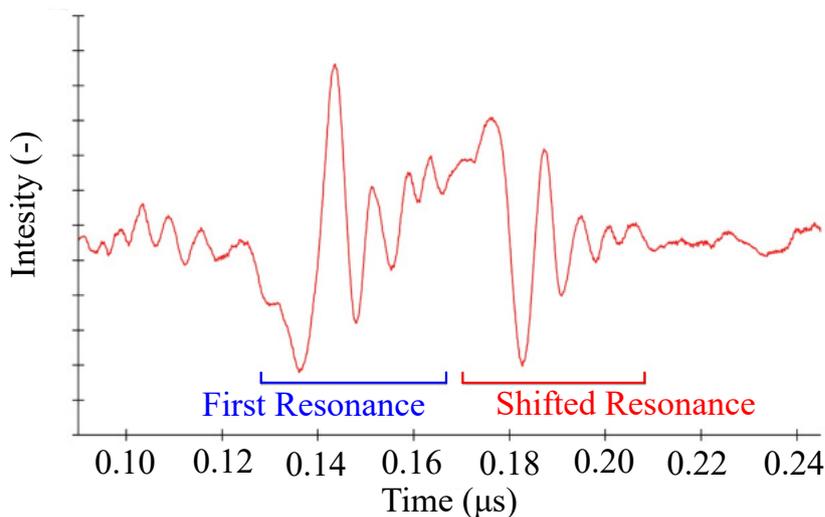

Fig. 6.7: Rapid scan measurement of 2mM BDPA dissolved in toluene. The not-degassed sample (≈ 50 nl) was sealed in LSH. The parameters of the measurements: frequency generated by AWG at 390 GHz in chirp pulses of 1.8 GHz (V Shape), sweep rate 0.5 μs, T=293 K, $B_0 \approx 14$ T, number of averages = 2 000 000.

BDPA dissolved in toluene at 2 mM concentration was measured at 390 GHz. The sample was not degassed, making the signal broader and less intense due to the presence of oxygen [146]. Two resonance signals result from shifting the main signal (see Fig. 6.7 blue) via DC in the modulation coil. Higher current, which would shift the second resonance out of the measurement spectra, was not used due to the limit of the used current source (2.5 A). Our synthesizers could not sweep sufficiently fast over the signal area in these particular measurements. Therefore, AWG replaced them to generate a broader sweep (chirp pulses of 1.8 GHz (V Shape) with a sweep rate of 0.5 μs.), which was necessary to see rapid scan oscillations. Moreover, the detector mixers were replaced by zero bias detectors due to unstable dual-channel AWG output, resulting in the wrong synchronization of LO and RF lines. The final spectrum is the result of 2 000 000 averages. Despite that, the background of the spectrum is significant, which made it impossible to simulate the rapid scan signal. This measurement is proof of the applicability of our spectrometer for the study relaxation times of radicals but further work will be needed to improve the method.

Conclusion

This work focused on the development of an EPR spectrometer with the main goal of measuring relaxation times via Rapid Scan, called FRaSCAN EPR. The main properties of the FRaSCAN Spectrometer are frequency range $80 - 1100\text{GHz}$, magnetic field range 0 ± 16 Tesla, Sample temperature from $2 - 400$ K, and possible to run continuous wave EPR experiments in field domain and frequency domain (even simultaneously), and rapid scan EPR. This thesis is split into two main parts, the theoretical and practical ones. The basic theory of EPR spectroscopy, the advantages of EPR in the high field, the spin relaxation phenomenon, the main parts of the HF-EPR spectrometer with the QO transmission system are described in the theoretical part encompassed among chapters 1 to 3. The designed spectrometer, the sample holders with proof-of-functionality measurements and the rapid scan measurements are shown in the last 3 chapters.

The spectrometer consists of three standalone parts: magnet frame, EPR table, and EPR probe. The magnet frame holds the superconducting cryogen-free magnet in the lab pit. Therefore, loading the sample into the magnet is in an user-friendly height. Furthermore, the magnet frame contains the automated docking desk with all electronics, computer ports, and the servo-driven movement system for coupling different tables with the superconducting magnet. The switching of tables was demonstrated with FIR and EPR tables. One important part of the magnet frame is the designed airlock system, which allows loading the EPR probe into the magnet VTI without air contamination. The airlock was designed with a side valve and window, which allows the transfer of sensitive samples into the probe inside the airlock via a designed UHV transfer case. The EPR table has a frame with a retractable wheel which allows it to be undocked from the magnet frame. The EPR table contains all electronics and m.w. components, which are needed for the EPR experiment. It contains m.w. sources and detectors, quasi optics solution to couple the m.w. with EPR probe, electronics needed for EPR experiments (lock-in, digitizer, source-meter. power sources), and four servo-driven movement systems for automatic m.w. coupling between the EPR table and EPR Probe. Proof-of-concept test shows that automatic procedure significantly reduces the time needed to couple the m.w. beam between the table and probe. The last part of the spectrometer is the EPR probe. The EPR probe is the long corrugated waveguide shielded by a stainless tube with an opened bottom end and with window at the top. The stainless steel tube serves for differential pumping during the loading of the EPR probe into the magnet through the airlock. At the bottom of the EPR probe is the FLF, which reduces the sample holder preparation and loading to a minimum time. Thanks to FLF, wiring, and m.w. coupling of the sample holder is reduced to the

minimum. The part of the design was also the study of m.w. attenuation by VNA and Tk power meter, study the cooling dependence of the EPR probe, and testing and troubleshooting of all mechanical parts.

In total, six different sample holders were designed and troubleshot. All sample holders are shown together with the measurement as the proof-of-functionality. SSH for measuring press powder pellets or crystals with Mn_{12} EPR map, RSH for oriented crystal measurement with rotary map measurements of copper acetate, ChSH for testing devices under m.w. with the test of the bolometer, Liquide SH for measuring liquid samples with measurement TEMPOL dissolved in acetone, CSH for measuring up to six press powder pallets with the example of quantitative EPR measurements done with five differently concentrated BDPA samples, and VSH for measure air-sensitive samples prepared in UHV cluster with measurement of press powder pallet. Moreover, m.w. VNA studied attenuation in sample holders to improve overall performance. VNA measurements were used for the inner diameter of the waveguide optimization and to know which frequencies to avoid during the EPR experiments for each sample holder.

The end of this thesis is focused on rapid scan measurements. At the beginning is shown how to calculate the sensitivity. Even the sensitivity ($5 \cdot 10^{14}$ spins/(G $\cdot$ $\sqrt{Hz}$)) results to below others HF-EPR spectrometer ($5 \cdot 10^{10}$ spins/(G $\cdot \sqrt{Hz}$)) [33], the spectrometer is under constant development. As the specter's troubleshooting continues, I believe that this number will decrease to the point that spectrometer sensitivity will get to the state-of-the-art point. Even while I was finishing this thesis, the crucial problem in orientation XP mixer, which attenuates signal by 3 dB, was found. Nevertheless, I would like to mention a few suggestions that would be worth investigating in the future to improve spectrometer sensitivity:

- First of all, the ground of the detectors. The noise of different frequencies was present from time to time during the measurements. I would recommend avoiding any ground loops which would be found. Moreover, all the grounds should be connected to one line separated from the power grid.
- Secondly, I would recommend a more deep analysis of XP isolation and leakage from CO into XP when the m.w. propagate into the EPR probe. We recently found out that there is quite a big leakage of LO into the XP detector. The origin is unsure yet. It is mainly visible when the high power output of m.w. source is used. If the origin is in the probe, one solution might be to implement a roof mirror that can rotate under the sample to increase XP isolation.
- Thirdly, I recommend checking the modulation coil wiring connection as some modulation frequencies create random signal steps in EPR spectra.

The last chapter shows a series of rapid scan EPR done with LiPC, ending with proof-of-concept a rapid scan on the radicals, not degassed sample of DPPH dis-

solved in toluene, which was the main task of my Ph.D.

Perspectives: Despite the fast development of magnetic resonance field, I hope that this thesis will remain up-to-date and provide useful information to anyone who will read it. A HF-EPR spectrometer is high complexity and not easy to build and operate. In my work, I pointed out that any spectrometer using a sample holder without a resonator (non-resonant sample holder) has a wide range of applications, which can be reached by designing appropriate sample holders. There are plenty of problems that still need to be solved in the development of rapid scan EPR. How to make stable broad sweep, background treatment for broad signals, measurement of T_1 time and more. Still, even little progress of EPR spectroscopy can bring new information in many scientific disciplines.

We prove that our spectrometer can perform rapid scan on the samples with a relatively narrow signal like DPPH or LiPC. Next progress in frequency domain rapid scan will open the door of the new broad use of EPR. Thanks to broader operating range (tens of GHz) and the absence of a dead time, rapid scan can theoretically measure extremely short T_2 (ns) relaxation times at any frequency within the spectrometer's frequency range. Therefore, as the sensitivity of detectors and spectrometer goes higher together with more powerful and faster m.w. sources, we can expect measuring T_2 and T_1 time on samples with broad line width such as transition metals complexes, SMM/SIM quantum bits, and others. Moreover, our successful experiment on DPPH will open the door for DNP radical study in the near future. The development of rapid scan on radicals dissolved in liquid will continue in our EXPRO GAČR project (Implementation of Frequency Rapid Scan Electron Spin Resonance Spectroscopy into Nuclear Magnetic Resonance Systems), which recently received financial support. The successful study of such radicals in high magnetic fields is necessary in understanding and optimizing the nuclear polarization efficiency and developing spin polarization agents. Thus, significantly improve the NMR spectroscopy.

Author publications and other outputs:

- **PUBLICATION**

2022 Sample Holders for Sub-THz Electron Spin Resonance Spectroscopy, IEEE Transactions on Instrumentation and Measurement, *A. Sojka, et al. (Submitted)*

2021 Rapid scan ESR: a versatile tool for the spin relaxation studies at (sub)THz frequencies, Applied Physics Letters, *O. Laguta, A. Sojka, et al. (Accepted)*

2021 Simulation of nitrogen nuclear spin magnetization of liquid solved nitroxides, Phys Chem Chem Phys, *Andriy Marko, A. Sojka, et al.*

2020 High-frequency EPR: current state and perspectives, RSC Electron Paramagnetic Resonance: Volume 27, 214 – 252. *A. Sojka, et al.*

2020 Deposition of Tetracoordinate Co(II) Complex with Chalcone Ligands on Graphene, Molecules, 25, 5021. *J. Hrubý, Š. Vavrečková, L. Masaryk, A. Sojka, et al.*

- **CONFERENCES/SUMMER SCHOOLS**

09/2021 PhD Retreat 2021 (online), Czech Republic

04/2021 (Poster) RSC ESR 2021 (online), Scotland

11/2019 (Poster) 8th European Federation of EPR School, Czech Republic, **Member of Organizers**

09/2019 (Poster) XIth EFEPR Conference, Bratislava, Slovakia

07/2019 (Poster) 60st Rocky Mountain Conference on Magnetic Resonance, Denver (USA)

06/2019 (Talk) 2nd conference of the Magneto-Optical and THz Spec. Research Group, Poland

10/2018 (Poster) PETER Summer School, Brno, Czech Republic

09/2018 (Talk) V International School for Young Scientists, Russia

07/2018 (Poster) ICN+T, Brno, Czech Republic. **Member of organizers**

04/2018 (Poster) CEITEC PhD & Postdoc Retreat, Telč, Czech Republic, **Winner of Poster price**

07/2017 16th IUVSTA International Summer School on Phys. at Nanoscale, Czech Republic

03/2016 (Poster) sIMMposium Symposium of the Institute Molecules and Materials, Netherlands

02/2015 (Poster) Brno University of Technology students poster session, Brno, Czech Republic

- **INTERNSHIPS**

2019 CEITEC Mobility, Santa Barbara University, USA, group of prof. Mark Sherwin.

2017 COST+, University of Stuttgart, Germany, group of Prof. Dr. Joris van Slageren.

2016 Erasmus+ program, Radboud University, Netherlands, Group of Prof. Alex Khajetoorians.

- **EDUCATION**

2015 – 2017 Master's study at Brno University of Technology, Institute of Physical Engineering and Nanotechnology (Czech Republic) under the supervision of Ing. Michal Pavera Ph.D. **Master's Thesis:** *Low-temperature scanning tunneling microscopy*

2012 – 2015 Bachelor's study at Brno University of Technology, Institute of Physical Engineering and Nanotechnology (Czech Republic) under the supervision of Ing. Michal Pavera Ph.D. **Bachelor's Thesis**: *Assembling and testing of the STM microscope*

2008 – 2012 Grammar school, Gymnázium Rožnov pod Radhoštem, Czech Republic

- **CURRENT POSITION**

2017 – Present Ph.D.'s study at the Central European Institute of Technology (CEITEC), Brno (Czech Republic) under the supervision of Dr. Ing. Petr Neugebauer. **Topic:** *Development of a Terahertz Magnetic Resonance Spectrometer for Electron Spin Dynamics Investigations*

- **PREVIOUS POSITIONS**

2020 R&D Designer, company Activair s.r.o., Brno, Czech Republic. *Development of a high-vacuum chamber for the study of welds.*

2016 – 2017 R&D System engineer, company FEI Thermo Fisher Scientific CZ s.r.o., Brno, Czech Republic. *Development of high-end scanning electron microscopes.*

2015	Lab worker, Institute of Physical Engineering and Nanotechnology, Brno, Czech Republic. *Development of the STM cooling system.*
2014 – 2015	Engineer, Aura engineering Hranice spol. s.r.o., Hranice Czech Republic, D*esing of single-purpose machines*
2008 – 2013	Electrician, Company Sojka, Hluzov, Czech Republic.
Others:	Summer Camp supervisor, *Group leader and game creator for kids 6 – 15 years*

- **SUPERVISION STUDENTS (3 bachelors, 1 high school)**

Tomáš Fargaš	Bachelor, 2021 Topic: *Rapid scans EPR on DNP relevant radicals*
Bc. Adam Lagiň	Bachelor, 2020, Topic: *Design of non-resonant sample holders,*
Bc. Andrej Gabriš	Bachelor, 2020, Topic: *Design of single-crystal sample holder for high-frequency electron paramagnetic resonance,*
Adam Vondráček	High school student, 2019-2020 Topic: *Artificial neural network in EPR*

Best presentation – 2019 and 2020 (CEITEC Student Talent)

- **CO-SUPERVISION STUDENTS (2 Masters)**

Ing. Tomáš Láznička	Master, 2020, Topic: *Design vacuum transfer chamber for High Field – EPR*
Ing. Tomáš Martínek	Master, 2018, Topic: *Design of a Non-Resonant General Purpose Sample Holder*

for Terahertz EPR Spectroscopy

- **TEACHING ACTIVITIES**

2020 – Present: EPR practical lab courses, 3rd- year students of Institute of Physical Engineering, BUT.
2018 – 2020:   Physics lab courses, 1st- year student of Institute of Mechanical engineering, BUT.
2018 – 2020:   Physics lab courses, 2st- year student of Institute of Mechanical engineering, BUT.

- **ORGANIZATION OF SCIENTIFIC MEETINGS**

2019	8th European Federation of EPR School
2018	ICN+T , Brno, Czech Republic
Others:	Activities for the popularization of science: *Researchers´ Night (2018 and 2019), VUT Junior (2020), VUT 120 anniversary (2019), excursion for public on CEITEC*

- **MEMBERSHIPS OF SCIENTIFIC SOCIETIES**

2019 – Present: Member of International EPR (ESR) Society

- **AWARDS**

2020	Travel Stipendium for Rocky Mountain Conference on Magnetic Resonance
2019-2020	Adam Vondracek, Best presentation – 2019 and 2020 (young CEITEC scientist)
2018	Winner of Poster price, CEITEC PhD & Postdoc Retreat, Telč, Czech Republic
2017	FEI Thermo Fisher Scientific CZ s.r.o. award for job achievements

- **INVOLVEMENT IN PROJECTS**

2020 - present	CZ-USA Inter-Excellence Topic: *Spectroscopy of single molecular magnets using graphene bolometers*
2019	Internal CEITEC project for creating a new education course, Topic: *Laboratory courses in Electron Paramagnetic Resonance*
2017	COST+, Topic: *Influence of Substrates on Magnetic Properties of Deposited Single-Molecule Magnets*
2017 - present	ERC, Topic: *THz Frequency Rapid Scan – Electron Spin Resonance spectroscopy for spin dynamics investigations of bulk and surface materials*

Bibliography

[1] T. Martinek. Design of a non-resonant general purpose sample holder for terahertz electron paramagnetic resonance spectroscopy, Master's thesis, 2018.

[2] A. Lagiň. Design of non-resonant sample holders, Bachelor's thesis, 2020.

[3] A. Gabriš. Návrh držáku vzorku pro studium orientovaných krystalů pomocí vysokofrekvenční paramagnetické resonance, Bachelor's thesis, 2020.

[4] T. Fargač. Rapid scan epr spectroscopy on dnp relevant radicals, Bachelor's thesis, 2021.

[5] T. Láznička. Design of mobile vacuum chamber for loading samples into high- -frequency electron paramagnetic resonance spectrometer, Master's thesis, 2020.

[6] A. J. Weil and J. Bolton. In *Electron Paramagnetic Resonance: Elementary Theory and Practical Applications.* 2nd edition, 2006.

[7] E. K. Zavoisky. Paramagnetic relaxation of liquid solutions for perpendicular fields. *Zhur. Eksperiment. i Theoret. Fiz.*, 15(12):344–350, jul 1944.

[8] L. Kevan and M. K. Bowman. *Modern pulsed and continuous-wave electron spin resonance.* 1990.

[9] O. Duss, M. Yulikov, G. Jeschke, and F. Allain. EPR-aided approach for solution structure determination of large RNAs or protein-RNA complexes. *Nature Communications*, 5, may 2014.

[10] A. Mullen, J. Hall, J. Diegel, I. Hassan, A. Fey, and F. MacMillan. Membrane transporters studied by EPR spectroscopy: Structure determination and elucidation of functional dynamics. *Biochemical Society Transactions*, 44(3):905–915, jun 2016.

[11] P. Consentius, U. Gohlke, B. Loll, C. Alings, U. Heinemann, M. C Wahl, and T. Risse. Combining EPR spectroscopy and X-ray crystallography to elucidate the structure and dynamics of conformationally constrained spin labels in T4 lysozyme single crystals. *Phys. Chem. Chem. Phys.*, 19(31):20723–20734, aug 2017.

[12] M. Carmen Giménez-López, F. Moro, A. La Torre, C. J Gómez-García, P. D Brown, J. Van Slageren, and A. N Khlobystov. Encapsulation of

single-molecule magnets in carbon nanotubes. *Nature Communications*, 2, 2011.

[13] A. Kajiwara and K. Matyjaszewski. EPR and kinetic studies of atom transfer radical polymerization of (meth)acrylates. *Polymer Journal*, 31(1):70–75, 1999.

[14] F. Liu, D. S. Krylov, L. Spree, S. M. Avdoshenko, N. A. Samoylova, M. Rosenkranz, A. Kostanyan, T. Greber, A. U.B. Wolter, B. Büchner, and A. A. Popov. Single molecule magnet with an unpaired electron trapped between two lanthanide ions inside a fullerene. *Nature Communications*, 8, jul 2017.

[15] N. Fujita, D. Matsumoto, Y. Sakurai, K. Kawahara, H. Ago, T. Takenobu, and K. Marumoto. Direct observation of electrically induced Pauli paramagnetism in single-layer graphene using ESR spectroscopy. *Scientific Reports*, 6, oct 2016.

[16] K. Sato, S. Nakazawa, S. Nishida, R. D. Rahimi, T. Yoshino, Y. Morita, K. Toyota, D. Shiomi, M. Kitagawa, and T. Takui. Novel Applications of ESR/EPR: Quantum Computing/Quantum Information Processing. 2012.

[17] A. S. Thankamony, J. J. Wittmann, M. Kaushik, and B. Corzilius. Dynamic nuclear polarization for sensitivity enhancement in modern solid-state nmr. *Progress in Nuclear Magnetic Resonance Spectroscopy*, 102-103:120–195, 2017.

[18] Q. Ni, E. Daviso, T. Can, E. Markhasin, S. K. Jawla, T. M. Swager, R. J. Temkin, J. Herzfeld, and R. G. Griffin. High frequency dynamic nuclear polarization. *Accounts of Chemical Research*, 46(9):1933–1941, sep 2013.

[19] M. N. Leuenberger and D. Loss. Quantum computing in molecular magnets. *Nature*, 410(6830):789–793, apr 2001.

[20] S. Realista, A. J. Fitzpatrick, G. Santos, L. P. Ferreira, S. Barroso, L. C. J. Pereira, N. A. G. Bandeira, P. Neugebauer, J. Hrubý, G. G. Morgan, J. van Slageren, M. J. Calhorda, and P. N. Martinho. A mn(iii) single ion magnet with tridentate schiff-base ligands. *Dalton Trans.*, 45:12301–12307, 2016.

[21] I. Nemec, R. Herchel, M. Kern, P. Neugebauer, J. Van Slageren, and Z. Trávníček. Magnetic anisotropy and field-induced slow relaxation of magnetization in tetracoordinate coii compound [co(ch3-im)2cl2]. *Materials*, 10(3), 2017.

[22] Y.-Y. Zhu, T.-T. Yin, S.-D. Jiang, A.-L. Barra, W. Wernsdorfer, P. Neugebauer, R. Marx, M. Dörfel, B.-W. Wang, Z.-Q. Wu, J. van Slageren, and S. Gao. The solvent effect in an axially symmetric feiii4 single-molecule magnet. *Chem. Commun.*, 50:15090–15093, 2014.

[23] T. K. Prasad, G. Poneti, L. Sorace, M. J. Rodriguez-Douton, A.-L. Barra, P. Neugebauer, L. Costantino, R. Sessoli, and A. Cornia. Magnetic and optical bistability in tetrairon(iii) single molecule magnets functionalized with azobenzene groups. *Dalton Trans.*, 41:8368–8378, 2012.

[24] G. M. Smith, P. A. S. Cruickshank, D. R. Bolton, and D. A. Robertson. High-field pulse epr instrumentation. In *Electron Paramagnetic Resonance: Volume 21*, volume 21, pages 216–233. The Royal Society of Chemistry, 2008.

[25] J. R. Biller, D. G. Mitchell, M. Tseytlin, H. Elajaili, G. A. Rinard, R. W. Quine, S. S. Eaton, and G. R. Eaton. Rapid scan electron paramagnetic resonance opens new avenues for imaging physiologically important parameters in vivo. *Journal of Visualized Experiments*, 2016(115), sep 2016.

[26] S. S. Eaton, Y. Shi, L. Woodcock, L. A. Buchanan, J. McPeak, R. W. Quine, G. A. Rinard, B. Epel, H. J. Halpern, and G. R. Eaton. Rapid-scan EPR imaging. *Journal of Magnetic Resonance*, 280:140–148, jul 2017.

[27] D. G. Mitchell, G. M. Rosen, M. Tseitlin, B. Symmes, S. S. Eaton, and G. R. Eaton. Use of rapid-scan epr to improve detection sensitivity for spin-trapped radicals. *Biophysical journal*, 105(2):338–342, 2013.

[28] O. Laguta, M. Tuček, J. van Slageren, and P. Neugebauer. Multi-frequency rapid-scan HFEPR. *Journal of Magnetic Resonance*, 296:138–142, nov 2018.

[29] A. Marko, A. Sojka, O. Laguta, and P. Neugebauer. Simulation of nitrogen nuclear spin magnetization of liquid solved nitroxides. *Phys. Chem. Chem. Phys.*, 23(32):17310–17322, aug 2021.

[30] P. Neugebauer, J.-G. Krummenacker, V.-P. Denysenkov, Ch. Helmling, C. Luchinat, G. Parigi, and T.-F. Prisner. High-field liquid state NMR hyperpolarization: a combined DNP/NMRD approach. *Phys. Chem. Chem. Phys.*, 16(35):18781–18787, aug 2014.

[31] P. Neugebauer, J. G. Krummenacker, V. P. Denysenkov, G. Parigi, C. Luchinat, and T. F. Prisner. Liquid state dnp of water at 9.2 t: an experimental access to saturation. *Phys. Chem. Chem. Phys.*, 15:6049–6056, 2013.

[32] S.-E. Küçük, P. Neugebauer, T.-F. Prisner, and D. Sezer. Molecular simulations for dynamic nuclear polarization in liquids: a case study of tempol in acetone and dmso. *Phys. Chem. Chem. Phys.*, 17:6618–6628, 2015.

[33] P. Neugebauer, D. Bloos, R. Marx, P. Lutz, M. Kern, D. Aguilà, J. Vaverka, O. Laguta, C. Dietrich, R. Clérac, and J. Van Slageren. Ultra-broadband EPR spectroscopy in field and frequency domains. *Phys. Chem. Chem. Phys.*, 20(22):15528–15534, 2018.

[34] W. Gerlach and O. Stern. Das magnetische Moment des Silberatoms. *Zeitschrift für Physik 1922 9:1*, 9(1):353–355, dec 1922.

[35] I. I. Rabi, J. R. Zacharias, S. Millman, and P. Kusch. A new method of measuring nuclear magnetic moment. *Phys. Rev.*, 53:318–318, Feb 1938.

[36] G. R. Eaton, Sandra S. E., and Kev M. S. Foundations of modern epr. 1998.

[37] J. W. Emsley and J. Feeney. Forty years of Progress in Nuclear Magnetic Resonance Spectroscopy. 2007.

[38] G. A. Morris. Varian Associates and the birth of commercial NMR spectroscopy. *Journal of Magnetic Resonance*, 306:12–16, sep 2019.

[39] Ya. S. Lebedev. *Magnetic Resonance and Related Phenomena*. Springer, 1978.

[40] O. Y. Grinberg and L. J. Berliner, editors. *Very High Frequency (VHF) ESR/EPR*, volume 22 of *Biological Magnetic Resonance*. 2004.

[41] Ya. S. Lebedev. Submillimeter epr spectroscopy of free radicals. In *Dokl. Akad. Nauk*, 1976.

[42] R. R. Ernst and W. A. Anderson. Application of fourier transform spectroscopy to magnetic resonance. *Review of Scientific Instruments*, 37(1):93–102, 1966.

[43] R. R. Ernst. Nuclear magnetic resonance fourier transform spectroscopy (nobel lecture). *Angewandte Chemie International Edition in English*, 31(7):805–823, 1992.

[44] T. C. Farra. Pulsed and fourier transform nmr spectroscopy. *Analytical Chemistry*, 42(2):109A–112A, 1970.

[45] A. D. Bain and J. S. Martin. Ft nmr of nonequilibrium states of complex spin systems. i. a lionville space description. *Journal of Magnetic Resonance (1969)*, 29(1):125–135, 1978.

[46] U. Eichhoff and P. Höfer. 75 Years of EPR. EPR Milestones in 60 Years Bruker History. *Applied Magnetic Resonance*, 51:1723–1737, 2020.

[47] R. T. Weber, J. M. Disselhorst, L. J. Prevo, J. Schmidt, and W. T. H. Wenckebach. Electron spin-echo spectroscopy at 95 GHz. *Journal of Magnetic Resonance (1969)*, 81(1):129–144, jan 1989.

[48] F. Muller, M. A. Hopkins, N. Coron, M. Grynberg, L. C. Brunel, and G. Martinez. A high magnetic field EPR spectrometer. *Review of Scientific Instruments*, 60(12):3681, sep 1989.

[49] C. Kutter, H. P. Moll, J. Van Tol, H. Zuckermann, J. C. Maan, and P. Wyder. Electron-spin echoes at 604 GHz using far infrared lasers. *Phys. Rev. Lett.*, 74(15):2925–2928, 1995.

[50] W. B. Lynch, K. A. Earle, and J. H. Freed. 1-mm wave esr spectrometer. *Review of scientific instruments*, 59(8):1345–1351, 1988.

[51] K. Möbius and A. Savitsky. *High-Field EPR Spectroscopy on Proteins and their Model Systems.* Royal Society of Chemistry, dec 2008.

[52] A. W. Overhauser. Polarization of Nuclei in Metals. *Phys. Rev.*, 92(2):411, oct 1953.

[53] R. G. Griffin and T. F. Prisner. High field dynamic nuclear polarization—the renaissance. *Phys. Chem. Chem. Phys.*, 12(22):5737–5740, may 2010.

[54] H. Ohta, S. Okubo, E. Ohmichi, T. Sakurai, W. M. Zhang, and T. Shimokawa. Developments of multi-extreme high field ESR in Kobe. In *Journal of Low Temperature Physics*, volume 170, pages 511–519, mar 2013.

[55] Ch. Caspers, P. F. da Silva, M. Soundararajan, M. A. Haider, and J.-P. Ansermet. Field and frequency modulated sub-THz electron spin resonance spectrometer. *APL Photonics*, 1(2):026101, may 2016.

[56] N. Bloembergen, E. M. Purcell, and R. V. Pound. Relaxation effects in nuclear magnetic resonance absorption. *Phys. Rev.*, 73:679–712, Apr 1948.

[57] B. A. Jacobsohn and R. K. Wangsness. Shapes of nuclear induction signals. *Phys. Rev.*, 73:942–946, May 1948.

[58] R. K. Gupta, J. A. Ferretti, and E. D. Becker. Rapid scan fourier transform nmr spectroscopy. *Journal of Magnetic Resonance (1969)*, 13(3):275–290, 1974.

[59] J. Dadok and R. F. Sprecher. Correlation nnw spectroscopy. *Journal of Magnetic Resonance (1969)*, 13(2):243–248, 1974.

[60] D. Shaw. *Fourier transform N.M.R. spectroscopy.* 1976.

[61] A. M. Portis. Rapid passage effects in electron spin resonance. *Phys. Rev.*, 100:1219–1221, Nov 1955.

[62] G. M. Smith, J. C. G. Lesurf, R. H. Mitchell, and P. C. Riedi. Quasi-optical cw mm-wave electron spin resonance spectrometer. *Review of Scientific Instruments*, 69(11):3924, nov 1998.

[63] J. P. Joshi, J. R. Ballard, G. A. Rinard, R. W. Quine, S. S. Eaton, and G. R. Eaton. Rapid-scan EPR with triangular scans and fourier deconvolution to recover the slow-scan spectrum. *Journal of Magnetic Resonance*, 175(1):44–51, jul 2005.

[64] J. W. Stoner, D. Szymanski, S. S. Eaton, R. W. Quine, G. A. Rinard, and G. R. Eaton. Direct-detected rapid-scan epr at 250mhz. *Journal of Magnetic Resonance*, 170(1):127–135, 2004.

[65] D. G. Mitchell, R. W. Quine, M. Tseitlin, V. Meyer, S. S. Eaton, and G. R. Eaton. Comparison of continuous wave, spin echo, and rapid scan EPR of irradiated fused quartz. *Radiation Measurements*, 46(9):993–996, sep 2011.

[66] Rapid Scan EPR|Bruker, https://www.bruker.com/en/products-and-solutions/mr/epr-instruments/rapidscan.html, 2021-11-02.

[67] J. R. Biller and J. E. McPeak. EPR Everywhere. *Applied Magnetic Resonance 2021 52:8*, 52(8):1113–1139, jan 2021.

[68] Webpage - nmr v brne | tesla bs477 www.ebyte.it/library/hist/nmr_tesla_cs.html, 2022-15-03.

[69] A. Abragam and B. Bleaney. *Electron paramagnetic resonance of transition ions.* Oxford : Clarendon press, Oxford, first edition, 1970.

[70] P. Bertrand. *Electron Paramagnetic Resonance Spectroscopy.* Springer International Publishing, Cham, 2020.

[71] D. Hanneke, S. Fogwell, and G. Gabrielse. New measurement of the electron magnetic moment and the fine structure constant. *Phys. Rev. Lett.*, 100:120801, Mar 2008.

[72] P. Marra. *Theoretical approach to direct resonant inelastic x-ray scattering on magnets and superconductors.* PhD thesis, 05 2016.

[73] M. Rohrer, O. Brügmann, B. Kinzer, and Thomas F. Prisner. High-field/high-frequency EPR spectrometer operating in pulsed and continuous-wave mode at 180 GHz. *Applied Magnetic Resonance 2001 21:3*, 21(3):257–274, 2001.

[74] A. Schweiger and G. Jeschke. Principles of Pulse Electron Paramagnetic Resonance. Oxford University Press. page 578, 2001.

[75] D. Gatteschi, R. Sessoli, and J. Villain. *Molecular Nanomagnets*, volume 9780198567530. Oxford University Press, sep 2007.

[76] J. Hrubỳ, S. Vavrečková, L. Masaryk, A. Sojka, G. J. Navarro, M. Bartoš, R. Herchel, J. Moncol, I. Nemec, and P. Neugebauer. Deposition of tetracoordinate co (ii) complex with chalcone ligands on graphene. *Molecules*, 25(21):5021, 2020.

[77] A. Sojka, M. Šedivý, O. Laguta, A. Marko, V. T. Santana, and P. Neugebauer. High-frequency EPR: Current state and perspectives. *Electron Paramagnetic Resonance*, 27:214–252, nov 2021.

[78] I. Park, Ch. Lee, J. Park, S. Kim, and S. Jeong. Performance of the fast-ramping high temperature superconducting magnet system for an active magnetic regenerator. *IEEE Transactions on Applied Superconductivity*, 27(4):1–5, 2017.

[79] A.L. Barra. High- and multi-frequency epr study of mn12: A new technique for studying new objects. *Inorganica Chimica Acta*, 361(12):3564–3569, 2008. Protagonists in Chemistry: Dante Gatteschi (Part I).

[80] S. Mitsudo, Aripin, T. Shirai, T. Matsuda, T. Kanemaki, and T. Idehara. High power, frequency tunable, submillimeter wave ESR device using a gyrotron as a radiation source. *International Journal of Infrared and Millimeter Waves*, 21(4):661–676, 2000.

[81] H. Hirata, T. Walczak, and H.-M. Swartz. Electronically Tunable Surface-Coil-Type Resonator for L-Band EPR Spectroscopy. *Journal of Magnetic Resonance*, 142(1):159–167, 2000.

[82] P. Neugebauer. Development of Heterodyne High Field / High Frequency Electron Paramagnetic Resonance Spectrometer at 285 GHz. Technical report, Dissertation's Thesis, 2010.

[83] K. Möbius, A. Savitsky, A. Schnegg, M. Plato, and M. Fuchs. High-field epr spectroscopy applied to biological systems: characterization of molecular switches for electron and ion transfer. *Phys. Chem. Chem. Phys.*, 7:19–42, 2005.

[84] R. Maurice, C. de Graaf, and N. Guihéry. Theoretical determination of spin hamiltonians with isotropic and anisotropic magnetic interactions in transition metal and lanthanide complexes. *Phys. Chem. Chem. Phys.*, 15:18784–18804, 2013.

[85] X. Feng, J. Liu, T. D. Harris, S. Hill, and J. R Long. Slow magnetic relaxation induced by a large transverse zero-field splitting in a mniireiv (cn) 2 single-chain magnet. *Journal of the American Chemical Society*, 134(17):7521–7529, 2012.

[86] J. M. Frost, K. L.M. Harriman, and M. Murugesu. The rise of 3-d single-ion magnets in molecular magnetism: Towards materials from molecules? , apr 2016.

[87] T. Lis. Preparation, structure, and magnetic properties of a dodecanuclear mixed-valence manganese carboxylate. *Acta Crystallographica Section B*, 36(9):2042–2046, Sep 1980.

[88] R. Sessoli, D. Gatteschi, A. Caneschi, and M. A. Novak. Magnetic bistability in a metal-ion cluster. *Nature 1993 365:6442*, 365(6442):141–143, 1993.

[89] J. Freed. On the Theory of Spin Relaxation of Gas Molecules: The Strong-Collision Limit. *The Journal of Chemical Physics*, 41(1):7, jul 2004.

[90] S. T. Liddle and J. van Slageren. Improving f-element single molecule magnets. *Chemical Society Reviews*, 44(19):6655–6669, 2015.

[91] R. L. Cummerow and D. Halliday. Paramagnetic losses in two manganous salts. *Phys. Rev.*, 70:433–433, Sep 1946.

[92] M. H. Levitt. *Spin dynamics: basics of nuclear magnetic resonance.* 2013.

[93] A. A. Manenkov, R. Orbach, and Ralph P. Hudson. Spin-Lattice Relaxation in Ionic Solids. *Physics Today*, 20(7):88, jan 1967.

[94] A. Lund, E. Sagstuen, A. Sanderud, and J. Maruani. Relaxation-Time Determination from Continuous-Microwave Saturation of EPR Spectra. *Radiation Research*, 172(6):753 – 760, 2009.

[95] C. Griesinger, M. Bennati, H. M. Vieth, C. Luchinat, G. Parigi, P. Höfer, F. Engelke, S. J. Glaser, V. Denysenkov, and T. F. Prisner. Dynamic nuclear polarization at high magnetic fields in liquids, 2012.

[96] E. Moreno Pineda, N. F. Chilton, R. Marx, M. Dörfel, D. O. Sells, P. Neugebauer, S. D. Jiang, D. Collison, J. Van Slageren, E. J. McInnes, and R. P. Winpenny. Direct measurement of dysprosium(III)··· dysprosium(III) interactions in a single-molecule magnet. *Nature Communications*, 5, oct 2014.

[97] J. Du, X. Rong, N. Zhao, Y. Wang, J. Yang, and R. B. Liu. Preserving electron spin coherence in solids by optimal dynamical decoupling. *Nature*, 461(7268):1265–1268, oct 2009.

[98] M. Nechtschein, F. Genoud, C. Menardo, K. Mizoguchi, J. P. Travers, and B. Villeret. On the nature of the conducting state of polyaniline. *Synthetic Metals*, 29(1):211–218, mar 1989.

[99] T. Gaebel, M. Domhan, I. Popa, C. Wittmann, P. Neumann, F. Jelezko, J. R. Rabeau, N. Stavrias, A. D. Greentree, S. Prawer, J. Meijer, J. Twamley, P. R. Hemmer, and J. Wrachtrup. Room-temperature coherent coupling of single spins in diamond. *Nature Physics*, 2(6):408–413, 2006.

[100] D. E. Kaplan, M. E. Browne, and J. A. Cowen. Pulsed X-band EPR spectrometer. *Review of Scientific Instruments*, 32(11):1182–1186, 1961.

[101] I. Tkach, K. Halbmair, C. Höbartner, and M. Bennati. High-frequency 263 GHz PELDOR. *Applied Magnetic Resonance*, 45(10):969–979, oct 2014.

[102] S. Takahashi, L. C. Brunel, D. T. Edwards, J. Van Tol, G. Ramian, S. Han, and M. S. Sherwin. Pulsed electron paramagnetic resonance spectroscopy powered by a free-electron laser. *Nature*, 489(7416):409–413, sep 2012.

[103] J. S. Hyde, R. A. Strangeway, T. G. Camenisch, J. J. Ratke, and W. Froncisz. W-band frequency-swept EPR. *Journal of Magnetic Resonance*, 205(1):93–101, jul 2010.

[104] E. L. Hahn. Spin echoes. *Phys. Rev.*, 80(4):580, 1950.

[105] T. Prisner, M. Rohrer, and F. MacMillan. Pulsed epr spectroscopy: biological applications. *Annual review of physical chemistry*, 52(1):279–313, 2001.

[106] E. L. Hahn. Nuclear induction due to free larmor precession. *Phys. Rev.*, 77(2):297, 1950.

[107] H. Cho, S. Pfenninger, C. Gemperle, A. Schweiger, and R. R. Ernst. Zero deadtime pulsed esr by remote echo detection. *Chemical physics letters*, 160(4):391–395, 1989.

[108] P. A. Cruickshank, D. R. Bolton, D. A. Robertson, R. I. Hunter, R. J. Wylde, and G. M. Smith. A kilowatt pulsed 94 ghz electron paramagnetic resonance spectrometer with high concentration sensitivity, high instantaneous bandwidth, and low dead time. *Review of Scientific Instruments*, 80(10):103102, 2009.

[109] J. M. Franck, R. P. Barnes, T. J. Keller, T. Kaufmann, and S. Han. Active cancellation – a means to zero dead-time pulse epr. *Journal of Magnetic Resonance*, 261:199–204, 2015.

[110] A. Marko O. Laguta, A. Sojka and P. Neugebauer. Rapid scan esr: a versatile tool for the spin relaxation studies at (sub)thz frequencies. *accepeted in Applied Physics Letters*, 2022.

[111] M. Tuček. Frequency-swept rapid-scan epr on organic radicals, 2018.

[112] M. Tseitlin, G. A. Rinard, R. W. Quine, S. S. Eaton, and G. R. Eaton. Deconvolution of sinusoidal rapid epr scans. *Journal of Magnetic Resonance*, 208(2):279–283, 2011.

[113] M. Tseitlin. General solution for rapid scan epr deconvolution problem. *Journal of Magnetic Resonance*, 318:106801, 2020.

[114] G. Annino, H. Moons, M. Fittipaldi, S. Van Doorslaer, and E. Goovaerts. High-Field Pulsed ENDOR with Intra-cavity Radiofrequency Coil. *Applied Magnetic Resonance*, 51:1433–1449, 2020.

[115] C. P. Poole. Electron spin resonance: a comprehensive treatise on experimental techniques. 1996.

[116] E. J. Reijerse, P. J. Van Dam, A. A. K. Klaassen, W. R. Hagen, P. J. M. Van Bentum, and G. M. Smith. Concepts in high-frequency EPR - Applications

to bio-inorganic systems. *Applied Magnetic Resonance*, 14(2-3):153–167, 1998.

[117] E. Ohmichi, Y. Shoji, H. Takahashi, and H. Ohta. Frequency-domain electron spin resonance spectroscopy using continuously frequency-tunable terahertz photomixers. *Applied Physics Letters*, 119(16):162404, oct 2021.

[118] V. S. Bajaj, C. T. Farrar, M. K. Hornstein, I. Mastovsky, J. Vieregg, J. Bryant, B. Eléna, K. E. Kreischer, R. J. Temkin, and R. G. Griffin. Dynamic nuclear polarization at 9T using a novel 250GHz gyrotron microwave source. *Journal of Magnetic Resonance*, 160(2):85–90, feb 2003.

[119] V. F. Tarasov and G. S. Shakurov. Submillimetre EPR spectrometer. *Applied Magnetic Resonance*, 2(3):571–576, sep 1991.

[120] L. St Marie, A. El Fatimy, J. Hrubý, I. Nemec, J. Hunt, R. Myers-Ward, D K. Gaskill, M. Kruskopf, Y. Yang, R. Elmquist, R. Marx, J. v. Slageren, P. Neugebauer, and P. Barbara. Nanostructured graphene for nanoscale electron paramagnetic resonance spectroscopy. *Journal of Physics: Materials*, 3(1):014013, jan 2020.

[121] J. Nehrkorn, K. Holldack, R. Bittl, and A. Schnegg. Recent progress in synchrotron-based frequency-domain fourier-transform thz-epr. *Journal of Magnetic Resonance*, 280:10–19, 2017.

[122] P. F. Goldsmith. *Quasioptical Systems: Gaussian Beam Quasioptical Propogation and Applications (IEEE Press Series on RF and Microwave Technology)*. 1998.

[123] G. M. Smith, P. A. S. Cruickshank, D. R. Bolton, and D. A. Robertson. High-field pulse epr instrumentation. In *Electron Paramagnetic Resonance: Volume 21*, volume 21, pages 216–233. The Royal Society of Chemistry, 2008.

[124] M. R. Fuchs. A high-field / high-frequency electron paramagnetic resonance spectrometer (360 ghz / 14 t)., Dissertation's thesis, 1999.

[125] R. I. Hunter, D. A. Robertson, P. Goy, and G. M. Smith. Design of high-performance millimeter wave and sub-millimeter wave quasi-optical isolators and circulators. *IEEE Transactions on Microwave Theory and Techniques*, 55(5):890–897, may 2007.

[126] J. F. Hanlon. *A user's guide to vacuum technology.* John Wiley & Sons, 2005.

[127] A. Sojka, M. Šedivý, A. Lagiň, A. Gabriš, T. Láznička, V. T. Santana, O. Laguta, and P. Neugebauer. Sample holders for sub-thz electron spin resonance spectroscopy. *IEEE Transactions on Instrumentation and Measurement*, submitted 1/2022.

[128] J. M. Gaitonde and M. V. Lowson. Low-temperature thermal expansion of peek, hta and some of their composites reinforced with carbon fibres. *Composites Science and Technology*, 40(1):69–85, 1991.

[129] L. Song, Z. Liu, P. Kaur, J. M. Esquiaqui, R. I. Hunter, S. Hill, G. M. Smith, and G. E. Fanucci. Toward increased concentration sensitivity for continuous wave epr investigations of spin-labeled biological macromolecules at high fields. *Journal of Magnetic Resonance*, 265:188–196, 2016.

[130] E. N. Yuri, A. Gopinath, and D. D. Thomas. Aqueous sample in an epr cavity: sensitivity considerations. *Journal of Magnetic Resonance*, 167(1):138–146, 2004.

[131] F. El Hallak, P. Neugebauer, A.-L. Barra, J. Van Slageren, M. Dressel, and A. Cornia. Torque-detected ESR of a tetrairon(III) single molecule magnet. *Journal of Magnetic Resonance*, 223:55–60, oct 2012.

[132] R. P. Sartoris, V. T. Santana, Eleonora F., R. F. Baggio, O. R. Nascimento, and . Calvo. Exchange couplings and quantum phases in two dissimilar arrays of similar copper dinuclear units. *Dalton Transactions*, 49(16):5228–5240, apr 2020.

[133] T. Yamane, K. Sugisaki, T. Nakagawa, H. Matsuoka, T. Nishio, S. Kinjyo, N. Mori, S. Yokoyama, C. Kawashima, N. Yokokura, K. Sato, Y. Kanzaki, D. Shiomi, K. Toyota, D. H. Dolphin, W.-C. Lin, Ch. A. McDowell, M. Tadokoro, and T. Takui. Analyses of sizable ZFS and magnetic tensors of high spin metallocomplexes. *Phys. Chem. Chem. Phys.*, 19(36):24769–24791, sep 2017.

[134] M. Simenas, A. Kultaeva, S. Balciunas, M. Trzebiatowska, D. Klose, G. Jeschke, M. Maczka, J. Banys, and A. Poppl. Single Crystal Electron Paramagnetic Resonance of Dimethylammonium and Ammonium Hybrid Formate Frameworks: Influence of External Electric Field. *Journal of Physical Chemistry C*, 121(30):16533–16540, aug 2017.

[135] V. T. Santana, B. N. Cunha, A. M. Plutín, R. G. Silveira, E. E. Castellano, A. A. Batista, R. Calvo, and O. R. Nascimento. Magnetic-field-tuned phase

transition of a molecular material from the isolated-spin to the coupled-spin regime. *Phys. Chem. Chem. Phys.*, 21:4394–4407, 2019.

[136] D. Bloos, J. Kunc, L. Kaeswurm, R. L. Myers-Ward, K. Daniels, M. Dejarld, A. Nath, J. Van Slageren, D. K. Gaskill, and P. Neugebauer. Contactless millimeter wave method for quality assessment of large area graphene. *2D Materials*, 6(3):035028, may 2019.

[137] J. Ekin. Experimental Techniques for Low-Temperature Measurements: Cryostat Design, Material Properties and Superconductor Critical-Current Testing. *Experimental Techniques for Low-Temperature Measurements: Cryostat Design, Material Properties and Superconductor Critical-Current Testing*, 9780198570547:1–704, oct 2006.

[138] L. Marie, A. Fatimy, J. Hrubý, I. Nemec, J. Hunt, R. Myers-Ward, D.-K. Gaskill, M. Kruskopf, Y. Yang, R. Elmquist, R. Marx, J. Slageren, P. Neugebauer, and P. Barbara. Nanostructured graphene for nanoscale electron paramagnetic resonance spectroscopy. *Journal of Physics: Materials*, 3(1):014013, jan 2020.

[139] C. A. Swenson. Mechanical Properties of Teflon at Low Temperatures. *Review of Scientific Instruments*, 25(8):834, dec 2004.

[140] L. Kormoš, P. Procházka, A.-O. Makoveev, and J. Čechal. Complex k-uniform tilings by a simple bitopic precursor self-assembled on Ag(001) surface. *Nature Communications 2020 11:1*, 11(1):1–6, apr 2020.

[141] J. Hrubý, V. T. Santana, D. Kostiuk, M. Bouček, S. Lenz, M. Kern, P. Šiffalovič, J. van Slageren, and P. Neugebauer. A graphene-based hybrid material with quantum bits prepared by the double langmuir–schaefer method. *RSC Adv.*, 9:24066–24073, 2019.

[142] F. Ciccullo, M. Glaser, M.-S. Sättele, S. Lenz, P. Neugebauer, Y. Rechkemmer, J. van Slageren, and M.B. Casu. Thin film properties and stability of a potential molecular quantum bit based on copper(ii). *J. Mater. Chem. C*, 6:8028–8034, 2018.

[143] O. Laguta, A. Sojka, A. Marko, and P. Neugebauer. Rapid scan esr: a versatile tool for the spin relaxation studies at (sub)thz frequencies. *accepted in Applied Physics Letters*, 2022.

[144] H. Sato, L. A. Dalton, D. Ha, R. W. Quine, S. S. Eaton, and G. R. Eaton. Electron spin relaxation in x-lithium phthalocyanine. *The Journal of Physical Chemistry B*, 111(28):7972–7977, 2007.

[145] G. Ilangovan, Jay L. Zweier, and P. Kuppusamy. Electrochemical preparation and epr studies of lithium phthalocyanine. *The Journal of Physical Chemistry B*, 104(40):9404–9410, 2000.

[146] S. S. Eaton and G. R. Eaton. Epr spectra and electron spin relaxation of o$_2$. *Applied Magnetic Resonance*, 52(10):1223–1236, 2021.

[147] P. Turek, J.-J. André, A. Giraudeau, and J. Simon. Preparation and study of a lithium phthalocyanine radical: optical and magnetic properties. *Chemical Physics Letters*, 134(5):471–476, 1987.

[148] A. Mobae, R M. Nathan, D. Nallathamby, J. Cook, J. B. Mitchell, S. Subramanian, and M. C. Krishna. Preparation and epr studies of lithium phthalocyanine radical as an oxymetric probe. *Free Radical Biology and Medicine*, 25(1):72–78, 1998.

[149] A. Marko, A. Sojka, O. Laguta, and P. Neugebauer. Simulation of nitrogen nuclear spin magnetization of liquid solved nitroxides. *Phys. Chem. Chem. Phys.*, 23:17310–17322, 2021.

[150] J. M. North. *Synthesis and characterization of single-molecule magnets: manganese-acetate, iron-bromium, and analogs*. PhD thesis, The Florida State University, 2004.

List of Abbreviations

AWG	A rbitrary Waveform Generator
BDPA	α,γ-Bisdiphenylene-β-phenylally
CEITEC	Central European Institute of Technology
CSH	Carusel Sample Holder
CT	Computed Tomography
cw	continuous wave
DNP	Dynamic Nuclear Polarization
DPPA	Diphenyl phosphoryl azide
EPR (ESR)	Electron Paramagnetic Resonance (Electron Spin Resonance)
FIR	Far InfraRed
FLF	Fast Loading Flange
FRaSCAN	Frequency Rapid SCAN
LiPc	Lithium Phthalocyanine
MOTeS	Magneto-optical and THz Spectroscopy Research Group
HF-EPR	High Field / High Frequency Electron Paramagnetic Resonance
ChSH	Chip Sample Holder
LSH	Liqude Sample Holder
m.w.	Microwave
NMR	Nuclear Magnetic Resonance
OM	Optical Microscopy
PET	Positron Emission Tomography
QO	Quasi optics
RS	Rapid Scan
SH	Sample Holder
SIM	Single-ions magnet
SMM	Single-Molecule Magnets
SSH	Simple Sample Holder
TEMPOL	4-Hydroxy-tetramethylpiperidine 1-oxy
THz	Terahertz
RSH	Rotator Sample Holder
UHV	Ultra-High Vacuum
VNA	Vector Network Analyzer
VSH	Vacuum Sample Holder
VTI	Variable Temperature Insert
ZFS	Zero Field Splitting

# List of appendices

A Samples

Lithium phthalocyanine (LiPc)

Lithium Phthalocyanine in micro crystalline form was prepared electrochemically following a procedure described in the literature [147, 148]. The sharp crystal without any optical crack was chosen and glued on mirror.

Graphene-based bolometer

A bolometer fabricated from epitaxial graphene on silicon carbide. These bolometers utilized a graphene quantum dot to produce a temperature-dependent resistance [120]. Due to quantum confinement effects, thermal activation is required for conduction across the dot, producing a highly responsive broadband detector at low temperatures. This nanostructured graphene device was used to measure radiation intensity at frequencies between 10 GHz and 1 THz.
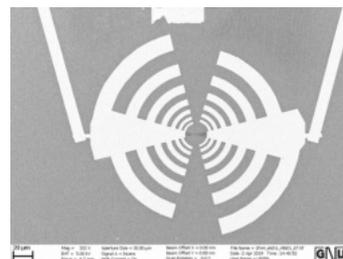
Copper Acetate Monohydrate

Single crystals of the dimeric copper acetate monohydrate ($[Cu(CH_3COO)_2 \cdot H_2O]$) were obtained as follows: copper(II) acetate (10 g, x mmol) was dissolved in 50 ml of 70°C water and stirred until a supersaturated solution was obtained. A drop of concentrated acetic acid was added during stirring to prevent reduction to Cu(I) which was observed otherwise. The solution was filtered with micropore filter $0.2\,\mu$m and kept under constant temperature of 40°C in an oil bath in order to decrease volume and initiate crystallization. Crystals of about 2 mm^2 were grown after 2 days and selected for the EPR measurement tests in this work. The selected crystal was randomly oriented in the RSH. The four EPR signals observed at a single field/frequency correspond to the MW absorption by two rotated molecules in the lattice of this compound.
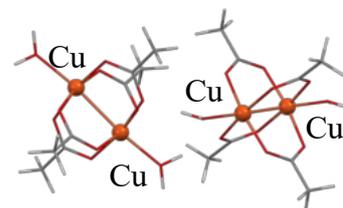
Diphenyl phosphoryl azide (DPPA)

The DPPA was bought from Sigma Aldrich and dissolved in toluene (bought from Sigma Aldrich) to desired concentration. After dissolving, final mixture was dropped into cell of LSH. The spectra shown in Fig.6.7 were recorded without sample degassing.
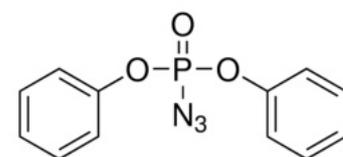
α,γ-Bisdiphenylene-β -phenylallyl (BDPA)

The BDPA was bought from Sigma Aldrich and dissolved in toluene together with polystyrene (bought from Sigma Aldrich) to desired concentration. After dissolving, final mixture was dropped on the mirror, where the toluene evaporated overnight creating film of polystyrene with BDPA inside its matrix.
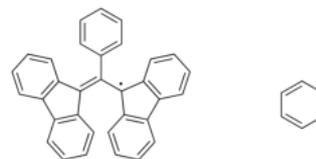
4-Hydroxy-tetramethylpiperidine 1-oxyl (TEMPOL)

The TEMPOL was bought from sigma Aldrich and dissolved in acetone to concentration of $1\,\mathrm{mMol}$. The same compounds was already used for the sample preparation of our recent EPR measurements [149]. The spectra shown in Fig. 5.8 were recorded without sample degassing.
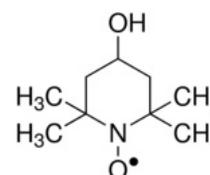
$\mathbf{Mn_{12}AC}$

First time prepared by Lis [87], and its SMM magnetic properties discovered by Sessoli [88]. The $[\mathrm{Mn_{12}(CH_3COO)_{16}(H_2O)_4O_{14}}]$ $\cdot$ $2\mathrm{CH_3COOH}$ $\cdot$ $4\mathrm{H_2O}$ was prepared by modification of following synthesis. 1 mmol of $\mathrm{Mn(CH_3COO)_2}$ $\cdot$ $4\mathrm{H_2O}$ was dissolved in 60 and stirred until all crystals dissolved. Then, 4 mmol of finely ground KMnO4 was added to the stirring solution in agate mortar. The KMnO4 was added by small portions over 2 minutes. Subsequently, the reaction was allowed to be stirred for strictly 5 minutes and quickly filtered. The dark brown solution was kept in dark for a week and left to crystalize. The crystals were removed by filtration under reduced pressure giving a good quality black crystals. The crystals were washed with cold ethanol and dried. The sharp crystal without any optical crack was chosen and glued on mirror by a vaccum grease. The Figure of $\mathrm{Mn_{12}AC}$ taken from [150].
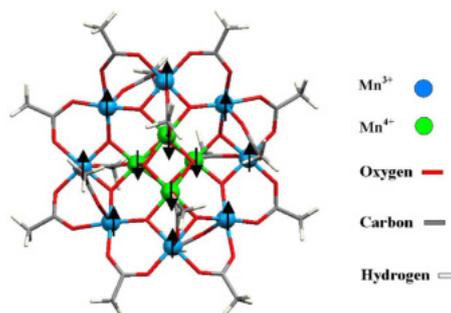
B Drawings

All dimensions are in mm. The abbreviation Assy means assembly.

B.1 01-Magnet-Frame
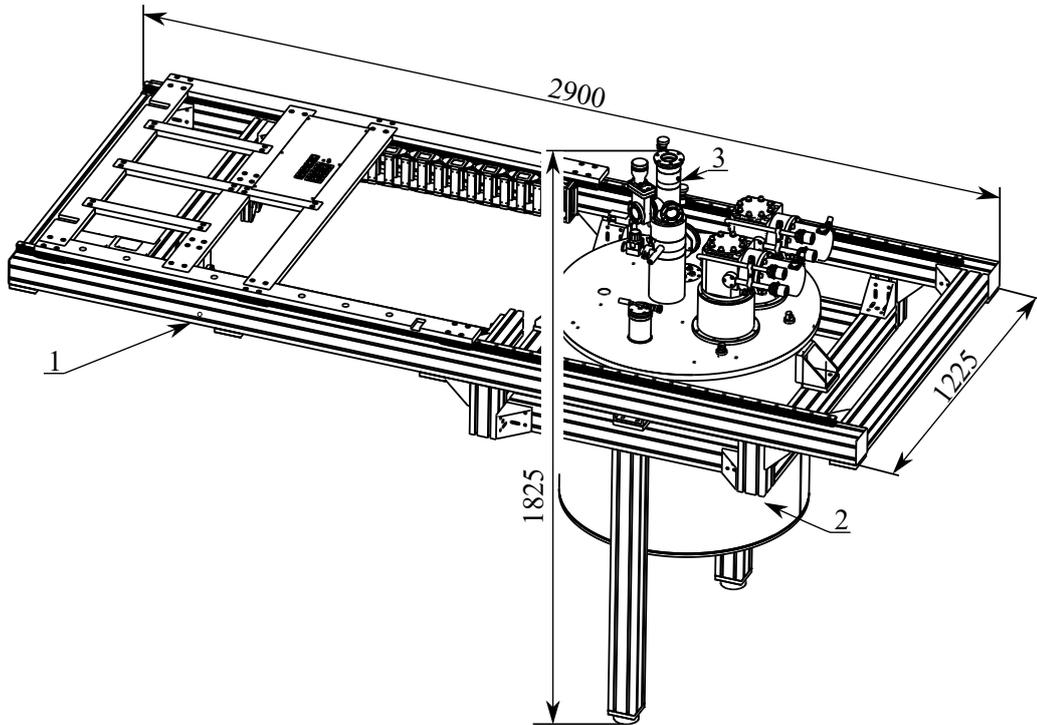
NO.	01_Part Name	Drawing	QTY	Seller	Type
1	01 - Frame- Magnet	01_01	1	Non	Assy
2	02 - Magnet	None	1	Cryogenic Ltd	Part
3	03 - Airlock	01_03	1	Non	Assy

01_01-Magnet-Frame
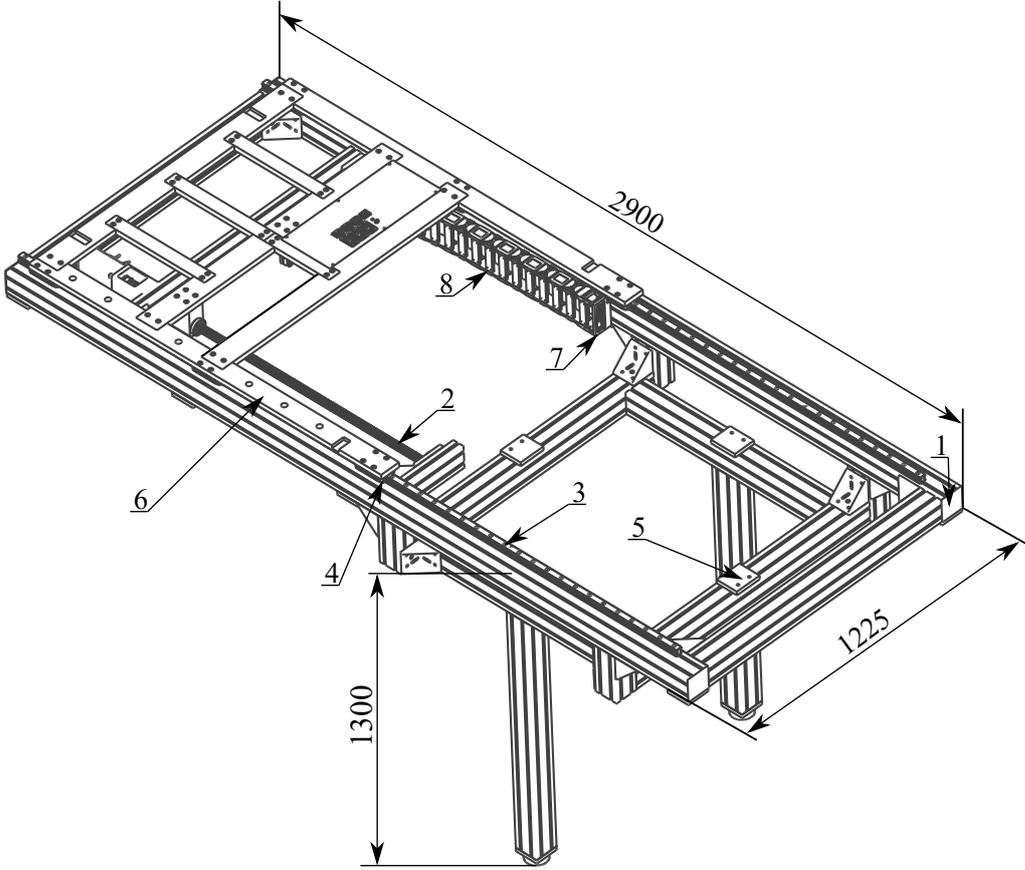
N.	01_01_Part Name	Drawing	QTY	Seller	Type
1	01 - Magnet Frame	Step only	1	Bosch Rexroth AG	Part
2	02 - MSystem-X	01_01_02	1		Assy
3	03 - FDA25D-2500	None	1	Betz s.r.o.	Part
4	04 - Kassette-FDA25K098	None	1	Betz s.r.o.	Part
5	05 - Magnet_plate	01_01_05	1		Part
6	06 - Magnet_FRAME_DESK	01_01_06	1		Assy
7	07 - BELT HOLDER	3D print	1		Part
8	08 - E4-32-10-EL-BELT	None	1	Igus inc.	Part

01_01_03 - Airlock
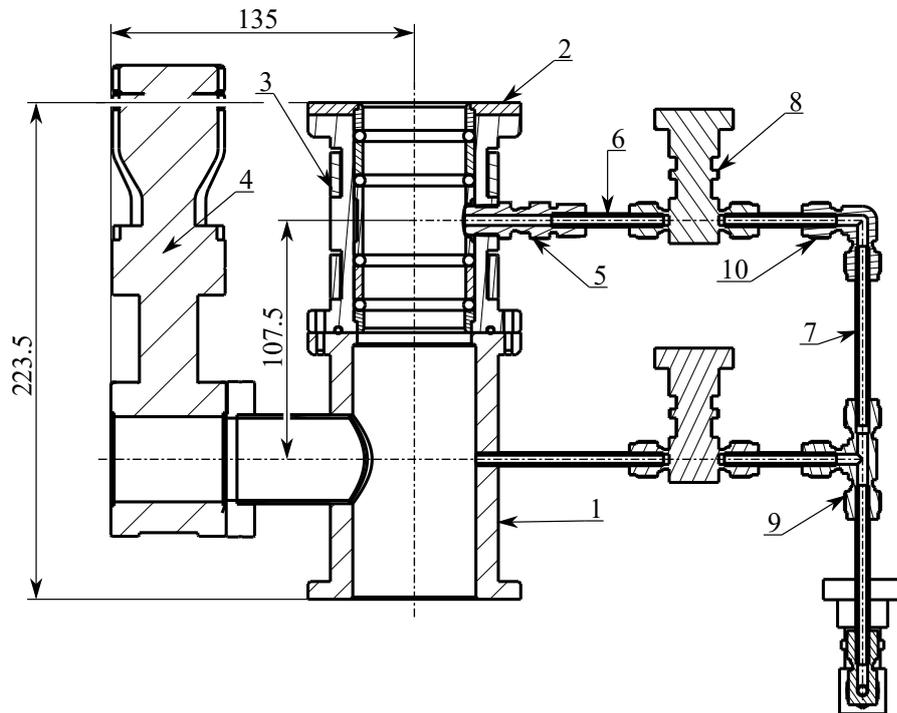
N.	01_03_Part Name	Drawing	QTY	Seller	Type
1	01 - Bottom	01_03_01	1		Assy
2	02 - TOP	01_03_01	1		Assy
3	03 - TOPNY DRAT	None	2	Elektron-etto, S.r.o.	Part
4	04 - GV-40CF-C-M4	None	1	VAT Vakuumventile AG	Part
5	05 - SS-400-11-4	None	1	Swagelok-Gruppe AG	Part
6	06 - SS-6H-50	None	5	Swagelok-Gruppe AG	Part
7	07 - SS-6H-80	None	2	Swagelok-Gruppe AG	Part
8	08 - SS-6H-MM-SC11	None	4	Swagelok-Gruppe AG	Part
9	09 - SS-6M0-3	None	2	Swagelok-Gruppe AG	Part
10	10 - SS-6H0-9	None	1	Swagelok-Gruppe AG	Part

B.2   02 - EPR Table
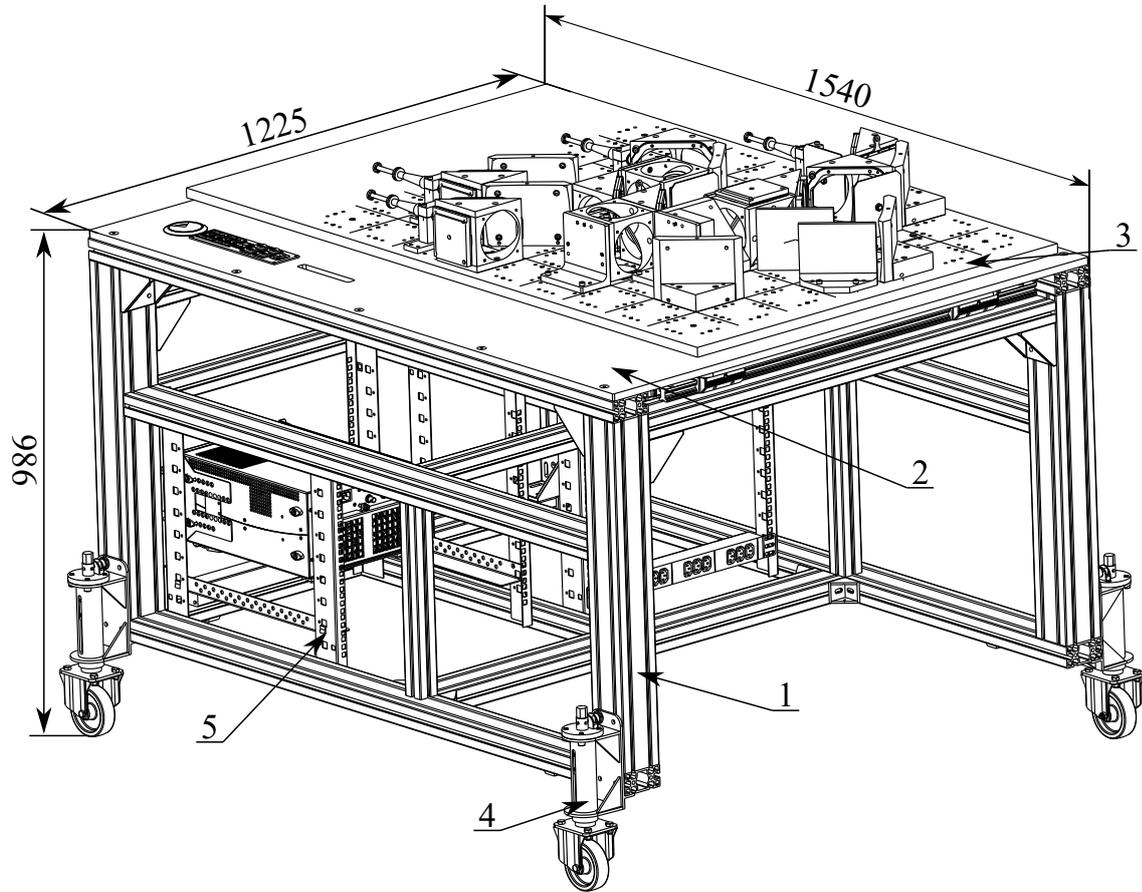
N.	02_Part Name	Drawing	QTY	Seller	Type
1	01 - EPR-Table-Frame	02_01	1		Assy
2	02 - TOP-Desk	02_02	1		Assy
3	03 - QO-Bridge	None	1	Thomas Keating Ltd	Assy
4	04 - Lifting-wheels	02_04	4		Assy
5	05 - Electronic rack	None	1	Rittal Czech, s.r.o.	Assy

02_01 - EPR-Table-Frame
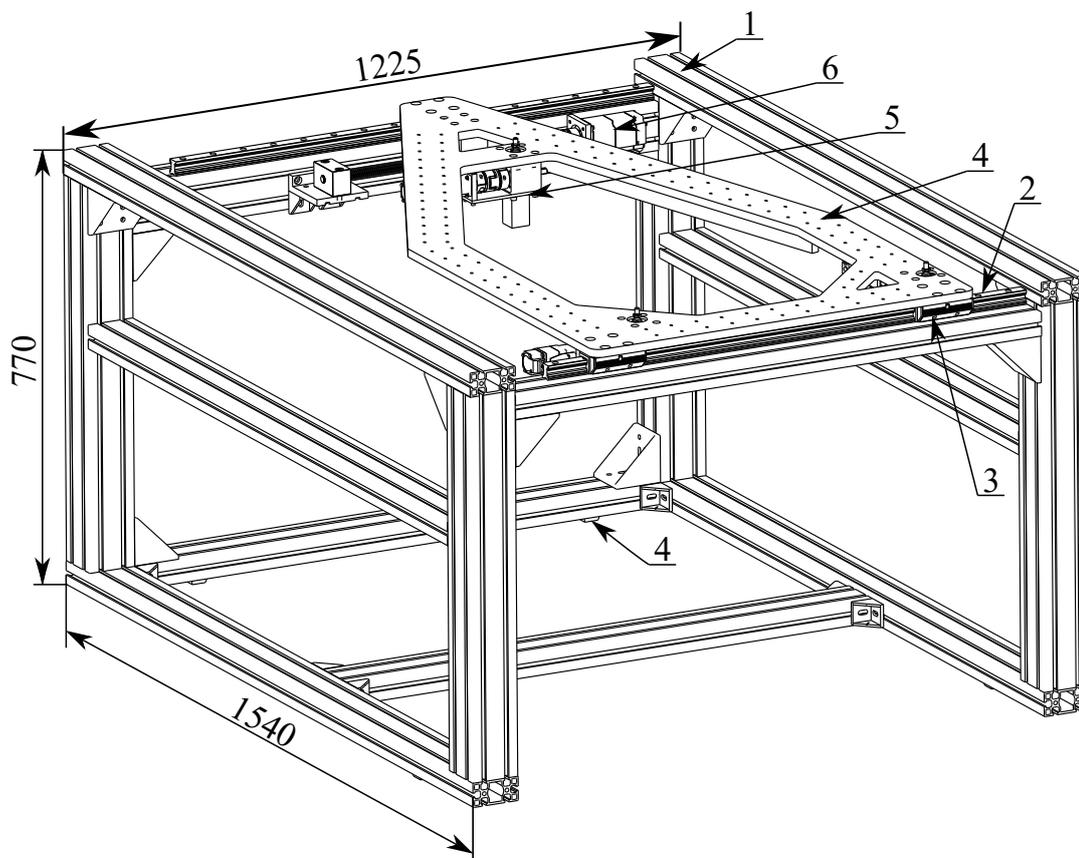
N.	02_01_Part Name	Drawing	QTY	Seller	Type
1	01 - Frame	Step only	1		Assy
2	02 - FDA25D-950	None	2	Betz s.r.o.	Part
3	03 - Kassette-FDA25K098	None	3	Betz s.r.o.	Part
4	04 - Delta-Plate	02_01_04	1		Assy
5	05 - MSystem-Z	02_01_05	3		Assy
6	05 - MSystem-Y	02_01_06	1		Assy
7	05 - Locking-Pin	02_01_07	4		Part

B.3   03 - EPR Probe
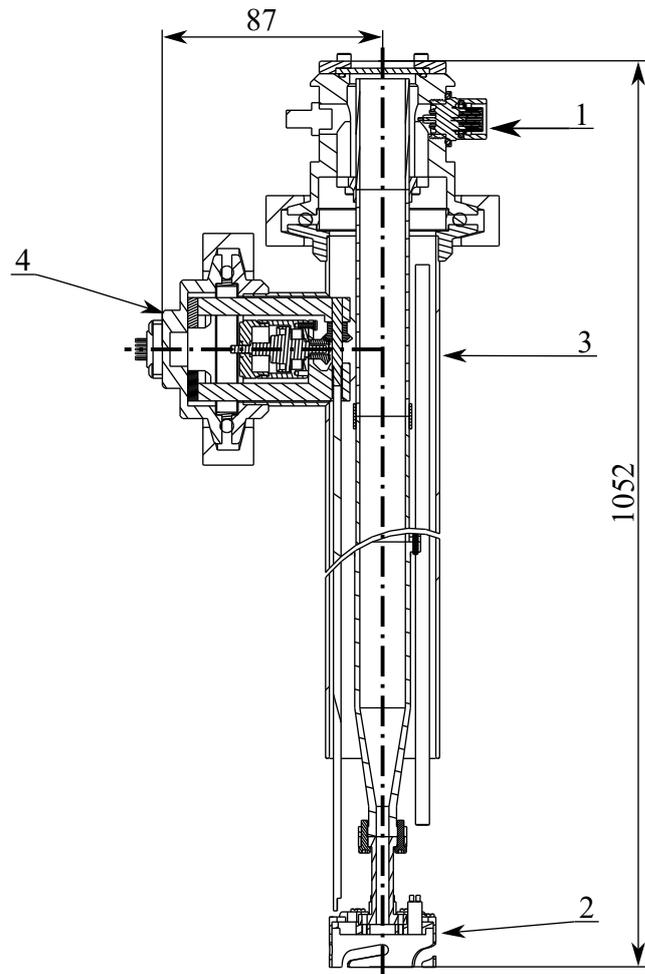
N.	03_Part Name	Drawing	QTY	Seller	Type
1	01 - TK-Probe	03_01	1		Assy
2	02 - FLF	03_02	1		Assy
3	03 - Cover-Tube	03_03	1		Part
4	04 - Msystem-Piezo	03_04	1		Assy

03_02-FLF
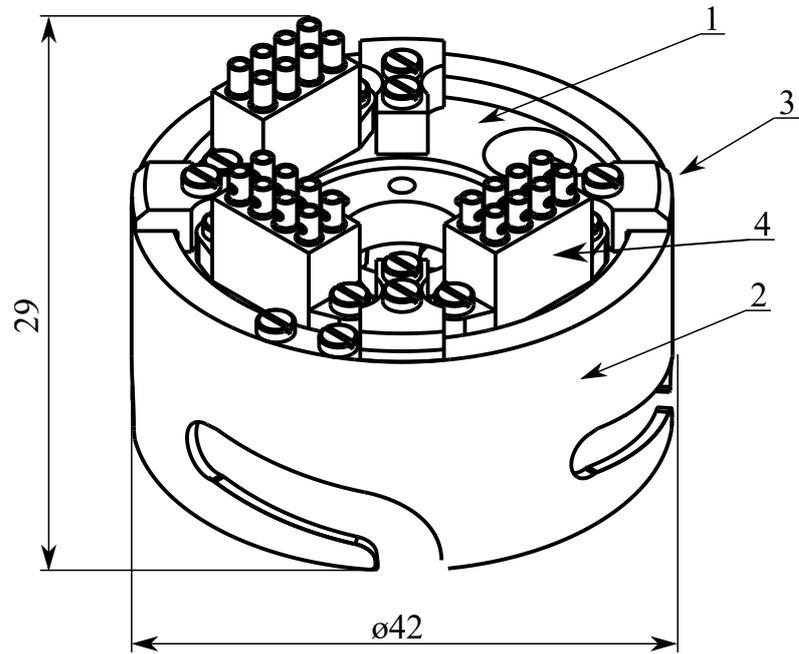
N.	03_02_Part Name	Drawing	QTY	Seller	Type
1	01 - Flange-Base	03_02_01	1		Part
2	02 - Flange-Collar	03_02_02	1		Part
3	03 - Collar-Holder	03_02_03	4		Part
4	04 - Electric-Block	03_02_04	3		Assy

B.4 Sample Holders

04-SSH
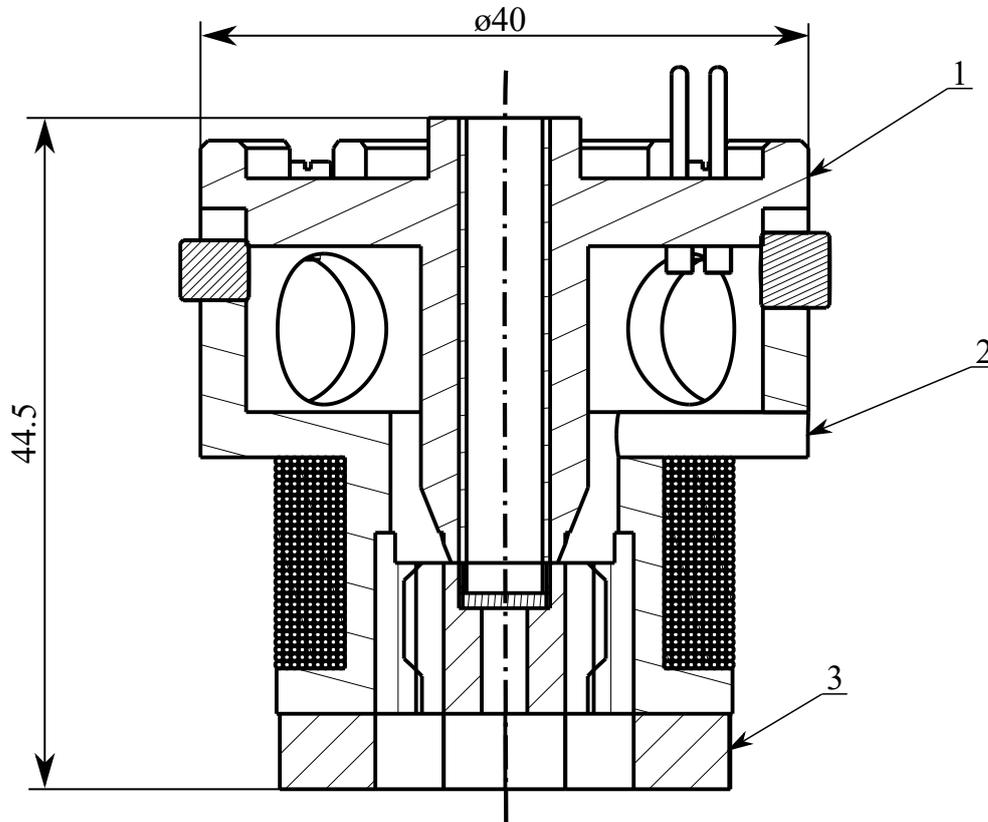
N.	04_Part Name	Drawing	QTY	Seller	Type
1	01 - Connection-Part	04_01	1		Assy
2	02 - Body	04_02	1		Assy
3	03 - Functional-Part	04_03	1		Assy

05-BSH

ø40

42.5
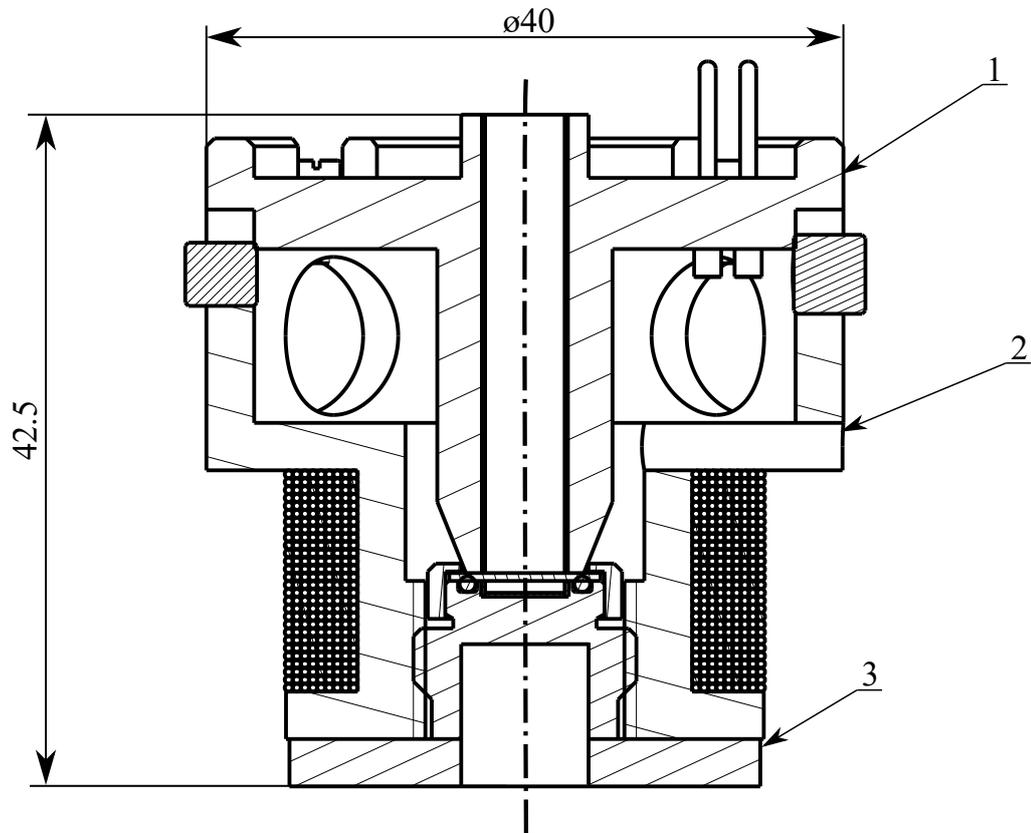
N.	05_Part Name	Drawing	QTY	Seller	Type
1	01 - Connection-Part	05_01	1		Assy
2	02 - Body	05_02	1		Assy
3	03 - Functional-Part	05_03	1		Assy

06-RSH
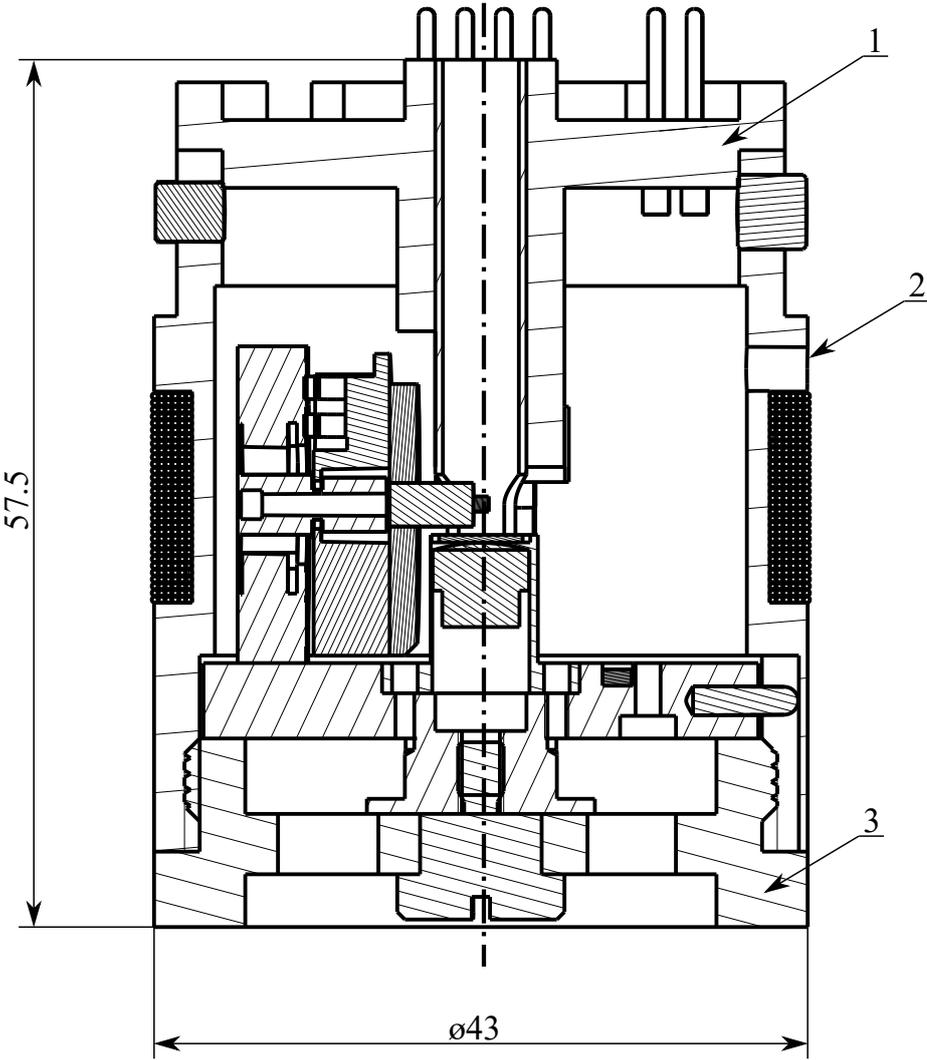
N.	06_Part Name	Drawing	QTY	Seller	Type
1	01 - Connection-Part	06_01	1		Assy
2	02 - Body	06_02	1		Assy
3	03 - Functional-Part	06_03	1		Assy

07-ChSH
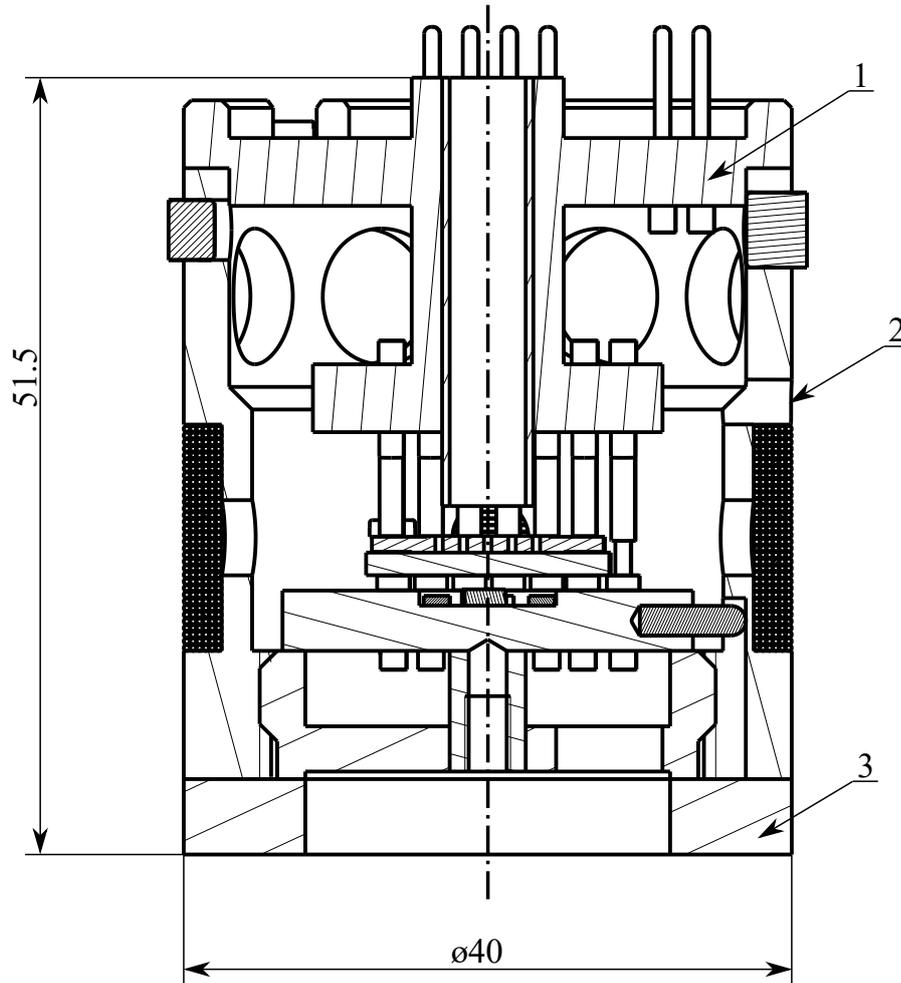
N.	07_Part Name	Drawing	QTY	Seller	Type
1	01 - Connection-Part	07_01	1		Assy
2	02 - Body	07_02	1		Assy
3	03 - Functional-Part	07_03	1		Assy

08-CSH
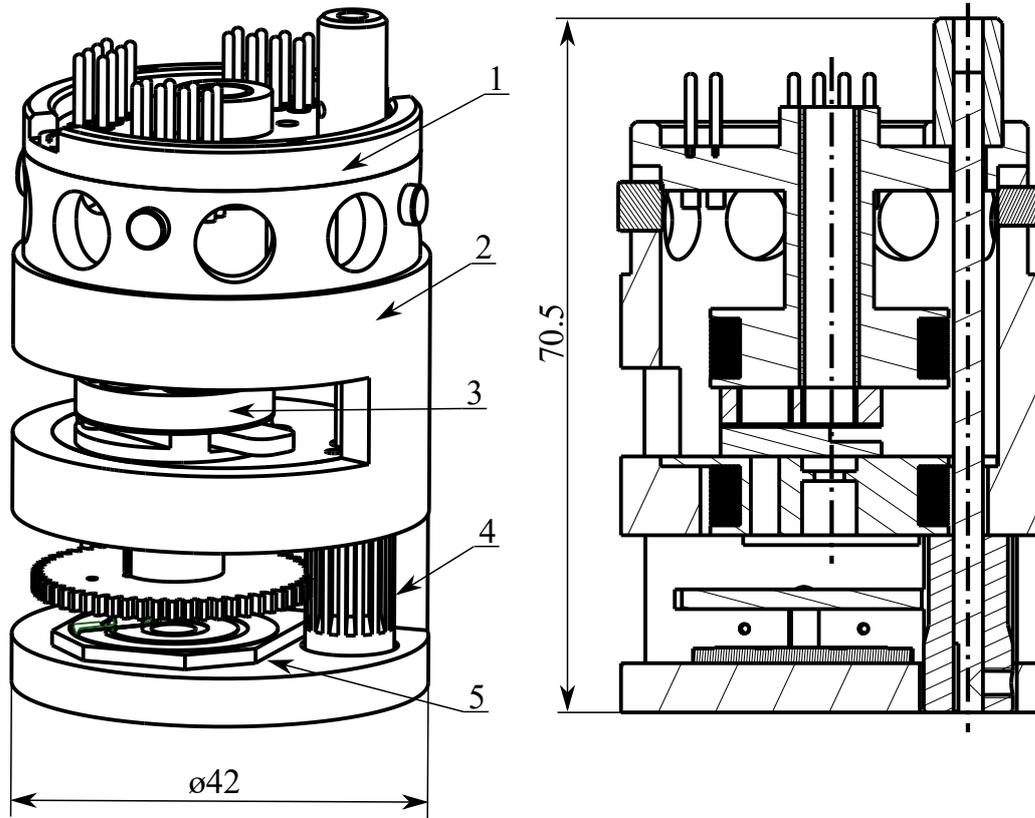
N.	08_Part Name	Drawing	QTY	Seller	Type
1	01 - Connection-Part	08_01	1		Assy
2	02 - Body	08_02	1		Assy
3	03 - Rotary-Platform	08_03	1		Assy
4	04 - Gear-System	08_04	1		Assy
6	05 - Encoder	08_05	1		Part

08-VSH
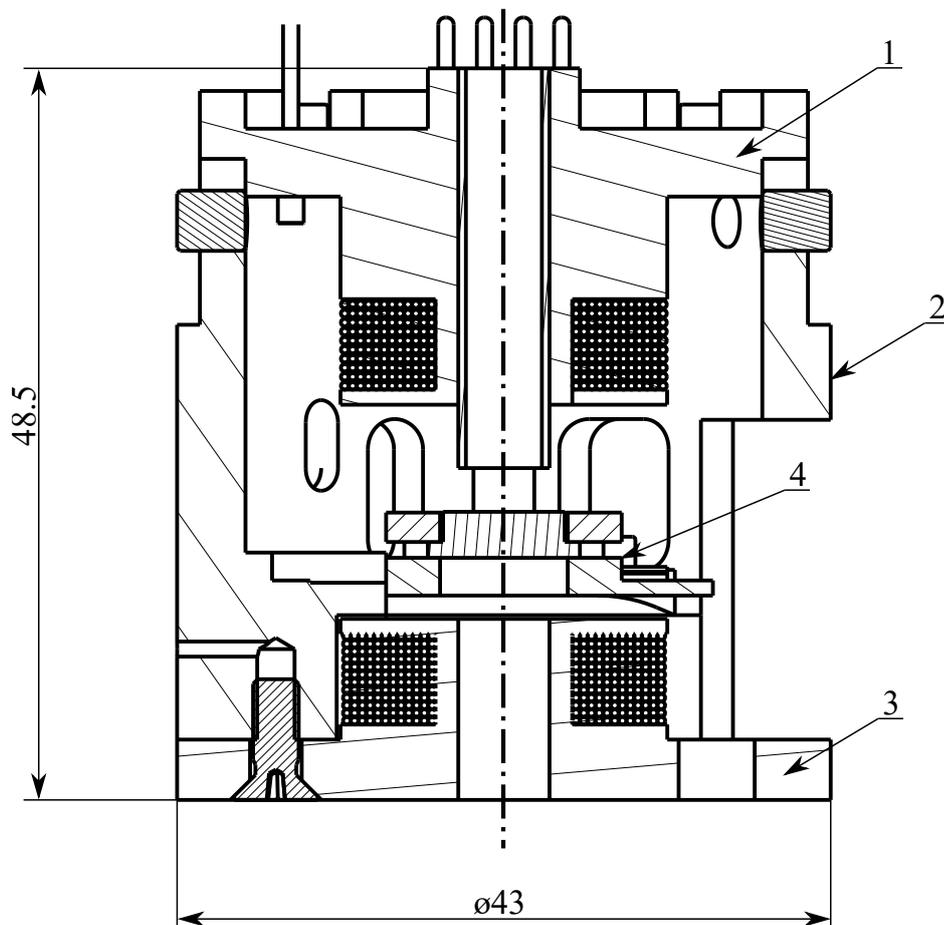
N.	09_Part Name	Drawing	QTY	Seller	Type
1	01 - Connection-Part	09_01	1		Assy
2	02 - Body	09_02	1		Assy
3	03 - Omictron-Plate	09_03	1		Assy
4	02 - Bottom-Coil	09_04	1		Part

C VTI magnet

The VTI orVariable temperature insert provides the means to vary the sample temperature between 2K and 400K. The scheme of our VIT is showin in Fig. C.1. Cooling of the VTI and sample is provided by close helium circuit. The helium gas is cooled and liquidized by the cryo-cooler at the 40K and 4K stages.Then cooled bellow 4 K via expansion after the needle valve.
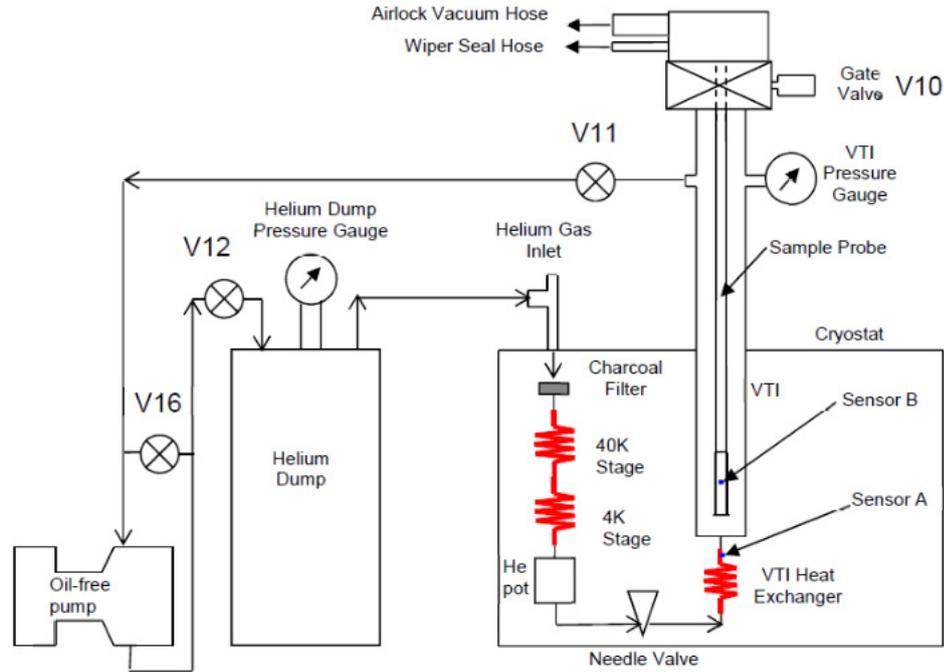

Fig. C.1: Scheme of VTI magnet

The VTI-He circuit works as follows: Helium gas is stored in the "dump" vessel at room temperature. Circulation of the He circuit is realized by the scroll pump, which is always turned on. The He gas flow from the dump into the VTI circuit through the helium gas inlet. First, the He gas passes through a charcoal filter, cooled to a temperature lightly below 70 K, which keeps the He gas clean. Then the gas flows through the first stage heat exchanger, which cools the gas to 40K. After that, the second stage of the cryo-cooler cooled at a temperature of 4K or less, where the He gas liquidized and dropped into He pot. The helium liquid then flows across the needle valve, after which it expands in the VTI exchanger and cools further to approximately 2K. The cold gas then flows around sample (sensor B) in VTI space to the top of the VTI, where it exits and travels back to the pump and dump.

The needle valve is automatically controlled. A VTI pressure gauge is fitted to allow the user to set and monitor the flow rate (directly related to pressure). Typically a pressure between 5 and 15 mbar is recommended. The heat exchanger at the bottom of the VTI is fitted with a thermometer (sensor A) and a heater controlled using the temperature controller. The heater is used to adjust the helium gas temperature and therefore regulate the sample temperature.

D Wiring and electronic distribution

D.1 Wiring of the EPR table

Part of the EPR table is the electronic rack for all controllers, power sources, and power grid connections. The distribution of electronics in the EPR table is shown in Fig.D.1. The servo controllers and USB hub are hidden under the cover plates and are reachable from the left side when the drawer is opened. The EPR table support desk on the top contains the power grid, four USB ports and two eternal ports connected with the USB hub, and a ground connection.
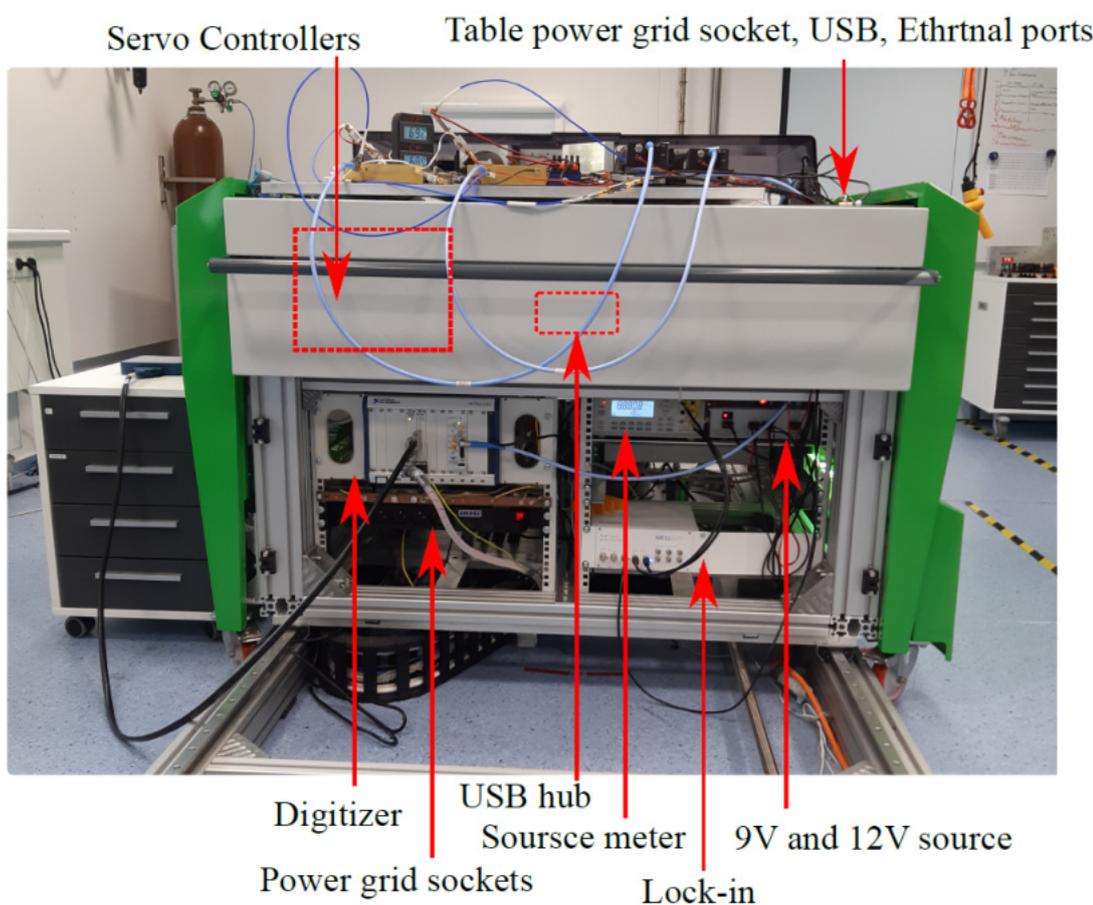
D.2 Wiring of the probe

To interface electrical signals, as was mentioned, three hermetic connectors (SFE102A053, DBEE104A056, SFE104A086) were installed on the probe head (see Fig.D.2).
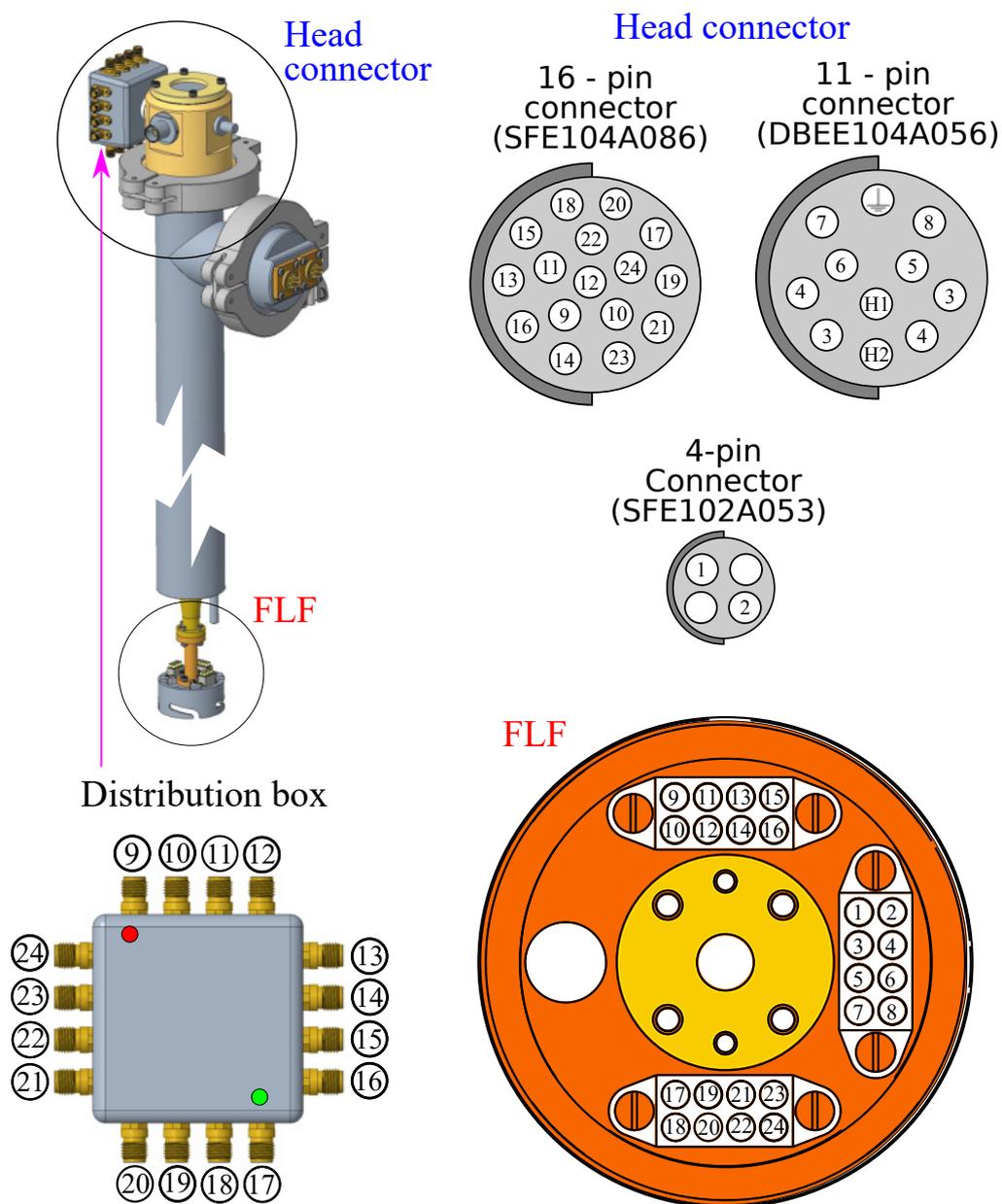
One of the connector is used to drive a modulation coil, the second one for devices commonly used in all sample holders: a sample heater, a temperature sensor, and a Hall sensor. The third connector is used for signals which purpose differs with sample holder (electronic transport measurements in the case of the chip holder, driving of the piezo rotator in the case of the rotator sample holder, position reading in the case of the carousel sample holder). Twisted wire pairs were used for all leads

between connectors on the probe head and connectors on the flange of the sample holder to reduce the signal interference. To reduce the heat leakage, most wires are 36 AWG size (0.1270 mm) and made of phosphor bronze. A few 32 AWG (0,2019 mm) phosphor bronze twisted pairs were used to supply the sample heater, the temperature sensor, and the Hall sensor. 26 AWG (0.4049 mm) polyimide enameled copper wires were used only in the case of the modulation coil and one pair is dedicated to the piezo rotator (32 AWG).The table D.2 sum up the wires and their resistances.

NO	Use	Wire	R [Ω]	NO	Use	Wire	R [Ω]
1	Piezo+ /Chip	Cu 32 AWG	0.7	9	Chip	Cu+Sn+P 36 AWG	≈10
2	Piezo-1 /Chip	Cu 32 AWG	0.7	10	Chip	Cu+Sn+P 36 AWG	≈10
3	Piezo ENC /Chip	Cu+Sn+P 36 AWG	≈10	11	Chip	Cu+Sn+P 36 AWG	≈10
4	Piezo ENC/Chip	Cu+Sn+P 36 AWG	≈10	12	Chip	Cu+Sn+P 36 AWG	≈10
5	Piezo ENC /Chip	Cu+Sn+P 36 AWG	≈10	13	Chip	Cu+Sn+P 36 AWG	≈10
6	Chip	Cu+Sn+P 36 AWG	≈10	14	Chip	Cu+Sn+P 36 AWG	≈10
7	Chip	Cu+Sn+P 36 AWG	≈10	15	Chip	Cu+Sn+P 36 AWG	≈10
8	Chip	Cu+Sn+P 36 AWG	≈10	16	Chip	Cu+Sn+P 36 AWG	≈10

NO	Use	Wire	R [Ω]
17	Modulation Coil	Cu 26 AWG	0.17
18	Modulation Coil	Cu 26 AWG	0.17
19	T. Sensor	Cu+Sn+P 32+36 AWG	3.45 + 9.35
20	T. Sensor	Cu+Sn+P 32+36 AWG	3.45 + 9.36
21	Hall Sensor / Heater	Cu+Sn+P 32 AWG	3.5
22	Hall Sensor / Heater	Cu+Sn+P 32 AWG	3.5
23	Hall Sensor	Cu+Sn+P 32 AWG	3.5
24	Hall Sensor	Cu+Sn+P 32 AWG	3.5

D.3 CSH encodere

Because of the relatively long shaft's elasticity and laxity in both gears, the rotation of the sample platform is not firmly (solidly) bound to the rotation of the motor. Therefore, the encoder equipped on motor can be used only to estimate the position, but not its precise determination. A resistive encoder was implemented to ensure that the position of the sample platform will always be adjusted properly (sample cell right below the waveguide). The resistive encoder was made on ceramic (alumina) substrate by printing and baking conductive and resistive paste (SEANT Technology, Brno, Czech Republic). Its topology is in the Fig. D.3. The encoder was mounted in the axis of a short rotating shaft that moves with a sample platform, right below the second gear. A slider that connects the resistive (black) line with conductive (silver) was made of a phosphor bronze stripe fixed to the gear bottom. The motion of the slider then strictly corresponds to the motion of the sample platform.
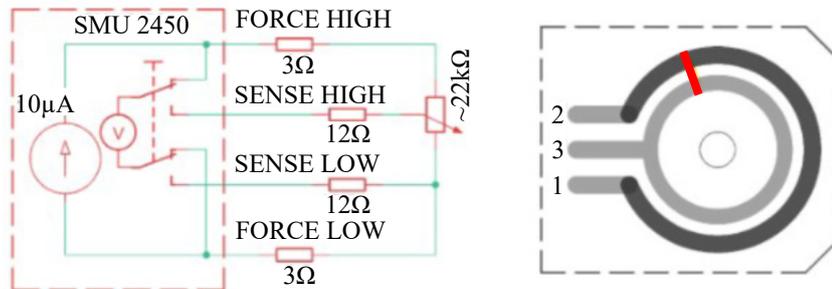
Because the change of resistance with a temperature is inevitable, minimizing its influence on the encoder for operation at various temperatures is necessary. This can be simply done if position evaluation is not based on measurement of absolute resistance but rather as a ratio of the slider resistance (between terminal 2 and 3) to the total resistance of resistive arc (2 and 1). For this purpose, we used a source meter unit Keithley 2450 (SMU) in current source mode, while measuring voltage by two and four-wire method to measure the voltage on the whole resistive arc and voltage on the slider, respectively. The schematic that illustrates a connection of encoder with SMU is in Fig. D.3. All instrument terminals were connected to EPR probe head by coaxial cables. A twisted pair of insulated copper wires was used from the probe head for connection to terminals 1 and 2 of the encoder. The total resistance of wires in a FORCE loop was 6 Ω which adds +0.027% error to the voltage measured. Terminals 2 and 3 (the slider) were connected to the probe head via a twisted pair of phosphor bronze wires, which reduces a thermal leak. Their resistance can be neglected for the SENSE loop because the input resistance of the

instrument is more than 10 GΩ. Finally, the equation shows how the position is calculated and derived and why it is temperature independent:

$$\varphi = \frac{R_S}{R_T} \cdot 330° = \frac{\alpha \cdot \Delta T \cdot R_{S20}}{\alpha \cdot \Delta T \cdot R_{T20}} \cdot 330° = \frac{\frac{U_{S20}}{I}}{\frac{U_{T20}}{I}} \cdot 330° = \frac{U_S}{U_T} \cdot 330°. \qquad \text{(D.1)}$$

E Programs

E.1 Carousel position determination

PMD401 (PiezoMotor) was used as controller of the piezo-electric motor. This controller communicates with a host computer by a two wire RS485 interface, using commands represented by an ASCII strings. Description of all commands and interface settings can be found in a Technical manual to PMD401. Based on the manual a simple custom software for PMD401 was created in LabVIEW. Subsequently, the software was extended to provide a feedback information about position from resistive encoder via Keithley 2450 SMU (Tektronix).

In a block diagram, an event structure is used to handle user's interactions (see E.1). Handled user events are: reset quadrature encoder on piezo motor, immediately stop piezo motor, refresh measurement by SMU, select a desired position and exit the program. Internally and periodically invoked event is a timeout event that is used to connect to both instruments, if they are not connected, measure position and adjust it. User can select either a feedback from the quadrature encoder or the custom encoder.
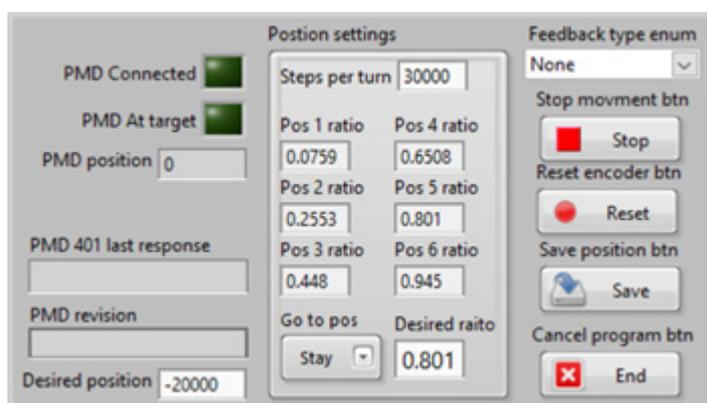

Fig. E.1: Block diagram for automatic position of carousel sample holder. Note, first time the position has to be found automatically.

E.2 Automatic coupling system

The Fig. E.2 shows the user interface from a program to the automatic coupling system. In the first version, the program for coupling is rather simple and can move only with one motor simultaneously. Designed UI gives an overview of the current situation (which servo is moving and the actual position) and the emergency stop button. For progress, the integral of the signal is shown in the graph.

The computer communicates directly with the servo controllers IndraDrive Cs (Bosh Rexroth AG, DE) through ethernet. The drivers already contain set limits and speeds. Therefore, the communication uses commands represented by ASCII strings.


Fig. E.2: Block diagram for automatic position of carousel sample holder. Note, first time the position has to be found automatically.